GRAPHITE TECHNOLOGY COURSE

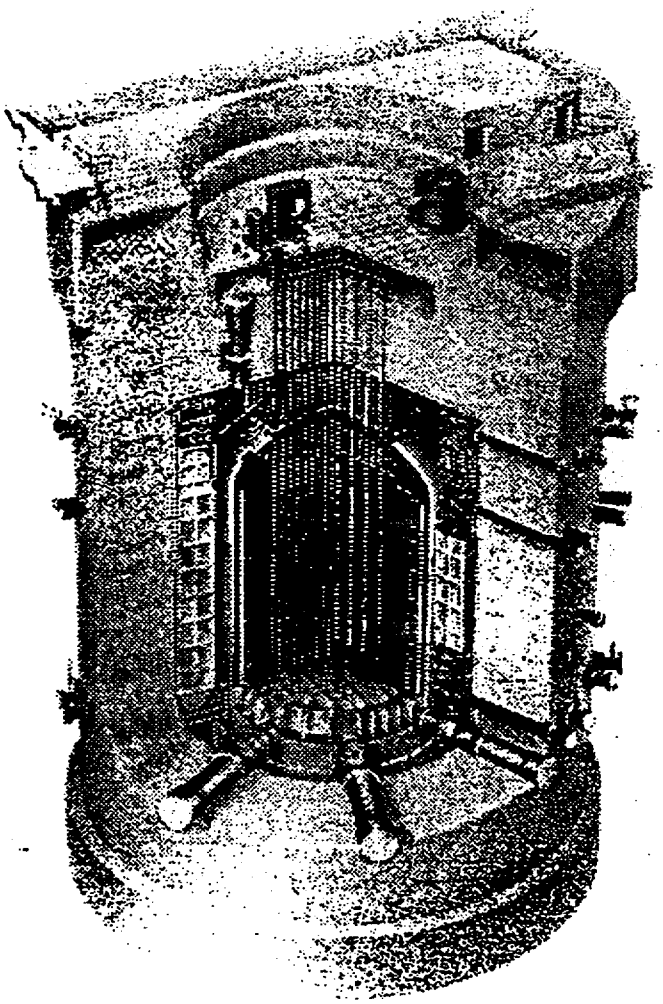

Dr BJ Marsden

For further details contact:

Tel: 01925 254953

Fax: 01925 252285

GRAPHITE TECHNOLOGY COURSE

LECTURE 1

1. Introduction and Aims of the Course

The principal difficulty in the use of graphite as a nuclear reactor moderator material stems from the large and continuing changes in dimensions and physical properties which occur due to the combined effects of radiation damage and radiolytic weight loss that are suffered by the material during long-term reactor exposure. These changes can be severe and are difficult to predict with certainty for the designed lifetime of modern reactors. The nature of the changes is such that they lead to problems in attempts to design stable and long lasting moderator structures, and their structural effects may become life-limiting for some moderator designs.

Assessment of the effects of dimensional and physical property changes on the integrity of graphite moderator structures has thus become an important factor in the preparation of safety cases that are written in support of moderator design, reactor operation and life extension. In order to carry out such assessments it is necessary to have a good basic understanding of the phenomena of radiation damage and radiolytic weight loss in graphite, and the various complex factors which influence the resultant dimensional and physical property changes they induce in the material. Secondly, it is necessary to be able to understand the extensive database which is available on graphite behaviour under irradiation, and in particular to know how to interpret that data correctly for the specific type of graphite, radiation conditions and physical environment appropriate to each application. Thirdly, it is essential that the correct methodology should be fully understood and properly applied throughout the assessment process used to evaluate all parameters such as radiation damage dose, dose rate, equivalent temperature, radiolytic weight loss, dimensional property change and physical property changes as a function of all relevant basic reactor parameters. Finally, it is essential to know how to apply the evaluated dimensional and physical property changes in the assessment process, and to have a basic understanding of how these changes may affect moderator structural integrity.

One of the aims of the course will be to give those attending a fundamental understanding of the basic principles, data and methodology used in the assessment of graphite moderator structures including the evaluation of:

(i) Radiation damage dose and dose rate.

(ii) Equivalent temperature.

(iii) Dimensional changes of PGA and Gilsocarbon graphites.

(iv) Physical property changes of PGA and Gilsocarbon graphites.

(v) Radiolytic weight loss.

(vi) Effects of radiolytic weight loss.

The course is confined to Magnox and Advanced Gas-cooled reactors and will introduce members to graphite moderator structural design of both types. Important aspects of the assessment of the effects of in-pile exposure on graphite moderator components and structural integrity will also be discussed, including such effects as the evaluation of thermal and shrinkage stresses, brick distortion and structural loading. The use of computer codes in the assessment process will be addressed.

2. Graphite Manufacture

The early nuclear power reactors (Magnox) were constructed from an anisotropic extruded pure petroleum coke graphite known as Pile Grade A (PGA). The irradiation conditions in the later Advanced Gas-cooled Reactors precluded the use of PGA and a new material was developed by the manufacturers based on a specification produced by the UKAEA. This material was an isotropic moulded graphite manufactured using a coke prepared from Gilsonite, a naturally occurring asphalt mined in Utah, USA. This improved graphite, which has better all round properties and dimensional stability under fast neutron irradiation, is known as Gilsocarbon graphite.

The properties of PGA and Gilsocarbon graphites are shown in Table 1.1

Fig 1.1 illustrates the process of graphite manufacture. Coke may be derived from naturally occurring asphalt or as a by-product of the oil refining process and may be used to make nuclear graphite providing that its purity is acceptable. The coke is first calcined, that is heat treated to 1300°C to remove residual volatile hydrocarbons, and is then crushed, ground and blended to give a specific particle size distribution. The coke particles are then mixed with a pitch binder and then either extruded or moulded to the required shape. The "green" article is then baked at a temperature of about 1000°C to carbonise the pitch binder and then impregnated under pressure with a suitable pitch to increase the density. The brick is then graphitised by heating electrically in a furnace packed with coke dust and sand to a temperature of about 2800°C, taking three or four days to reach temperature, a day or so at temperature and about 14 days to cool. Crystal development takes place during graphitisation and as a result its properties change markedly, particularly with respect to ease of machining and improved conductivity. The purity of the product is also improved since many of the contaminants are volatilised out at these temperatures. The brick may receive further impregnation and graphitisation steps to improve density, strength, etc.

The extrusion process used in the manufacture of PGA graphite tends to align the needle-shaped petroleum coke particles parallel to the direction of extrusion which results in a highly-orientated structure. Furthermore, the crystallographic layer planes of the eventual graphite crystallites tend to lie parallel to the long aixs, thus producing a product having anisotropic properties, ie properties measured parallel to the extrusion direction differ from those perpendicular to it. Gilsocarbon graphite on the other hand, being moulded and made from coke containing spherical structures in which the graphite crystallites tend to lie in an "onion skin" structure, has very isotropic properties. Figures 1.2 and 1.3 illustrate these differences.

3. Radiation Damage and Annealing

A neutron-induced fission in nuclear reactor fuel produces two to three new neutrons with energies which occur over a wide range. The spectrum of fission neutrons peaks at an energy of about 2 MeV and extends to energise greater than 10 MeV.

The role of the graphite moderator is to slow these neutrons down to thermal energy levels by collisions between the neutrons and the nuclei of carbon atoms. In a collision between a neutron and a carbon nucleus a substantial fraction of the neutron energy is transferred to the nucleus. The binding energy of the carbon atom in the graphite lattice is about 5eV, and, if the energy transferred is only a few times greater than this, it is irreversibly displaced from that site. The primary displaced carbon atom will collide with other carbon atoms causing them to be displaced also, and so on, thereby creating a displacement cascade, Fig 1.4.

A graphite crystallite consists of layers of carbon atoms with the layers stacked one upon the other, and with the carbon atoms in each layer located at the vertices of a hexagonal network, Fig 1.5. Displaced atoms may move to positions between the layers, known as "interstitial" positions, leaving behind them holes or "vacancies". The interstitial atoms group together to form interstitial loops which push the atomic layers apart, causing crystal growth perpendicular to the layers. The vacancies form vacancy lines which cause the atomic layers to contract in the plane of the layers, causing crystal shrinkage parallel to the layers. Fig 1.4 illustrates the damage process.

The large majority of displaced atoms find their way back to normal lattice positions, but a significant proportion form defects which change the properties of the graphite in various ways. Some of the displaced atoms return by a process of annealing, the number of atoms so affected being a function of both irradiation temperature and duration. Thus, a given fast neutron damage dose will produce more net damage if the irradiation temperature is reduced or the dose rate is increased (ie a given dose is received over a shorter period of time). As will be seen later, this aspect of radiation damage is particularly important in both the interpretation of data and in its application during the assessment process.

4. Damage Function

The damage received by an element of graphite from an irradiation source is a function of a source strength, the distance from the source, and the attenuation in damage with distance through intervening graphite. The attenuation of damage through graphite was first measured by Kinchin[1] in the graphite reflector of the BEPO reactor at Harwell. The resultant curve of relative damage through graphite is shown in Fig 1.6. The curve permits damage in any graphite lattice to be computed providing that an appropriate adjustment is made for differences in graphite density between BEPO (1.6 g/cm^3) and the reactor of interest.

Subsequent Monte Carlo calculations by Boden and Russell[2] have led to refinements of the Kinchin curve, and Fig 1.7 shows the damage absorption curve currently recommended for use in Magnox reactors, this curve also being based on a graphite density of 1.6 g/cm^3. The curve may be used to derive the value of an integrated damage function at any position in a Magnox reactor core taking account of varying source strengths, the distance from the various sources and the thickness of intervening graphite. The damage function so derived

enables the damage dose received by the graphite in a given time to be calculated, and this dose may in turn be used to evaluate the effect of fast neutron irradiation on the component in question. The calculation of damage function may be performed by hand calculation or by computer calculation using a code such as GRAFDAM which incorporates the damage absorption curve shown in Fig 1.7.

The damage function, df, for a single uniform line source is defined as:

$$df = (\phi(Rg)/R) \qquad (1)$$

where

Rg = equivalent thickness of BEPO graphite (density 1.6 g/cm^3) between the line source and the target, ins.

R = distance between line source and target, ins.

Φ(Rg) = damage absorption curve value from Fig 1.7 corresponding to intervening graphite thickness Rg.

For multi-source situations with sources of differing strengths,

$$df = \Sigma \left(\frac{Bi}{B} \cdot \frac{\phi(Rg)i}{Ri} \right) \qquad (2)$$

where

Bi = accumulated fuel burn-up of the ith source, MWd/t.

B = accumulated fuel burn-up of a reference source, MWd/t.

Φ(Rg)i = damage absorption curve value from Fig 1.7 corresponding to intervening graphite thickness Rg for the ith source.

Ri = distance between ith source and target.

The same equation may be used to calculate an integrated damage function value in AGRs, but here different damage absorption curves have been derived to represent the multi-pin fuel configuration of these reactors. Damage functions for AGRs are calculated by the FAIRY code using two different damage absorption curves, one representing the damage contribution from single pins within a fuel cluster contained within the target graphite brick, and another representing the contribution from all relevant channels outside the target channel, each fuel cluster being treated as a single line source located at the channel centre. Graphite damage

kernels for both source types, which may be used as input to FAIRY, have been derived by Boden and Russell[2].

5. Equivalent Rating and Dose

In order to correlate data obtained from several different experimental reactors, and to apply these data to the assessment of power reactors having various geometrical lattice arrangements and operating parameters, it is convenient to convert all fuel ratings and integrated doses to a common standard. The standard first adopted in the UK was the Calder equivalent rating and dose.

The Calder equivalent rating is defined as that fuel rating, Pe, in a Calder reactor which would produce the same rate of production of damage at a standard position as would be produced at the given position in the reactor under consideration where the fuel rating is P. The standard position chosen in Calder is the wall of a fuel channel 3.55 in diameter, in a lattice having a uniform square pitch of 8.0 in, containing fuel elements with a natural uranium rod diameter of 1.15 in, and at a point which lies on the line joining the centre of the fuel channel to its closest neighbour.

In reference 3, it is shown that:

$$Pe = \frac{A \cdot df \cdot P}{A_{Calder} \cdot df_{Calder}} \qquad (3)$$

where

Pe = Calder equivalent rating, MW/t

P = total local fuel rating in the reactor under consideration (ie including that proportion of channel heat output which appears in the graphite), MW/t

A = uranium cross-sectional area per channel in the reactor under consideration, in^2

A_{Calder} = uranium cross-sectional area per channel in Calder (= $1.04 in^2$)

df = damage function at the chosen point in the reactor under consideration (obtained from equation 2 above)

df_{Calder} = damage function at the standard position in Calder (= 1.395)

Substituting values gives:

$$Pe = 0.689 \,.\, A \,.\, df \,.\, P \qquad (4)$$

In reactors where fuel materials other than natural uranium are used it is necessary to apply a correction factor to the above relationship to allow for the fuel density change. Equation 4 then becomes:

$$Pe = 0.689 \,.\, A \,.\, df \,.\, P \,.\, \frac{\rho u}{18.78} \qquad (5)$$

where

ρu = grams of uranium in a cubic centimetre of fuel rod material in the reactor under consideration

18.78 = density of natural uranium, g/cm^3.

For Magnox reactors, ρu is taken to be 18.78 g/cm^3, whereas for AGRs, ρu has a recommended value of 9.388 g/cm^3.

Calder equivalent dose is obtained by multiplying rating values by the irradiation time in days. Thus,

$$De = 0.689 \,.\, A \,.\, df \,.\, B \,.\, \frac{\rho u}{18.78} \qquad (6)$$

where

De = Calder equivalent dose, MWd/t

B = accumulated fuel burn-up in reference fuel channel, MWd/t.

It is current practice to convert Calder equivalent doses to equivalent DIDO nickel doses (EDND, n/cm^2) since all graphite data are now presented as a function of EDND, largely because the majority of high dose data were obtained in the DIDO experimental reactor facility where damage fluxes and doses were measured by nickel foil activation. The conversion is made using the relationship[4].

$$EDND = 1.0887 \times 10^{17} \,.\, De \qquad (7)$$

Substituting in equation (6) gives:

$$EDND = 3.9942 \times 10^{15} \cdot A \cdot df \cdot B \cdot \rho u \quad (8)$$

6. WIMSE Code

The evaluation of damage doses (EDND, n/cm^2) using the damage function routines incorporated in GRAFDAM and FAIRY has now been superseded by use of the Winfrith code WIMSE which is capable of calculating damage doses directly. The WIMSE code is a powerful collection of methods for carrying out within core calculations on any thermal reactor type by solving the Boltzmann transport equation for the neutrons in the core. This includes all graphite moderated reactors. The code is the reference code for lattice cell calculations for all thermal reactor core calculations in the UK.

There is a variety of methods available within the code varying from simple modelling of fuel geometry in which the fuel is smeared out into a single central zone through to explicit modelling of the fuel pins, graphite sleeve and the graphite brick. All methods are linked to the same data library and this contains a response function for damage. Using this response function users can obtain damage anywhere in the structure. Calculations may consist of a single fuel channel and its associated graphite or an array of channels can be used. The choice of model is determined by the user.

7. Calder Effective Dose

During the early 1960's experimental data on stored energy and thermal conductivity changes were rather limited, and it became necessary to extrapolate the available data in order to make predictions for the higher irradiation doses appropriate to the Civil Magnox reactors. In order to make the required extrapolations it was necessary to establish a suitable correlation between the relevant parameters of dose, temperature and property change. It was well known that damage accumulation occurred at a slower rate when the irradiation temperature was increased, and a detailed study indicated that the data at different temperatures could apparently be made to correlate with a single curve if the Calder equivalent dose was reduced by a factor $R(\theta)$ which was temperature dependent. Thus, high irradiation temperatures required low values of $R(\theta)$ to reflect the slower rate of damage accumulation, and a single curve of property change versus Calder effective dose was produced in which the latter is defined as:

Calder effective dose = Calder equivalent dose x $R(\theta)$

where $R(\theta)$ is a function of Calder equivalent temperature as shown in Fig 1.8.

The assumption was made that a given property change would be reached regardless of temperature providing the irradiation damage dose was sufficiently high. This assumption is almost certainly pessimistic, particularly for higher irradiation temperatures where saturation in the build-up of stored energy and thermal conductivity changes appear to occur. Nonetheless, Calder effective dose has proved to be a very useful tool for correlating certain

property changes at low irradiation temperatures and its use persists to the present time. For most purposes, however, more reliable predictions can be obtained using the current improved data which are presented as curves of property change at various DIDO equivalent temperatures as a function of DIDO nickel dose.

8. Equivalent Temperature

It is now necessary to consider the net rate of production of damage in the graphite, ie the difference between the rate of production of damage and the rate of annealing of damage. The rate of annealing of damage increases with increase in temperature, but at any given temperature the amount of damage which is annealed decreases with increase in the rate of production of damage. In other words, annealing of damage is a function of both temperature and irradiation time, and if either of these parameters is reduced then less annealing of damage will occur.

In order to correlate data from a number of sources having widely different rates of production of damage and irradiation temperature, it is convenient to establish a standard rate of production of damage and to evaluate an equivalent temperature at which the graphite must be irradiated at this rate in order to produce the same net damage for a given total production of damage. The reference first chosen in the UK for this standard damage production rate is that rate of damage which would be produced at the standard position in Calder when the local fuel rating is 3.12 MW/t.

The Calder equivalent temperature is then defined as the temperature in a Calder reactor which, for a standard fuel rating of 3.12 MW/t would result in the same net damage at the standard position (see Section 5) as would be produced at the given position in the reactor under consideration, for the same total production of damage. The relationship is governed by the equation:

$$\frac{1}{Te} - \frac{1}{Ti} = \frac{k}{E} \log_e \left(\frac{Pe}{3.12}\right) \qquad (9)$$

where

Te = Calder equivalent temperature, K

Ti = irradiation temperature in reactor under consideration, K

k = Boltzmann's constant (= 8.617×10^{-5} eV/K)

E = Activation energy (usually taken as 1.2eV for low dose effects such as initial increase in Young's modulus and thermal resistivity, but a value of 3.0eV is considered more appropriate when the effects of high dose structural changes become important).

Pe = Calder equivalent rating at selected point in reactor under consideration, MW/t.

From equation 9 it can be shown that values of Pe greater than 3.12 MW/t would necessitate irradiation in Calder at a lower temperature than Ti in order to achieve the same net damage, and vice versa.

As in the case of equivalent doses (see Section 5) it is now more usual practice to refer equivalent temperatures to a standard position in DIDO where the Equivalent DIDO Nickel Dose Rate is 4×10^{13}n/cm^2.s. This is again because the large majority of high dose data has emanated from DIDO, and the resultant database uses DIDO equivalent temperatures calculated at this standard position in DIDO. The appropriate relationship for calculating DIDO equivalent temperatures is:

$$\frac{1}{\theta} - \frac{1}{Ti} = \frac{k}{E} \log_e \left(\frac{\phi}{4 \times 10^{13}} \right) \qquad (10)$$

where

θ = DIDO equivalent temperature, K

Φ = equivalent DIDO nickel dose rate at selected point in reactor under consideration, n/cm^2.s. Ti, k and E are as defined in equation (9).

9. Important Reactor Parameters

The damage dose (De, MWd/t) or (EDND, n/cm^2) should be calculated using equations (6) and (8), respectively, when the reference fuel burn-up (B, MWd/t) is calculated as follows:

(a) For predicting material property changes, self-stress and cross-sectional dimensional changes:

$$B = B_\ell$$

where B_ℓ = local fuel burn-up over life

(b) For predicting column length changes:

$$B = B_{mc} \cdot L_f/L_c$$

where B_{mc} = mean fuel burn-up in channel over life

L_f = total length of fuel in channel

L_c = length of column in active core

(c) For predicting brick length changes:

$$B = B_{mb} \cdot L_f'/L_b$$

where B_{mb} = mean burn-up of fuel located in brick bore

L_f' = length of fuel within brick

L_b = length of brick

References

1. Bell J C, Bridge H, Cottrell A H, Greenough G B, Simmons J H W and Reynolds W N. Phil Trans Roy Soc A254, p361 (1962).

2. Boden W A and Russell P D D. Mk II graphite damage in a flux gradient. APC/R1424 (1972).

3. Prince N. The calculation of stored energy and thermal conductivity changes in graphite due to neutron irradiation. TRG Report 388(R).

4. Compendium of CAGR core and sleeve data and methods. CSDMC/P28.

Table 1.1

Comparison of Properties* of Pile Grade A and Gilsocarbon Graphite

Property	Units	Pile Grade A (Hexagonal symmetry)	Gilsocarbon graphite (Isotropic)
Density	$g.cm^{-3}$	1.74	1.810
Open pore volume	$cm^3.cm^{-3}$	0.198	0.11
Closed pore volume	$cm^3.cm^{-3}$	0.01	0.086
Thermal Expansion Coefficient K^{-1} (20-120°C)		Parallel to extrusion $0.9x10^{-6}$ Perpendicular to extrusion $2.8x10^{-6}$	$4.3x10^{-6}$
Thermal conductivity $w.m^{-1}K^{-1}$ (20°C)		Parallel to extrusion 200 Perpendicular to extrusion 109	131 -
Young's Modulus (20°C)	GNm^{-2}	Parallel to extrusion 11.7 Perpendicular to extrusion 5.4	10.85 -
Strength Tensile	$MN.m^{-2}$	Parallel to extrusion 17 Perpendicular to extrusion 11	17.5 -
Bend	$MN.m^{-2}$	Parallel to extrusion 19 Perpendicular to extrusion 12	23.0 -
Compression	$MN.m^{-2}$	Parallel to extrusion 27 Perpendicular to extrusion 27	70.0 -
Poisson's ratio		Multiple values ~ 0.07	0.21
Electrical resistivity μ ohm.cm^{-1}		Parallel to extrusion 620 Perpendicular to extrusion 1100	900 -
Diffusivity		$13.6x10^{-3}$	$3x10^{-3}$
Permeability			
Viscous flow coeff B_o m^2		Parallel to extrusion $712x10^{-16}$ Perpendicular to extrusion $147x10^{-16}$	$6.5x10^{-15}$
Slip flow coeff K_o m		Parallel to extrusion $108x10^{-9}$ Perpendicular to extrusion $21x10^{-9}$	$5.8x10^{-9}$

* These properties are representative of the materials but do not represent mean values.

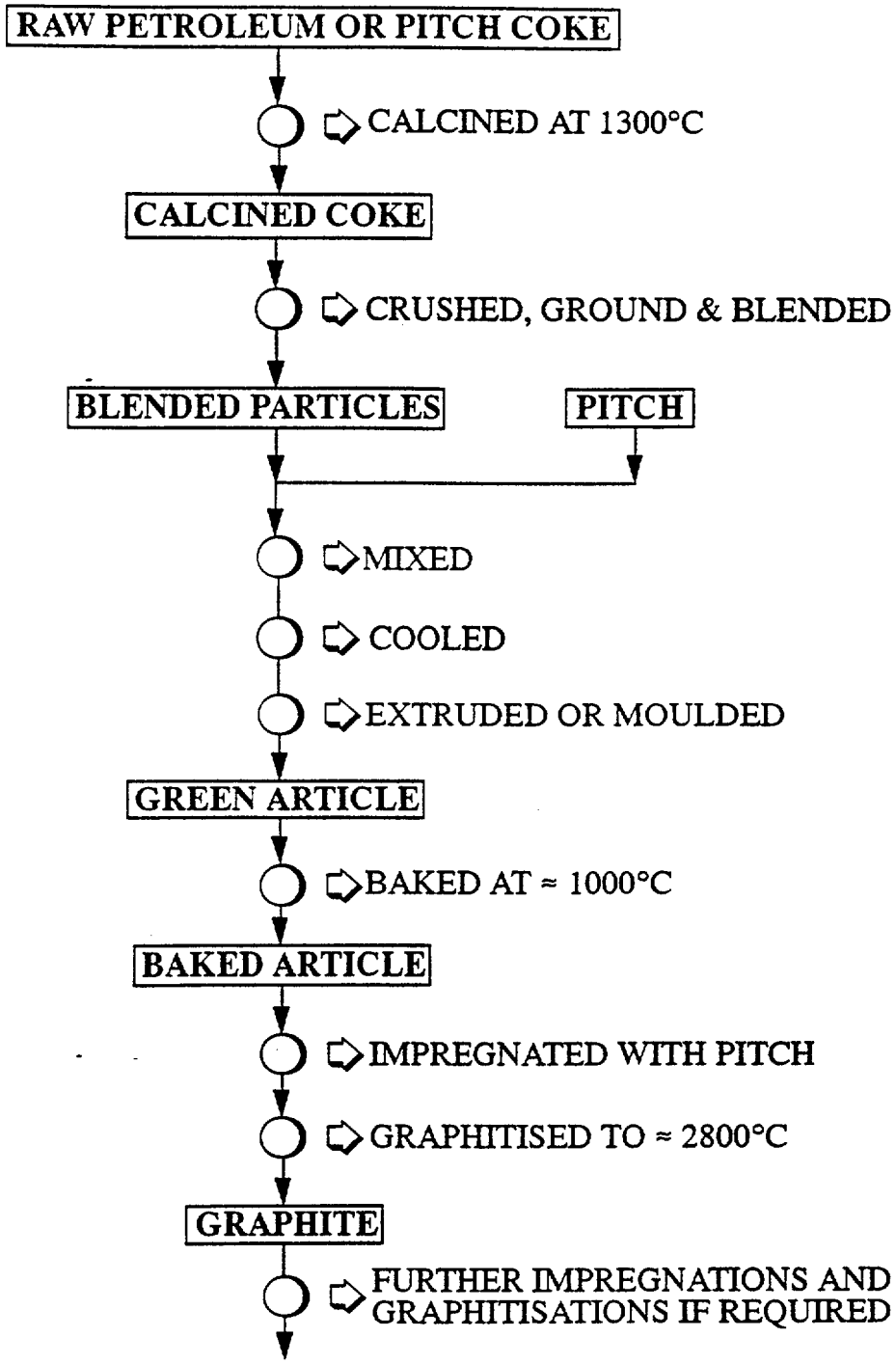

Figure 1. Materials and Process used in Graphite Manufacture

Figure 2. Polarised Light Micrograph of British Reactor Grade 'A' Graphite Cut Parallel to Extrusion. (Scale 185 microns to 1 cm)

Figure 3. Polarised Light Micrograph of IM1-24 (Gilso Carbon) Graphite. (Scale 185 microns to 1 cm)

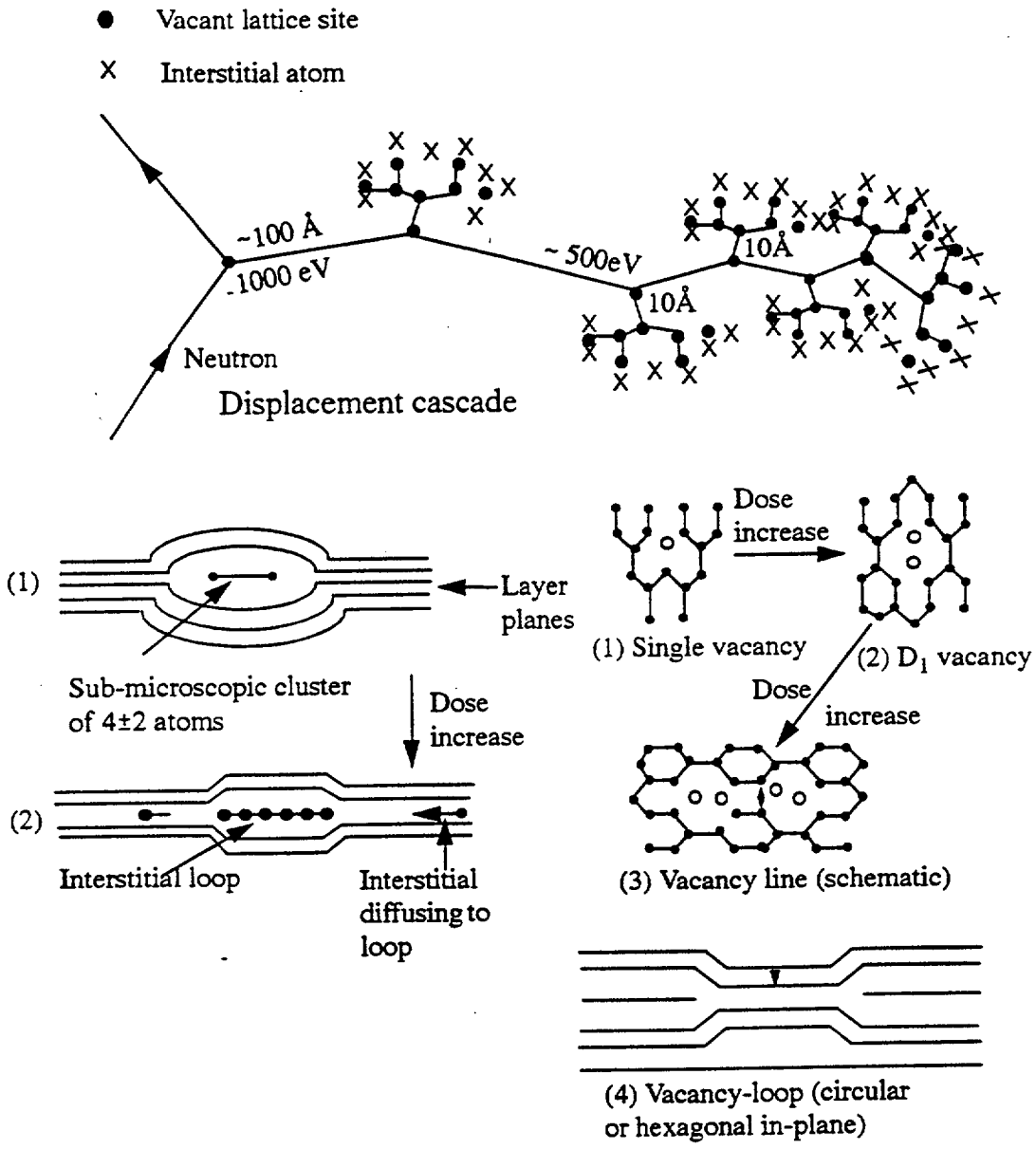

Figure 4. Lattice defects in graphite introduced by radiation

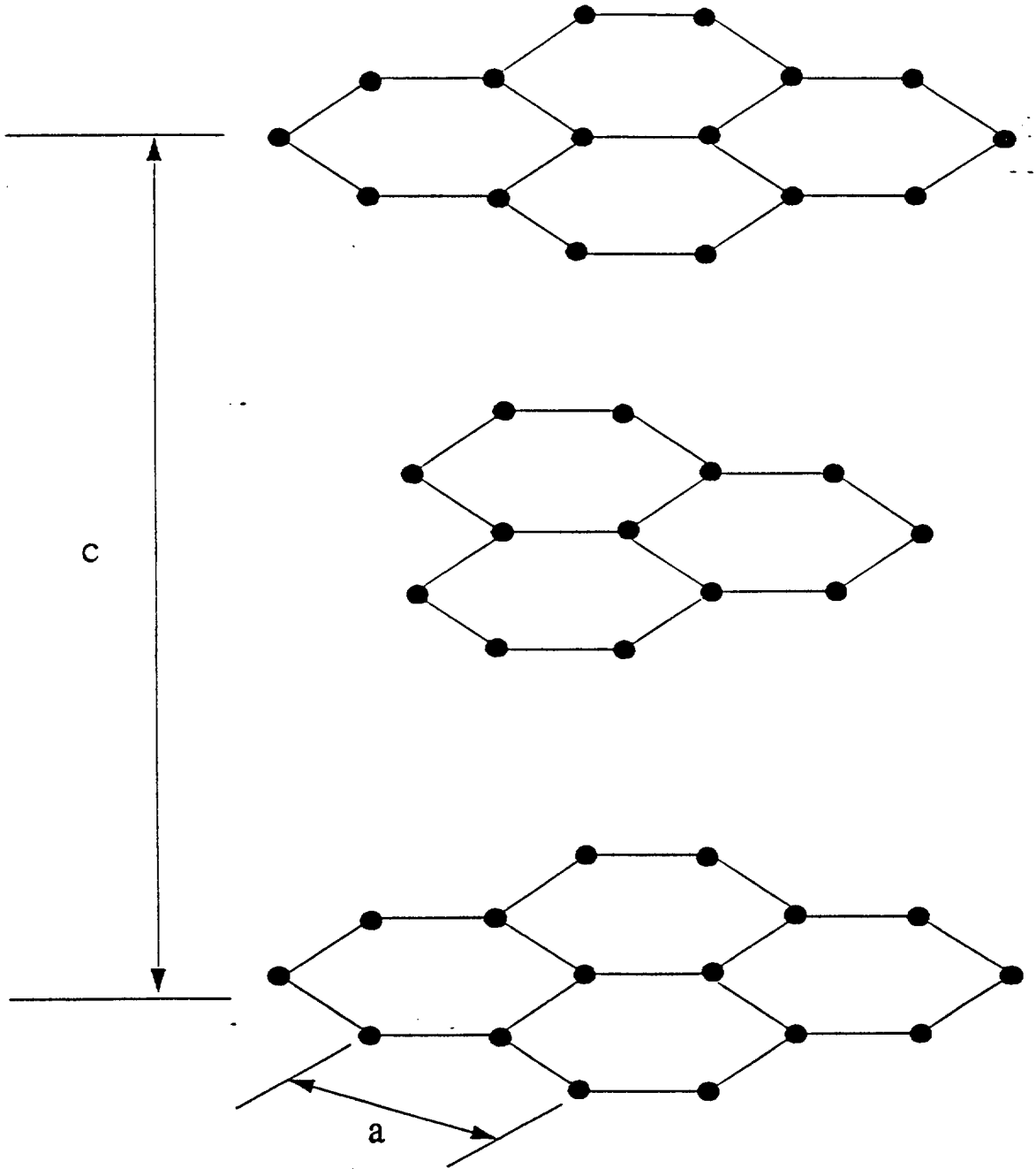

Figure 5. The Graphite Crystal Lattice

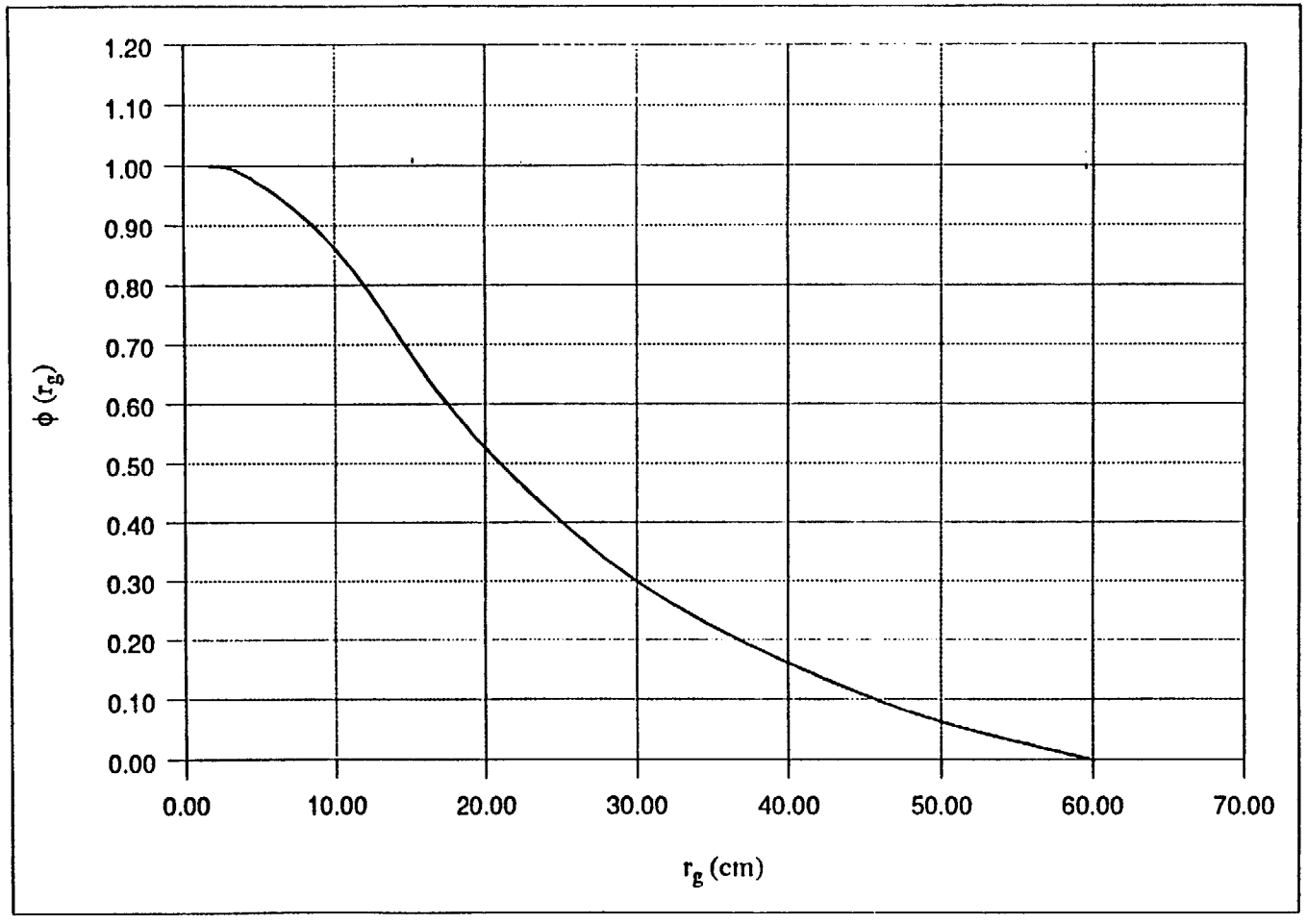

Figure 6. Variation of Graphite Damage Flux with Distance Through Graphite

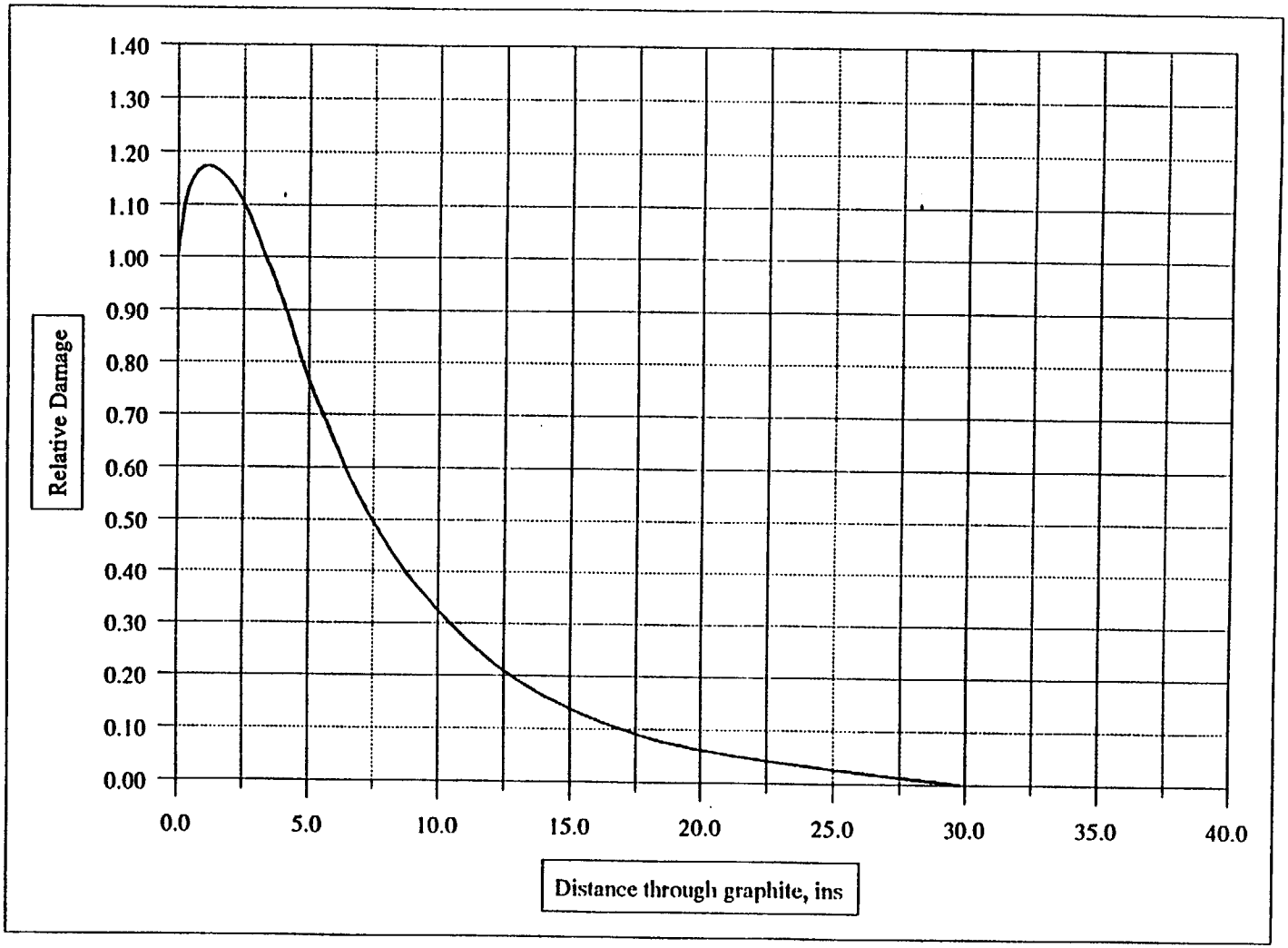

Figure 7. Relationship Between Graphite Relative Damage and Distance

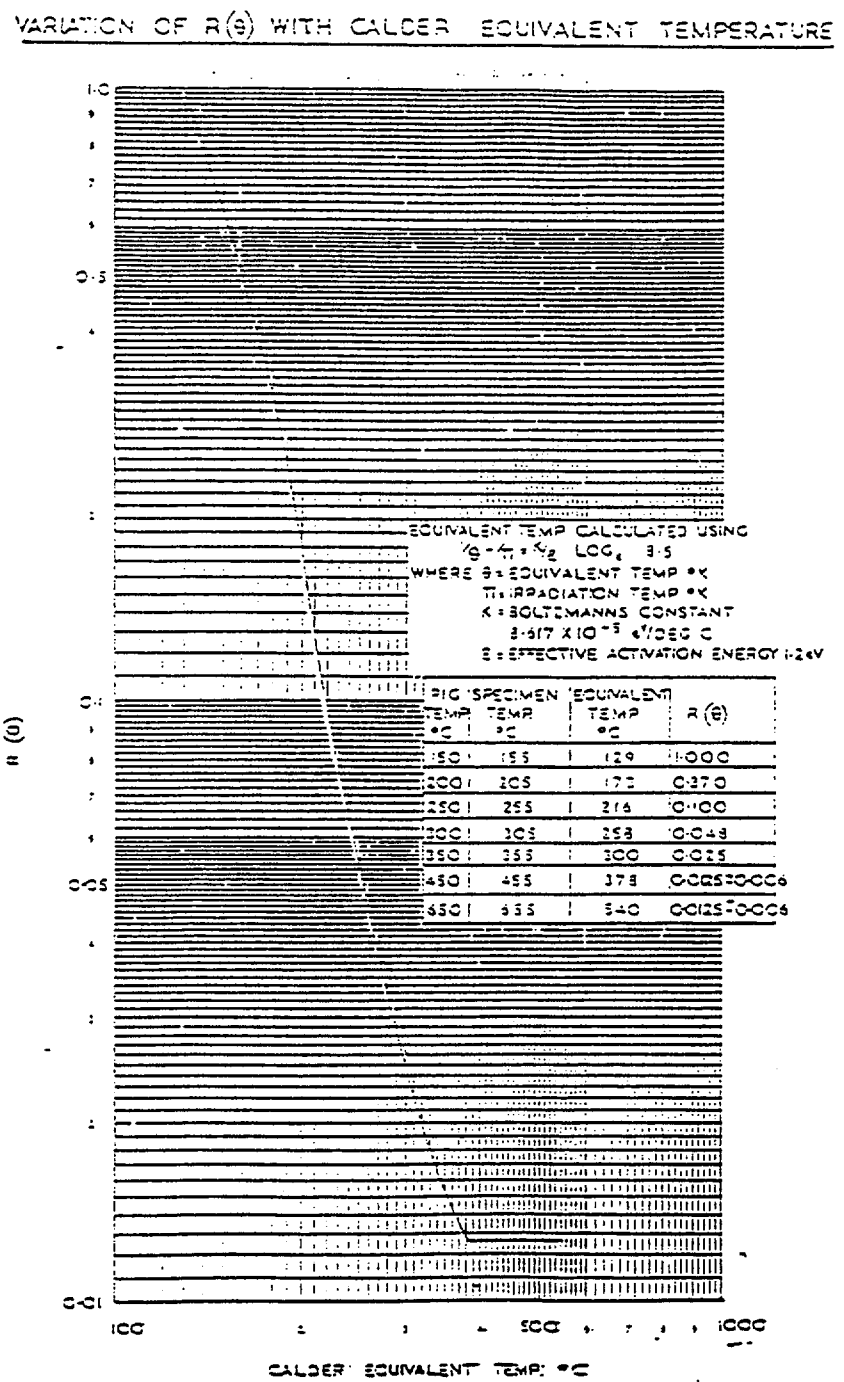
VARIATION OF R(θ) WITH CALDER EQUIVALENT TEMPERATURE
EQUIVALENT TEMP CALCULATED USING
WHERE θ = EQUIVALENT TEMP °K
Ti = IRRADIATION TEMP °K
K = BOLTZMANNS CONSTANT
8·617 X 10⁻⁵ eV/DEG C
E = EFFECTIVE ACTIVATION ENERGY 1·2eV
PIG SPECIMEN EQUIVALENT
TEMP TEMP TEMP R(θ)
°C °C °C
50 155 129 1·000
100 205 173 0·270
250 255 216 0·100
300 305 258 0·048
350 355 300 0·025
450 455 378 0·025-0·006
650 655 540 0·025-0·006
R (θ)
1·0
0·5
0·1
0·05
0·01
100
500
1000
CALDER EQUIVALENT TEMP: °C

Figure 8.

GRAPHITE TECHNOLOGY COURSE

LECTURE 2

1. Effect of Fast Neutron Irradiation

The dimensional and physical property changes which occur in graphite due to the combined effects of fast neutron irradiation and radiolytic weight loss are very complex and do not always conform to a logical pattern. The magnitude of the changes is different for each graphite type and method of manufacture, some graphites exhibiting highly anisotropic behaviour whilst others are completely isotropic. Interpretation of the available data on any given graphite often presents difficulties, not only in terms of mean behaviour and scatter about the mean, but also in terms of extrapolating the available experimental data to reactor lifetime exposure values.

Notwithstanding these difficulties, agreed interpretations and extrapolations of the available data on PGA and Gilsocarbon graphites do exist in the form of data manuals and reports, and these are continually updated in line with the latest thinking, observations and requirements in this technological field. For all practical applications it is therefore essential that the data user should make reference to the latest data manual or report when attempting to evaluate the dimensional or property change of any given graphite and to confirm from an appropriate specialist in the graphite field that the recommendation is current.

The methodology employed in the evaluation of dimensional and property changes is also very complex and highly detailed. Great care is required when using the methodology to ensure that all known factors have been taken into account and correctly applied. Some of the changes are a function of several variables (such as dose, equivalent temperature, absolute temperature and weight loss) some of which are interdependent with one another. The irradiation conditions may also vary during reactor life, and this must be taken into consideration when the effects of in-pile exposure are evaluated.

As with graphite data, the rules employed in graphite methodology also appear in data manuals and reports, and these cover both PGA and Gilsocarbon graphites where different rules apply. Here again it is essential that the user should seek the advice of a graphite specialist to ensure that the latest endorsed methodology is used for each application.

The graphite database and methodology rules are indeed so extensive and detailed that it would be practically impossible within the available space of these lecture notes to summarise them in a manner that would permit them to be used in practical assessments. The following notes are intended as a general guide to the graphite data and the methodology used in PGA and Gilsocarbon component and structural assessments, with emphasis placed on summarising the graphite data and the most important rules employed in the methodology. A brief synopsis of the data and methodology used to evaluate each of the various changes induced in both PGA and Gilsocarbon graphites is given below.

2. Dimensional Changes

As was mentioned in Lecture 1, radiation damage by fast neutrons causes carbon atoms to be displaced into interstitial positions where they form interstitial loops which push the carbon atom layers apart, resulting in crystal growth in the c-axis direction. The displaced atoms leave behind vacancies which form vacancy lines, and these result in crystal shrinkage in the a-axis direction. This behaviour continues over all measured doses. Between room-temperature and 300°C there are large changes in crystal volume, this volume change being associated with stored energy. Above 300°C the graphite crystals change shape with little or no change in volume.

During the manufacture of polycrystalline graphites, because of the large anisotropy of thermal expansion in the graphite crystal a and c directions, intercrystalline cracks are formed as the graphite cools after graphitisation. This leads to the formation of microporosity within the graphite structure. These imperfections are usually referred to as Mrosowski cracks after the scientist who suggested that mechanism by which they are formed. This microporosity is the reason for the lower density of bulk graphite (1.70 to 1.80 g/cm^3) when compared with the crystal density (2.23g/cm^3). During irradiation, part of the c-axial crystal growth can be accommodated by the pore space available within the Mrosowski cracks.

Since PGA is an extruded graphite manufactured from needle-shaped petroleum coke particles, the graphite tends to have the crystal basal planes aligned parallel to the extrusion axis. As a result, between 150°C and 300°C PGA behaves in a similar manner to the crystal, growing perpendicular to the extrusion direction and shrinking parallel to the extrusion direction. The changes in crystal dimensions can be very large as may be seen in Fig 2.1 which presents data on pyrolytic graphite where the carbon atom layers are highly orientated. As will be seen later, the dimensional changes of PGA graphite are significantly smaller because the crystal layers in nuclear graphite are more randomly orientated. Above 300°C PGA shrinks both parallel and perpendicular to extrusion.

Gilsocarbon graphite on the other hand, being moulded and made from coke containing spherical structures in which the graphite crystallites tend to lie in an "onion skin" structure, has very isotropic properties. As a result, the dimensional changes in the parallel and perpendicular directions to the direction of moulding are the same. At all temperatures of practical interest, ie 300°C and above, Gilsocarbon graphite exhibits initial shrinkage during which stage any c-axis growth is accommodated by a-axis shrinkage and voidage available in the microporosity. This process continues until all the microporosity has been taken up and the graphite begins to swell, this point being known as "turnaround". Radiolytic oxidation increases the microporosity of graphite and is predicted to delay turnaround in Gilsocarbon graphite. The effect of radiolytic oxidation on the dimensional changes of PGA graphite is considered to be negligible.

2.1 Data and Methodology - PGA Dimensional Changes

Figs 2.2 and 2.3 summarise the dimensional change data for PGA graphite obtained from

high flux irradiation experiments in DIDO[1]. Dimensional change, %, is plotted as a function of equivalent DIDO nickel dose (EDND), n/cm^2, for DIDO equivalent temperatures ranging from 150 to 650°C. Fig 2.2 shows that shrinkage occurs parallel to extrusion at all temperatures, and that shrinkage rate generally decreases with increase in temperature. Fig 2.3 shows that at temperatures below about 300°C graphite grows perpendicular to extrusion, the growth rate increasing with decrease in temperature. At temperatures between 300 and 650°C initial shrinkage in the perpendicular direction is followed later by growth.

For PGA dimensional changes, DIDO equivalent temperatures are calculated using an activation energy of 1.2eV[1]. Radiolytic weight loss should be assumed to have no effect on dimensional changes.

2.2 Data and Methodology - Gilsocarbon Dimensional Changes

The solid lines in Fig 2.4[2] are the recommended mean dimensional change curves for Gilsocarbon graphite in the absence of radiolytic oxidation as a function of dose (EDND) n/cm^2 at DIDO equivalent temperatures of 350, 450 and 550°C. The dotted lines in Fig 2.4 present the corresponding recommended "free" shrinkage curves in the absence of shrinkage reversal as would be expected to occur in the presence of very high rates of radiolytic oxidation when creation of microporosity would delay the onset of turnaround. The dimensional changes are applicable to both parallel and perpendicular directions to the direction of moulding. It will be seen that the initial shrinkage rate increases with increase in temperature, and that in the absence of radiolytic oxidation the onset of turnaround occurs earlier the higher the irradiation temperature.

In practice the dimensional change curves will be somewhere between the extreme values represented by the solid and dotted lines in Fig 2.4 since the radiolytic oxidation rate will be finite but small. In Gilsocarbon graphite, the rate of radiolytic oxidation is inhibited by the planned inclusion of methane and carbon monoxide as constituents in the coolant gas, thereby suppressing oxidation in the majority of the micropores. Since radiolytic oxidation is confined to what are referred to as the "reactive pores", a method of calculation has been devised whereby an intermediate curve may be evaluated between the solid and dotted lines by assuming that the intermediate curve is situated at a fractional distance between them represented by the ratio: initial reactive pore volume, V_{RPV}, divided by initial total open pore volume, V_{TOT}, in accordance with the equation:

$$\textit{Dimensional change, \%} = \left(\frac{V_{RPV}}{V_{TOT}}\right) \textit{Curve A} + \left(1 - \frac{V_{RPV}}{V_{TOT}}\right) \textit{Curve B} \qquad (1)$$

Curve A is the dotted line in Fig 2.4
Curve B is the solid line in Fig 2.4
V_{RPV} is the initial reactive pore volume (at zero time) in which all of the radiolytic oxidation is assumed to occur, cm^3/cm^3.
V_{TOT} is the initial (unirradiated) total open pore volume cm^3/cm^3.

The initial reactive pore volume is assumed to be directly proportional to the initial radiolytic oxidation rate, and from experimental data it has been determined that V_{RPV} should be evaluated from the equation:

$$V_{RPV} = 0.15\ 10^{8}\ RR \qquad (2)$$

where:

RR is the initial radiolytic oxidation rate at 673°K and 41 bar, g/g, hr (mW/g), and is coolant composition dependent as defined by the expression:

$$RR = [\ Ae^{-k(CH4)} + 0.05\ ]\ 10^{-8} \qquad (3)$$

where:

(CH4) is the in-pore methane concentration, vpm A and k are constants taken from the following table:

CO%	A	k
0.25	0.772	9.69×10^{-3}
0.5	0.591	6.85×10^{-3}
0.75	0.455	5.94×10^{-3}
1.0	0.361	5.30×10^{-3}
1.5	0.262	4.18×10^{-3}
2.0	0.220	3.27×10^{-3}
2.5	0.197	2.48×10^{-3}

Table 2.1 and Fig 2.5 give values of RR for a convenient range of CO and CH_4 values.

For Gilsocarbon graphite, DIDO equivalent temperatures are calculated using an activation energy of 3.0eV[2].

3. Coefficient of Thermal Expansion

The coefficient of thermal expansion (CTE) as used in the UK nuclear industry is usually measured in the range 20-120°C. The volume expansion of bulk graphite is much less than the volume of the crystal, largely due to the accommodation of crystal expansion by microporosity. The variation of the component crystal coefficients of thermal expansion α_a and α_c has been studied by irradiating highly oriented pyrolytic graphite. This shows that below ~300°C α_c decreases from $26 \times 10^{-6}\ K^{-1}$ to $14 \times 10^{-6}\ K^{-1}$ while α_a changes from $-1.25 \times 10^{-6}\ K^{-1}$ to $\sim+1 \times 10^{-6}\ K^{-1}$ over the same temperature range. Above ~300°C both α_c and α_a remain close to unirradiated values.

The CTE of PGA graphite exhibits orthotropic behaviour with $\alpha_{(20\text{-}120)}$ perpendicular to extrusion significantly higher than that parallel to extrusion, the respective values being $\sim 2.8 \times 10^{-6}$ and $0.9 \times 10^{-6}\ K^{-1}$. Gilsocarbon graphite on the other hand exhibits isotropic behaviour with respect to the expansion coefficient, $\alpha_{(20\text{-}120)}$ being significantly higher at $\sim 4.3 \times 10^{-6}\ K^{-1}$.

Clearly both graphites have much lower CTE values than the α_c value of $\sim 26 \times 10^{-6}\ K^{-1}$ measured in highly oriented pyrolytic graphite.

The changes in CTE with irradiation of bulk graphite are a complex function of the changes which take place within the crystal and within the structure of the graphite which are not fully understood. PGA generally shows an increase in expansion coefficient with irradiation in both perpendicular and parallel directions to extrusion, the increase being more rapid and to a higher level the lower the irradiation temperature. Gilsocarbon graphite, on the other hand, exhibits a significant reduction in expansion coefficient with irradiation following a smaller increase at low doses.

It is important to note that the thermal expansion coefficient of graphite is temperature dependent and exhibits a significant rise in expansion coefficient with increase in temperature. Values determined in the temperature range 20-120°C following fast neutron irradiation must therefore be adjusted to allow for this increase. It has been shown experimentally that the instantaneous coefficient of thermal expansion (CTE), α_i, can be determined from the CTE value measured in the range 20-120°C, $\alpha_{(20\text{-}120)}$, using the relationship:

$$\alpha_i = Ai.\alpha_{(20\text{-}120)} + Bi \qquad (4)$$

where Ai and Bi are dependent on temperature only, ie equation (4) is applicable to both unirradiated and irradiated graphite.

The parameter Ai may be taken as unity for all temperatures of practical interest (in both Magnox and AGRs). The parameter Bi as a function of temperature is shown in Fig 2.6.

The mean CTE over the temperature range 20 to T°C , $\alpha_{(20\text{-}T)}$ is of more practical use than the instantaneous coefficient, α_i, and may be obtained from the relationship

$$\alpha_{(20\text{-}T)} = \frac{1}{(T-20)} \int_{20}^{T} \alpha_i \, . \, dT \qquad (5)$$

$$= \frac{1}{(T-20)} \int_{20}^{T} (\alpha_{(20\text{-}120)} + Bi) \, . \, dT \qquad (6)$$

$$ie \quad \alpha_{(20\text{-}T)} = \alpha_{(20\text{-}120)} + \overline{B}_i \qquad (7)$$

where is the mean value of B_i over the temperature range 20-T°C.

Figure 2.7 has been produced using equation 7 for discrete values of $\alpha_{(20\text{-}120)}$ between 1.5 x 10^{-6} and 5.5 x 10^{-6} °C^{-1}, and gives mean CTE values in the range 20 to T°C for T values up to 750°C.

3.1 Data and Methodology - PGA Coefficient of Thermal Expansion

Figures 2.8a and 2.8b summarise the PGA experimental data[1] on $\alpha_{(20\text{-}120)}$ changes as a function of dose (EDND), n/cm^2, for DIDO equivalent temperatures in the range 150 to 650°C. At the lower irradiation temperatures there is a rapid rise in expansion coefficient in both parallel and perpendicular directions to extrusion. As the irradiation temperature increases so the dose at which the thermal expansion begins to rise increases. Furthermore, the level to which it rises decreases with irradiation temperature.

For PGA graphite, the irradiation-induced changes in $\alpha_{(20\text{-}120C)}$ are evaluated from Figs 2.8a and 2.8b using DIDO equivalent temperatures calculated with an activation energy of 1.2eV[1]. The changes so evaluated are additive to the unirradiated $\alpha_{(20\text{-}120)}$ value for the graphite under consideration. However, irradiated thermal expansion values may be read directly from Figs 2.8a and 2.8b if unirradiated values are not significantly different from the starting values shown (0.8 x 10^{-6} and 3.0 x 10^{-6},°C^{-1}). Radiolytic weight loss effects on CTE should be assumed to be insignificant.

Adjustments for temperature dependence of CTE are as detailed in Section 3 above.

3.2 Data and Methodology - Gilsocarbon Coefficient of Thermal Expansion

Figure 2.9a shows the recommended mean curves for calculating the changes in $\alpha_{(20\text{-}120)}$ of Gilsocarbon graphite as a function of dose (EDND) n/cm^2 at DIDO equivalent temperatures of 350, 400, 450, 500 and 550°C. The initial rise in CTE is temperature dependent, the level to which it rises decreasing with increase in irradiation temperature. The subsequent fall in CTE with dose also occurs earlier with increase in irradiation temperature. As for PGA, the evaluated change in CTE is additive to the unirradiated $\alpha_{(20\text{-}120)}$ value for the graphite under consideration, but irradiated values may be read directly from Fig 2.9a if unirradiated CTE is not significantly different from the shown starting value of 4.35 x 10^{-6},°C^{-1}.

For AGR applications, a small additional correction to the irradiated $\alpha_{(20\text{-}120)}$ value is recommended to allow for a dependence on local strain. The sum of the elastic and creep strains should be evaluated and used to determine the appropriate correction from Fig 2.9b which is directly additive to the irradiated value. The correction leads to an increase in $\alpha_{(20\text{-}120)}$ for compressive strains and a decrease for tensile strains.

The irradiation-induced changes in $\alpha_{(20\text{-}120)}$ for Gilsocarbon graphite are evaluated from Fig 2.9a using DIDO equivalent temperatures determined using an activation energy of 3.0eV. It has been found that radiolytic oxidation of Gilsocarbon does not produce significant changes in CTE.

As for PGA, adjustments for temperature dependence of CTE are as detailed in Section 3.

4. Thermal Conductivity

The principal thermal conductivities of the graphite crystal, that is K_a parallel to the basal planes and K_c perpendicular to them, are dominated by phonon lattice wave conduction. The presence of lattice defects introduced by irradiation damage reduces both principal conductivities, but for most polycrystalline graphites the conductivities are dominated by the component K_a because $K_a >> K_c$. As will be seen later, further reductions in thermal conductivity may also occur as a result of pore opening due to radiolytic oxidation and pore generation at high doses due to crystal straining after turnaround.

The data are traditionally presented in terms of the fractional change in thermal resistivity measured at room temperature. However, in practice it is the thermal resistivity at the operating temperature which is required, and so it is necessary to develop an appropriate relationship from which this may be evaluated. The thermal resistance of irradiated graphite is given by:

$$\frac{1}{K(T)} = \frac{1}{K_o(T)} + \frac{1}{K_i(T)} \tag{8}$$

where

$\frac{1}{K(T)}$ = Irradiated thermal resistance at T°C

$\frac{1}{K_o(T)}$ = Unirradiated thermal resistance at T°C

$\frac{1}{K_i(T)}$ = Thermal resistance at T°C introduced by fast neutron irradiation

It is convenient to introduce thermal resistance at 30°C and consider ratios:

$$\frac{K_o(30)}{K(T)} = \frac{K_o(30)}{K_o(T)} + \frac{K_o(30)}{K_i(T)} \tag{9}$$

$$\frac{K_o(30)}{K(T)} = \frac{K_o(30)}{K_o(T)} + \frac{K_o(30)}{K_i(30)} \cdot \frac{K_i(30)}{K_i(T)} \tag{10}$$

The first term in equation 10 involves unirradiated values and depends on temperature only. The ratio $K_i(30)/K_i(T)$ has been shown to be dependent on temperature only. The ratio $K_o(30)/K_i(30)$ involves measurements at 30°C after irradiation at specified conditions and is shown to be dependent upon dose and DIDO equivalent temperature.

Two additional factors need to be introduced into equation 10 to account for structural changes in the graphite following turnaround and to account for pore opening effects due to radiolytic weight loss. The final equation for the thermal resistance of irradiated and oxidised graphite at T°C then becomes:

$$\frac{1}{K(T)} = \frac{1}{K_o(30)}\left[\frac{K_o(30)}{K_o(T)} + f.\delta T\right] S_k \left[\frac{K_o}{K}\right]_{ox} \qquad (11)$$

where:

$$f = \frac{K_o(30)}{K_i(30)} = \left[\frac{K_o(30)}{K(30))} - 1\right]$$

$$\delta(T) = \frac{K_i(30)}{K_i(T)}$$

S_K = Structural factor to allow for structural changes following turnaround.

$\left[\frac{K_o}{K}\right]_{ox}$ = Factorial increase in thermal resistance due to radiolytic weight loss.

Equation 11 is a general relationship which may be used to evaluate the thermal resistance of irradiated and oxidised graphite, 1/K(T), at any desired temperature up to the irradiation temperature; above this temperature changes in thermal resistance may occur due to annealing.

4.1 Data and Methodology - PGA Thermal Conductivity

The data from which the various parameters in equation 11 may be obtained in order to evaluate the thermal conductivity of irradiated and oxidised PGA graphite, K(T), are

summarised in Figs 2.10, 2.11, 2.12 and 2.13.

Fig 2.10 shows the fractional changes in thermal resistance, f, (= $K_o(30)/K(30)-1$), as a function of neutron dose for different irradiation temperatures from 150 to 650°C (DIDO equivalent). The changes are strongly temperature dependent with the largest increases occurring at the lower irradiation temperatures.
Fig 2.11 gives the temperature dependence of thermal conductivity ($K_o(T)/K_o(30)$) for unirradiated PGA graphite.

Fig 2.12 gives the temperature dependence of thermal resistivity, δT, for irradiated PGA graphite.

The structure term S_k is unity for PGA graphite applications.

Fig 2.13 shows the data on the change in thermal resistivity with radiolytic weight loss for PGA graphite from which use of the relationship $[K_o/K]_{ox} = e^{3.1x}$ is recommended, where x is the fractional weight loss.

When Fig 2.10 is used to determine the fractional change in thermal resistance of PGA graphite, DIDO equivalent temperatures are calculated using an activation energy of 1.2eV.

4.2 Data and Methodology - Gilsocarbon Thermal Conductivity

The parameters in equation 11 for evaluating the thermal conductivity of Gilsocarbon graphite in the irradiated and radiolytically oxidised condition may be obtained from Figs 2.14 to 2.19, inclusive..

Fig 2.14 shows curves of f as a function of dose for DIDO equivalent temperatures ranging from 325 to 550°C. It can be seen that f increases with dose, eventually reaching a saturation level which reduces with increase in irradiation temperature.

Fig 2.15 gives the relationship between ($K_o(T)/K_o(30)$) and temperature for Heysham II/Torness Gilsocarbon graphite.

Fig 2.16 gives the same relationship for Gilsocarbon graphite in all other AGRs.

Fig 2.17 shows the temperature dependence δT for all irradiated Gilsocarbon graphites.

Fig 2.18 shows the structure term S_k as a function of dose for DIDO equivalent temperatures in the range 350 to 550°C.

Fig 2.19 shows the data on the change in thermal resistivity with weight loss for Gilsocarbon graphite from which use of the relationship $[K_o/K]_{ox} = e^{2.7x}$ is recommended, where x is the fractional weight loss.

DIDO equivalent temperatures used to derive thermal resistivity changes should be calculated

using the following activation energy values:

f should be determined from Fig 2.14 using 1.2eV.

S_k should be determined from Fig 2.18 using 3.0eV.

5. Stored Energy

The crystal lattice of virgin graphite possesses the lowest potential energy of the constituent atoms, and the presence of irradiation-induced defects increases the total energy. If the temperature of irradiated graphite is raised above the irradiation temperature, the lattice defects reduce their energy by mutual annihilation and the excess energy appears as heat. This phenomenon, known as stored energy, was first predicted in 1943 by the physicist E P Wigner and is sometimes referred to as Wigner energy.

Stored energy may be characterised by several parameters of which the most commonly used are the total stored energy, E, and the rate of release of stored energy, dE/dT. As dE/dT is dimensionally equivalent to specific heat (J/g.K) its use permits a rapid assessment of the thermal stability of the graphite to be made. For fault study purposes it is assumed that the irradiation temperature must be exceeded by 50°C before significant energy release commences. At higher temperatures the release rate, dE/dT goes through a maximum $(dE/dT)_{max}$ after which a reduction to lower levels may occur, although some high temperature measurements show shallow peaks.

The magnitude of both E and $(dE/dT)_{max}$ are dependent upon the irradiation damage dose and the DIDO equivalent temperature. Their magnitude is directly related to the fractional change in resistivity, f, measured at room temperature. The following relationships were obtained from experiments on PGA graphite. It is important to note that they do not apply to graphite irradiated at the lower temperatures pertaining to the Windscale Piles.

$$E = 31.1 f \qquad (12)$$

and

$$\left(\frac{dE}{dT}\right)_{max} = \frac{E}{1910} \qquad (13)$$

where

$$f = \left[\frac{K_o(30)}{K(30)} - 1\right]$$

= Irradiation induced fractional change in thermal resistivity measured at room temperature.

E = Total stored energy, J/g.

$(dE/dT)_{max}$ = Maximum rate of release of stored energy, J/g°C.

5.1 Data and Methodology - PGA Stored Energy

The fractional change in thermal resistivity, f, should be determined from Fig 2.10, with DIDO equivalent temperatures obtained using an activation energy of 1.2eV. No adjustments to either E or $(dE/dT)_{max}$ are required for structural changes or radiolytic weight loss.

5.2 Data and Methodology - Gilsocarbon Stored Energy

Formal recommendations assume the use of PGA data.

6. Specific Heat

The specific heat of graphite varies with temperature in a unique relationship which is the same for all well graphitised nuclear graphites. The relationship is shown in Fig 2.20.

It should be assumed that the specific heat is not changed by fast neutron irradiation and is unaffected by graphite structural changes and radiolytic weight loss.

7. Young's Modulus

The stress-strain curves for unirradiated graphite in both tension and compression are non-linear, the material exhibiting hysteresis on unloading after which there is permanent set, Fig 2.21. The value of Young's modulus will therefore depend upon stress level and will be less than the dynamic modulus at significant strains. However, if the static modulus is measured at a low enough strain the static and dynamic values should be the same. Following irradiation the stress-strain curves become more linear and the permanent set is decreased, the strains to failure decrease, but the Young's moduli and strengths increase considerably. Experiments to determine the magnitude of irradiation-induced changes in Young's modulus have concentrated on dynamic modulus as the basis of measurement.

In orthodox polycrystalline graphites irradiated at temperatures below about 300°C the dose

dependence of Young's modulus change is very complex, an initial large rise is followed by a fall, then a second substantial rise followed by another fall, eventually reaching zero as the graphite disintegrates. For irradiation temperatures above 300°C an initial rise is followed by a constant value for a period, then a substantial rise and again a decrease to zero. Increasing irradiation temperature diminishes the dose at which the changes occur, except for the initial rise which decreases in magnitude with increasing irradiation temperature.

There are two distinct mechanisms involved in these changes, firstly due to changes in the elastic constants of the graphite crystals and secondly due to changes in the bulk structure of the graphite. Furthermore, there are two distinct mechanisms for changes in the elastic constants of the crystals. The first of these, which is responsible for the initial large rise in Young's modulus, is due to the pinning of mobile dislocations in the crystals, and this effect soon saturates. The second, which is responsible for the fall in modulus during the second irradiation phase, is caused by the changes in crystal modulus which result from the large changes in the c-axis lattice spacing which are particularly significant below 300°C. The effects of structural changes are also twofold. Differential straining of the crystal changes the pore structure in a way which at first "tightens" the graphite structure by reducing the average shear stress on the crystals (ie the modulus increases). However, at large crystal strains new porosity is generated which reduces the elastic moduli, eventually to zero, when the graphite disintegrates.

Finally, it is necessary to take into account the reduction in Young's modulus which results from the increase in porosity due to radiolytic oxidation. This effect is dependent upon weight loss and graphite type. The combined effect of fast neutron irradiation and radiolytic oxidation is the product of the factorial changes due to each effect:

$$\frac{E}{E_o} = \left(\frac{E}{E_o}\right)_i \cdot \left(\frac{E}{E_o}\right)_{ox} \qquad (14)$$

where:

$\frac{E}{E_o}$ = Factorial change in dynamic Young's modulus due to the combined effect of fast neutron irradiation and radiolytic oxidation.

$\left(\frac{E}{E_o}\right)_i$ = Factorial change in dynamic Young's modulus due to fast neutron irradiation.

$\left(\frac{E}{E_o}\right)_{ox}$ = Factorial change in dynamic Young's modulus due to radiolytic oxidation.

7.1 Data and Methodology - PGA Young's Modulus

The factorial change in Young's modulus due to irradiation above may be determined from Figs 2.22 and 2.23 which give the fractional change (E/E_o-1) as a function of equivalent DIDO nickel dose for DIDO equivalent temperatures ranging from 150 to 650°C. The data are respectively for the parallel and perpendicular directions to extrusion, from which the various effects described in Section 7 above may be observed. DIDO equivalent temperatures should be determined using an activation energy of 1.2eV.

Data covering Young's modulus changes due to radiolytic oxidation are shown in Fig 2.24, from which use of the following relationship for evaluating the factorial change as a function of weight loss is recommended for PGA graphite:

$$\left(\frac{E}{E_o}\right)_{ox} = e^{-4.8x} \qquad (15)$$

where x is the fractional weight loss.

The combined effect of these two changes may be determined using equation 14.

7.2 Data and Methodology - Gilsocarbon Young's Modulus

The higher irradiation doses and temperatures in AGRs give rise to a modified treatment of the factorial change due to fast neutron irradiation. This becomes two terms, firstly the pinning term which rapidly saturates at low dose and then shows no further change with dose, and secondly the structure term which first rises with dose and later starts to fall at the onset of turnaround. For AGRs, therefore, equation 149 is usually written as:

where:

$$\frac{E}{E_o} = P.S.W \qquad (16)$$

P = Saturated pinning term to account for pinning of mobile dislocations.

S = Structure term to allow for changes in the graphite structure due to irradiation damage.

W = Weight loss term.

$$ie \quad \frac{E}{E_o} = \left(\frac{E}{E_o}\right)_{pinning} \left(\frac{E}{E_o}\right)_{structure} \left(\frac{E}{E_o}\right)_{ox} \tag{17}$$

The pinning term is a function of DIDO equivalent temperature only, and may be determined from Fig 2.25 using an activation energy of 1.2eV.

The structure term is a function of both dose and DIDO equivalent temperature, and may be obtained from Fig 2.26 using an activation energy of 3.0 eV.

The weight loss term for Gilsocarbon graphite is also different from that applicable to PGA, and may be obtained from the relationship:

$$\left(\frac{E}{E_o}\right)_{ox} = e^{-3.4x} \tag{18}$$

where x is the fractional weight loss.

8. Static Strength

The strength criteria against which graphite failure under stress should be assessed depends upon the particular loading conditions to which the material is subject. Like all brittle materials, graphite has different failure apparent stresses depending on the type of loading and the component geometry. It is stronger in compression than bend, and stronger in bend than tension. For moderator bricks and keys, the stress distribution is a complex one to which neither the ultimate tensile strength nor bend strength may be used to calculate failure under tensile loading. In these cases the apparent stress at the point of fracture initiation must be determined by finite element modelling using the results of destructive tests on appropriately loaded moderator bricks and keys or slices cut from these components. The strength of a moderator brick or key which has suffered radiation damage and radiolytic oxidation may then be evaluated by adjusting this apparent failure stress by the appropriate factorial changes in graphite strength derived from experimental data on these effects.

Fast neutron irradiation produces substantial increases in the strength of graphite except at very high doses where the fall in the elastic moduli is accompanied by a loss of strength. The mechanism for the strength changes is the same as that causing changes to Young's modulus, being the result of within-crystal effects at low doses and structural changes at high doses.

In a brittle material such as graphite a crack growth mechanism of failure would be expected to operate, and a Griffith-type relationship between strength σ, modulus E, work of fracture g, and inherent flaw size c, viz:

$$\sigma^2 \propto g\frac{E}{c} \tag{19}$$

implies that changes within the crystal lattice without changes in the inherent crack population should lead to a strength change proportional to the square root of the modulus change, ie:

$$\left(\frac{\sigma}{\sigma_o}\right)_i = \left(\frac{E}{E_o}\right)_i^{1/2} \tag{20}$$

where:

$\left(\frac{\sigma}{\sigma_o}\right)_i$ = Factorial change in strength due to fast neutron irradiation

$\left(\frac{E}{E_o}\right)_i$ = Factorial change in Young's modulus due to fast neutron irradiation

However, irradiation-induced structural changes external to the crystal may influence the work of fracture or the effective flaw size, as well as the average crack/pore spectrum sampled by the modulus, and so equation 20 cannot be expected to be obeyed exactly. Nevertheless, the relationship of Equation 20 has been shown to represent the data reasonably well up to the point of turnaround where the structural changes give rise to a fall in Young's modulus beyond which the fall in strength is more severe.

Radiolytic oxidation also causes changes in strength, and the overall strength change is given by:

$$\frac{\sigma}{\sigma_o} = \left(\frac{\sigma}{\sigma_o}\right)_i \cdot \left(\frac{\sigma}{\sigma_o}\right)_{ox} \tag{21}$$

where

$\left(\frac{\sigma}{\sigma_o}\right)_{ox}$ = Factorial change in strength due to radiolytic oxidation.

8.1 Data and Methodology - PGA Strength

Determination of the factorial change in strength due to fast neutron irradiation should make use of equation 20, with factorial changes in Young's modulus evaluated by the method described in Section 7.1. An activation energy of 1.2eV should again be used to determine

DIDO equivalent temperatures in Figs 2.22 and 2.23 which give values of (E/E_o-1) as a function of dose.

Determination of the factorial change in strength due to radiolytic oxidation should make use of the following relationship derived from the data of Fig 2.27:

$$\left(\frac{\sigma}{\sigma_o}\right)_{ox} = e^{-5.2x} \qquad (22)$$

where x is the fractional weight loss.

The combined effect of these two changes may then be determined using equation 21.

8.2 Data and Methodology - Gilsocarbon Strength

As was the case for Young's modulus, the higher doses and temperatures in AGRs give rise to a modified treatment, and for such applications equation 21 is usually written:

$$\frac{\sigma}{\sigma_o} = (P.S^*)^{1/2} W \qquad (23)$$

where:

P = Saturated pinning term to account for pinning of mobile dislocations.

S* = Modified structure term to allow for structural changes due to irradiation damage.

W = Weight loss term = $\left(\frac{\sigma}{\sigma_o}\right)_{ox}$

$$ie \quad \frac{\sigma}{\sigma_o} = \left[\left(\frac{E}{E_o}\right)_{pinning} \cdot \left(\frac{E}{E_o}\right)_{mod\_struct}\right]^{1/2} \left(\frac{\sigma}{\sigma_o}\right)_{ox} \qquad (24)$$

The pinning term is the value of (E/E_o) read from Fig 2.25 using an activation energy of 1.2eV.

The modified structure term is given in Fig 2.28, for which an activation energy of 3.0eV is appropriate for calculating values of EDT. These curves have been calculated assuming that strength is proportional to the square root of the modulus change for doses up to the maximum modulus change. Above this dose, strength changes are assumed to vary linearly with modulus change. The modified structure term has thus been evaluated as:

$$S^* = S \qquad \gamma < \gamma_{max}$$

$$S^* = \frac{S^2}{S_{max}} \qquad \gamma \geq \gamma_{max}$$

where S is the structure term shown in Fig 2.26.

The weight loss term for Gilsocarbon strength changes may be obtained from the relationship:

$$\left(\frac{\sigma}{\sigma_o}\right)_{ox} = e^{-3.7x} \qquad (25)$$

where x is the fractional weight loss.

9. Impact Strength

UKAEA studies of unirradiated graphite specimens subjected to repeated impacts carried out on a variety of graphite types including PGA have shown that there is a one to one correlation between the dynamic stress at failure in a single impact and the static 3-point bend strength, Fig 2.29. From this work it was concluded that the impact energy to fail a rod was proportional to σ_b^2/E, Fig 2.30.

Much less work has been done on the impact behaviour of irradiated graphite. Probably the most detailed work has been carried out on AGR fuel sleeves, but this work is very specific in being used to support safety cases for on-load refuelling.

Although no firm rules exist for determining the impact strength of irradiated graphite, it is generally accepted that the above relationship between impact energy, strength and modulus may be used as a means of estimating the factorial change in impact strength due to fast neutron irradiation, $(U/U_o)_i$. Thus:

$$(U/U_o)_i = \frac{(\sigma/\sigma_o)_i^2}{(E/E_o)_i} \quad (26)$$

Substituting the relationship between strength and modulus changes due to fast neutron irradiation given in equation 20 gives:

$$(U/U_o)_i = \frac{\left[(E/E_o)_i^{1/2}\right]^2}{(E/E_o)_i} = 1$$

This implies that the impact strength is unchanged by irradiation up to the point of turnaround (see Section 8). However this approach is simplistic since it assumes that the stress/strain behaviour is linear before and after irradiation. In reality, unirradiated graphite exhibits non-linear behaviour and significant hysteresis whereas irradiated graphite shows more linear behaviour and less hysteresis. These factors would be expected to affect the energy absorption capacity of the material but are difficult to quantify.

It would be expected that radiolytic oxidation would reduce the impact strength of graphite since both strength and modulus are reduced. UKAEA have studied the impact strength of various sleeve graphites, from which is was concluded that radiolytic oxidation up to 19% weight loss did not have any untoward effect on impact resistance over and above that indicated by the changes in static strength and Young's modulus. Thus the factorial change in impact strength due to radiolytic oxidation, $(U/U_o)_{ox}$, may be obtained from the equation:

$$(U/U_o)_{ox} = \frac{(\sigma/\sigma_o)_{ox}^2}{(E/E_o)_{ox}} \quad (27)$$

9.1 Data and Methodology - PGA Impact Strength

PGA graphite is not irradiated beyond the point of turnaround and so for PGA:

$$(U/U_o)_i = 1 \quad (28)$$

ie there is no change in PGA impact strength due to irradiation alone.

Equation 27 may be used to estimate the factorial change in impact strength due to radiolytic oxidation by substituting the relationships for static strength, and Young's modulus changes from equations 22 and 15 respectively. Thus for PGA graphite:

$$(U/U_o)_{ox} = \frac{(e^{-5.2x})^2}{e^{-4.8x}} = e^{-5.6x} \quad (29)$$

9.2 Data and Methodology - Gilsocarbon Impact Strength

Up to the point of turnaround Gilsocarbon static strength change due to fast neutron irradiation is directly proportional to the square root of the modulus change, as given by equation 20. For this dose range, therefore, there is no change in Gilsocarbon impact strength due to irradiation alone since equation 28 will apply.

Beyond turnaround, Gilsocarbon strength is assumed to vary linearly with modulus change. Since Young's modulus is seen to fall beyond turnaround, this implies there is a corresponding fall in strength. From equation 26, it will be clear that a reduction in both strength and modulus beyond turnaround at the same rate will result in a fall in Gilsocarbon impact strength. This fall in both strength and modulus beyond turnaround is given by $E_t/E_{max.}$, where E_t is the Young's modulus value beyond turnaround and E_{max} is the maximum value of modulus reached at the point of turnaround where the dose is γ_{max}. Thus for Gilsocarbon graphite:

$$(U/U_o)_i = 1 \qquad \gamma < \gamma_{max} \tag{30}$$

$$(U/U_o)_i = \frac{(Et/E_{max})^2}{Et/E_{max}} = Et/E_{max} \qquad \gamma \geq \gamma_{max} \tag{31}$$

where Et/E_{max} is taken from Fig 2.26 using an activation energy of 3.0 eV.

For Gilsocarbon graphite, the factorial change in impact strength due to radiolytic oxidation may be obtained from equation 27 by substituting the relationship given by equations 25 and 18.

$$(U/U_o)_{ox} = \frac{(e^{-3.7x})^2}{e^{-3.4x}} = e^{-4.0x} \tag{32}$$

The combined effect of irradiation and radiolytic oxidation may be obtained by assuming that the two effects are multiplicative, ie that:

$$U/U_o = (U/U_o)_i \, (U/U_o)_{ax} \quad (33)$$

10. Irradiation Creep

When graphite is subjected to an applied stress in the presence of fast neutron irradiation it exhibits creep strain. This behaviour is extremely important since without irradiation creep the stresses in moderator bricks and keys would become unacceptably high at relatively low doses. Thermal creep is negligible at all temperatures of practical interest.

Experiments at constant stress showed that the creep strain during irradiation of graphite under stress is separated into primary and secondary contributions:

$$\epsilon_c = \epsilon_p + \epsilon_s \quad (34)$$

where

ϵ_c = total creep strain

ϵ_p = primary creep strain (recoverable)

ϵ_s = secondary creep strain

These experiments have shown that when structural changes within the graphite are not significant, the total creep strain under a constant externally applied stress σ is given by:

$$\epsilon_c = \frac{\sigma}{{}_sE_o}(1 - e^{-A\gamma}) + \frac{\sigma}{{}_sE_o} \cdot 0.23\gamma \quad (35)$$

where:

γ = Equivalent DIDO nickel dose in units of 10^{20} n/cm^2

${}_sE_o$ = Initial (unirradiated) Young's modulus obtained in a static test up to stress σ.

Thus both primary and secondary creep terms are linear with applied stress and inversely proportional to the initial Young's modulus. This applies for different graphites, for different directions within the same graphite, or for density variations in the same material. The creep strain may be uniquely expressed in elastic strain units (esu);

$$\epsilon_c\ (esu) \;=\; (1 - e^{-4\gamma}) + 0.23\gamma \qquad (36)$$

where:

$$1\ \ esu \;=\; \frac{\sigma}{{}_sE_0}$$

Data covering several types of graphite are shown in Fig 2.31. The upper two plots demonstrate the linearity of creep strain with dose and the fit with equation 35. The lower plots demonstrate that despite major differences in properties, all graphites conform to the single relationship of equation 36 when creep strain is expressed in elastic strain units.

The experimental data indicate that creep is substantially independent of temperature in the range 300 to 600°C. Below 300°C, the data are not sufficiently well established to doses at which structural effects may influence creep rate.

Under constant stress, the secondary creep term in equation 35 is modified to allow for structural changes in Young's modulus at high doses and for radiolytic weight loss by substituting for ${}_sE_o$ the effective modulus:

$$E_{eff} \;=\; {}_sE_o \,.\, S.W \qquad (37)$$

where

$$S \;=\; \left(\frac{E}{E_o}\right)_{ructure}$$

$$W \;=\; \left(\frac{E}{E_o}\right)_{ox}$$

Hence, the secondary creep strain between dose limits γ_1 and γ_1 may be written

$$\epsilon_s \;=\; \frac{0.23\sigma}{{}_sE_o} \int_{\gamma_1}^{\gamma_2} \frac{1}{S.W}\, d\gamma \qquad (38)$$

Which may be further modified to allow for variable stress:

$$\epsilon_s = \frac{0.23}{{}_sE_o} \int_{\gamma_1}^{\gamma_2} \frac{\sigma}{S.W} d\gamma \qquad (39)$$

The concept of an effective modulus should also be applied in the consideration of primary creep and its recovery.

10.1 Data and Methodology - PGA Irradiation Creep

The irradiation creep data at temperatures > 300°C are reasonably well defined and indicate the use of a structure term, S, of 1.0. The complex modulus changes < 300°C preclude definition of a structure factor in this temperature range.

The weight loss term, W, is represented by the relationship given in Section 7.1, equation 15, ie:

$$W = \left(\frac{E}{E_o}\right)_{ox} = e^{-4.8x}$$

10.2 Data and Methodology - Gilsocarbon Irradiation Creep

The structure term, S, recommended for Gilsocarbon may be obtained from Fig 2.26 using an activation energy of 3.0eV.

The weight loss term, W, is given by equation 18 in Section 7.2, ie:

$$W = \left(\frac{E}{E_o}\right)_{ox} = e^{-3.4x}$$

11.0 Activation Energy Values

Table 2.2 gives a convenient summary of activation energy values recommended in the Data and Methodology sections of this lecture for use in calculating DIDO equivalent temperatures when determining the various property changes of PGA and Gilsocarbon graphites.

References

1. Birch M and Brocklehurst J E. A review of the effects of irradiation on the physical and mechanical properties of Pile Grade "A" graphite. ND-R-1236(S), August 1986.

2. Brocklehurst J E. Irradiation damage in CAGR moderator graphite. ND-R-1117(S), July 1984 and Addendums.

Attack Rate Parameter for RPV Model gm/gm per hr per mW/gm x 10**8							
	Carbon Monoxide						
Methane	2500	5000	75000	10000	15000	20000	25000
0.0	0.822	0.641	0.505	0.411	0.312	0.270	0.247
25.0	0.656	0.548	0.442	0.366	0.286	0.253	0.235
50.0	0.526	0.470	0.388	0.327	0.263	0.237	0.224
75.0	0.423	0.404	0.341	0.293	0.241	0.222	0.214
100.0	0.343	0.348	0.301	0.262	0.222	0.209	0.204
125.0	0.280	0.301	0.267	0.236	0.205	0.196	0.194
150.0	0.230	0.262	0.237	0.213	0.190	0.185	0.186
175.0	0.192	0.228	0.211	0.193	0.176	0.174	0.178
200.0	0.161	0.200	0.189	0.175	0.164	0.164	0.170
225.0	0.137	0.177	0.170	0.160	0.152	0.155	0.163
250.0	0.118	0.157	0.153	0.146	0.142	0.147	0.156
275.0	0.104	0.140	0.139	0.134	0.133	0.140	0.150
300.0	0.092	0.126	0.127	0.124	0.125	0.132	0.144
325.0	0.083	0.114	0.116	0.114	0.117	0.126	0.138
350.0	0.076	0.104	0.107	0.106	0.111	0.120	0.133

Table 2.1 - Attack Rate Parameter as a Function of Methane and Carbon Monoxide Concentration for Gilsocarbon Graphite at 400 degrees C and 41 bar

Table 2.2 - Activation Energy Values for Calculating DIDO Equivalent Temperatures when Determining the Irradiation - Induced Property Changes of PGA and Gilsocarbon Graphites

Property Change		Activation Energy, eV	
		PGA	Gilsocarbon
Dimensional Changes		1.2	3.0
Coefficient of Thermal Expansion		1.2	3.0
Thermal Conductivity		1.2	3.0
Stored Energy		1.2	-
Young's Modulus	YM versus dose	1.2	-
	YM Saturated Pinning Term	-	1.2
	YM Structure Term	-	3.0
Static Strength	YM versus dose	1.2	-
	YM Saturated Pinning Term	-	1.2
	YM Modified Structure Term	-	3.0
Impact Strength, Et/Emax		-	3.0
Irradiation Creep, YM Structure Term		-	3.0

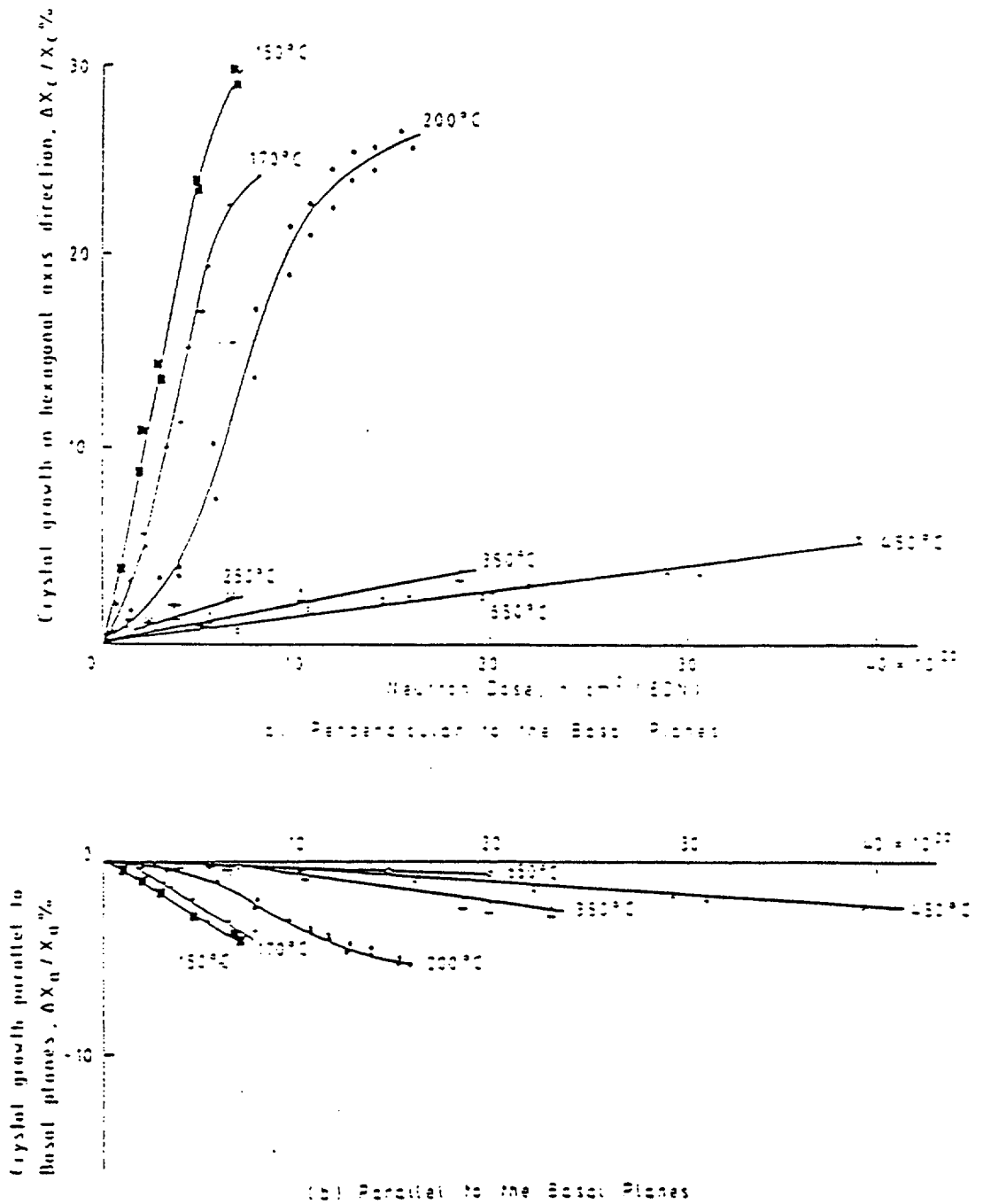

Figure 1. Dimensional changes of Pyrolytic Graphite – low temperature

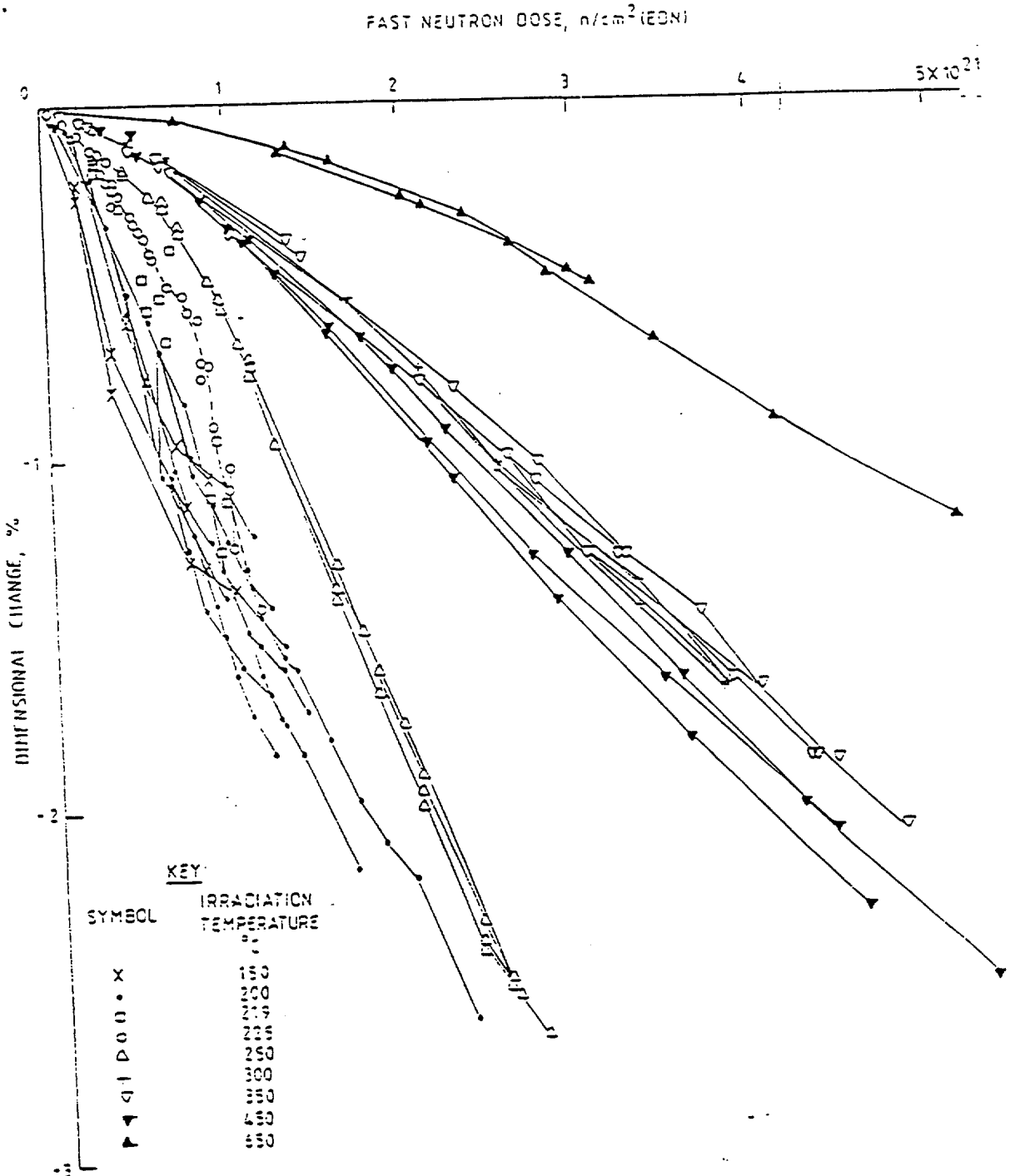

Figure 2. IRRADIATION INDUCED DIMENSIONAL CHANGES PARALLEL TO EXTRUSION: STANDARD DIDO Mk III HOLLOW FUEL ELEMENT DATA

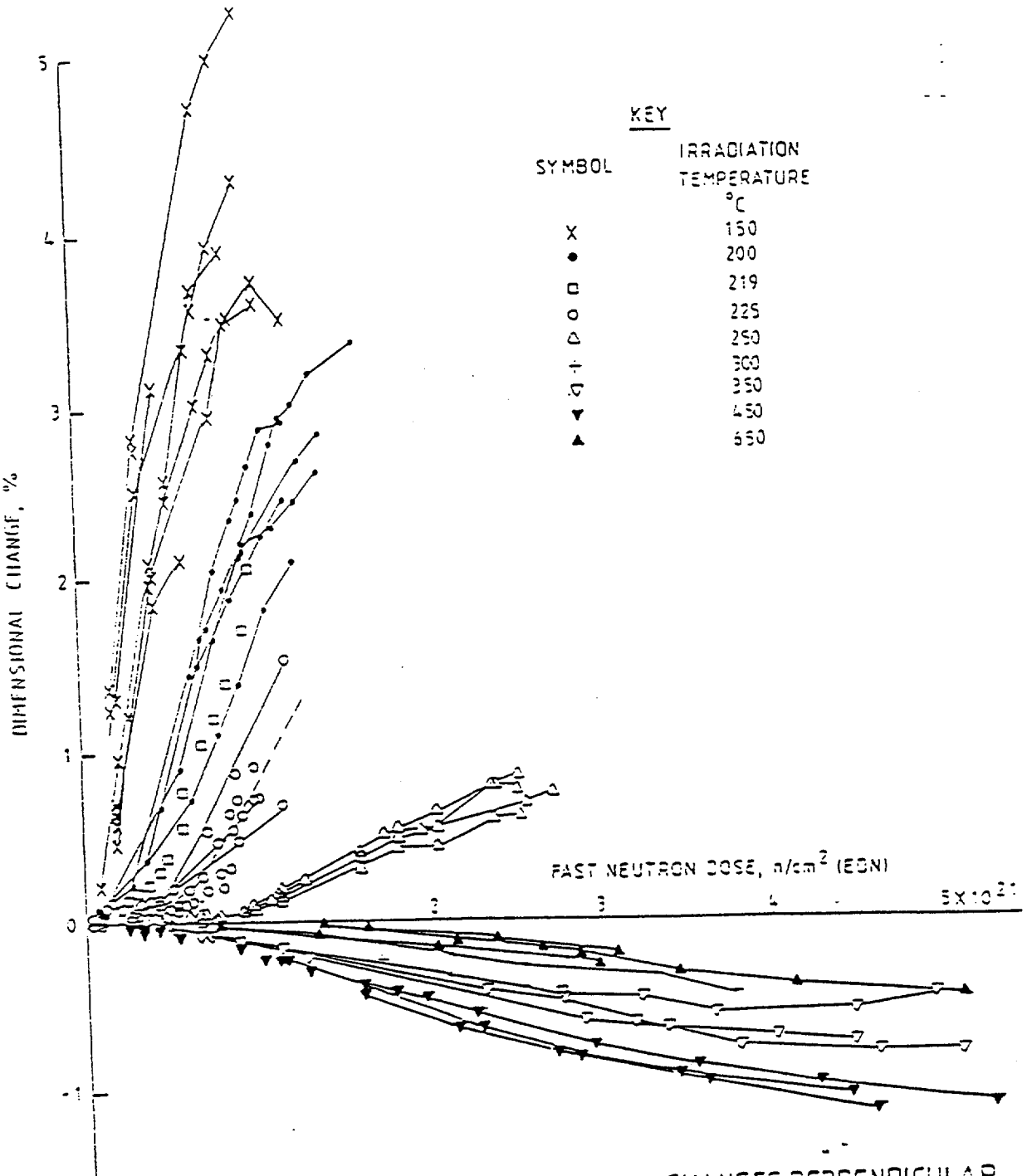

Figure 3. IRRADIATION INDUCED DIMENSIONAL CHANGES PERPENDICULAR TO EXTRUSION: STANDARD DIDO Mk III HOLLOW FUEL ELEMENT DATA

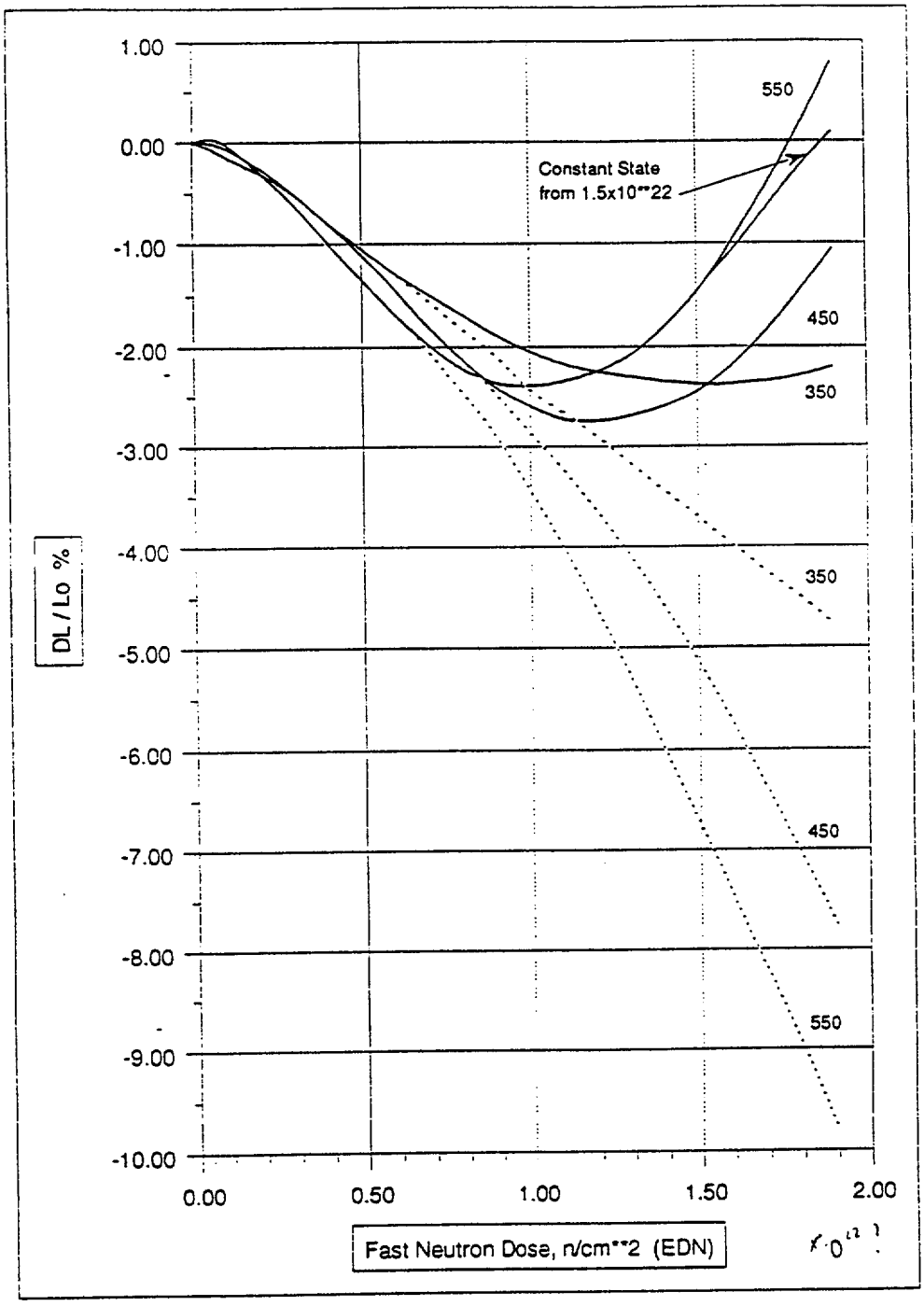

Figure 4. Dimensional Changes and a 'free' Shrinkage of CAGR Moderator Graphite at Different DIDO Equivalent Temperatures

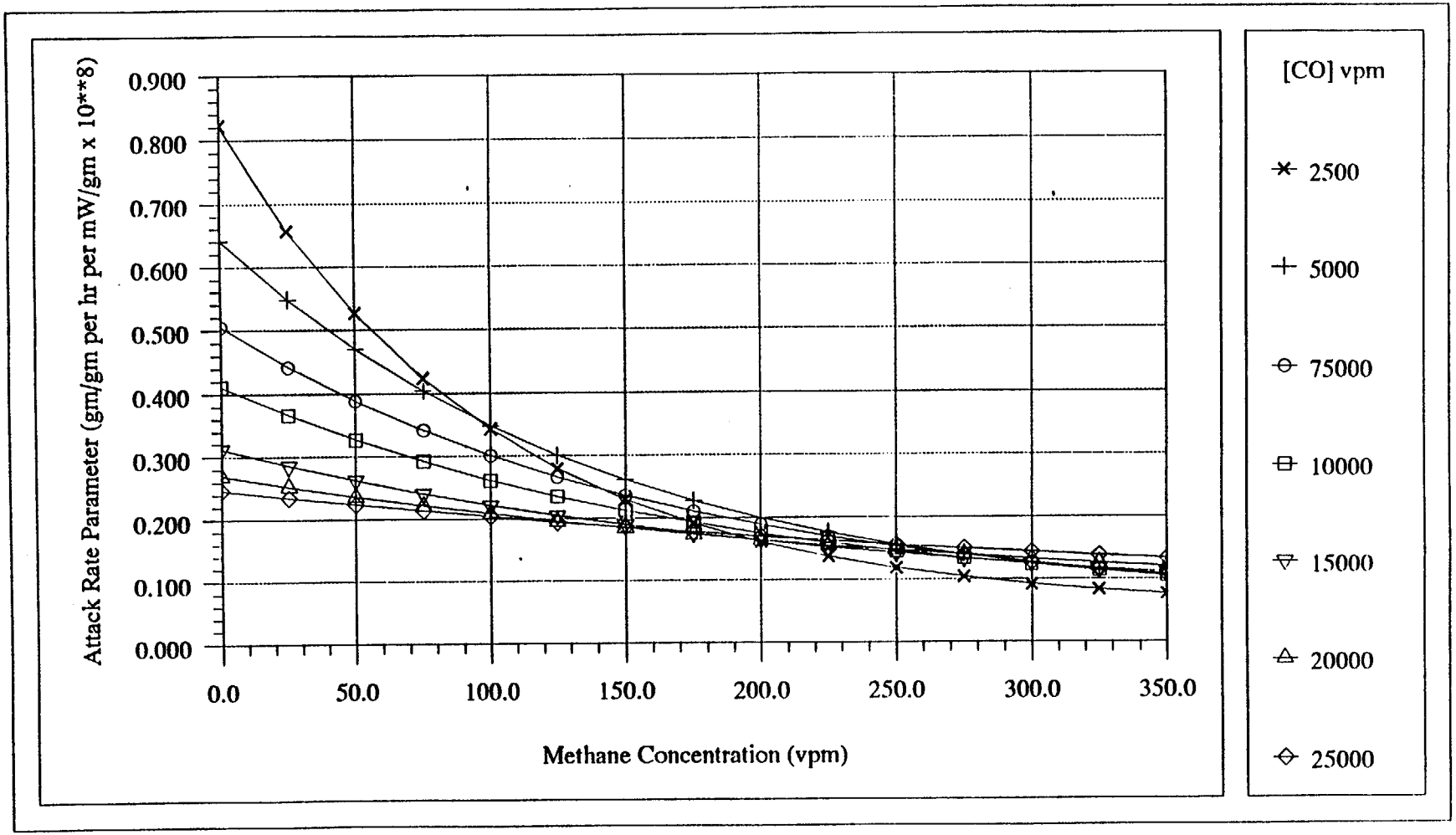

Figure 5. Attack Rate Parameter as a Function of Methane and Carbon Monoxide Concentration for Gilsocarbon Graphite at 400 degrees C and 41 bar

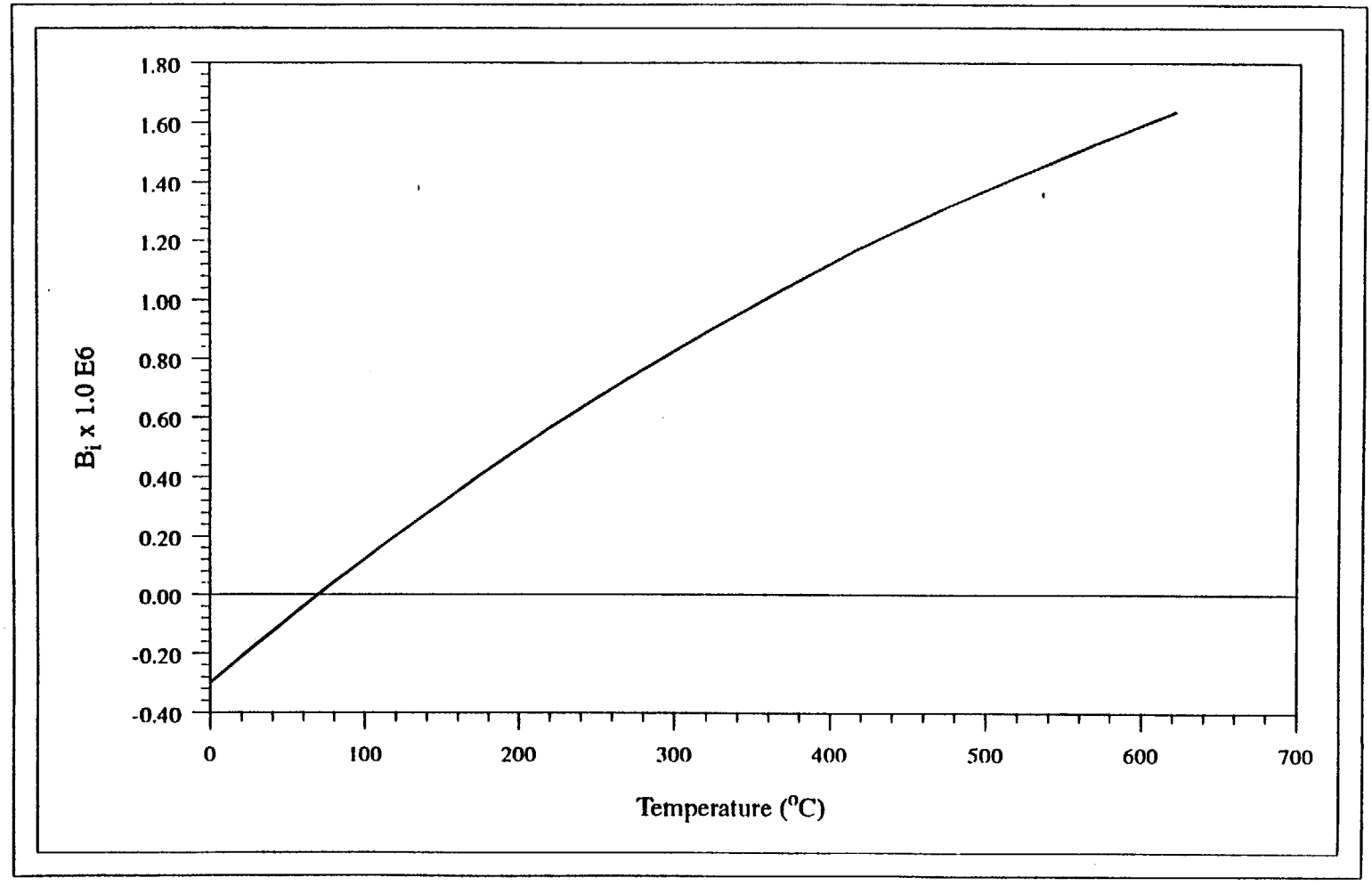

Figure 6. Parameter B_i v Temperature for Graphite

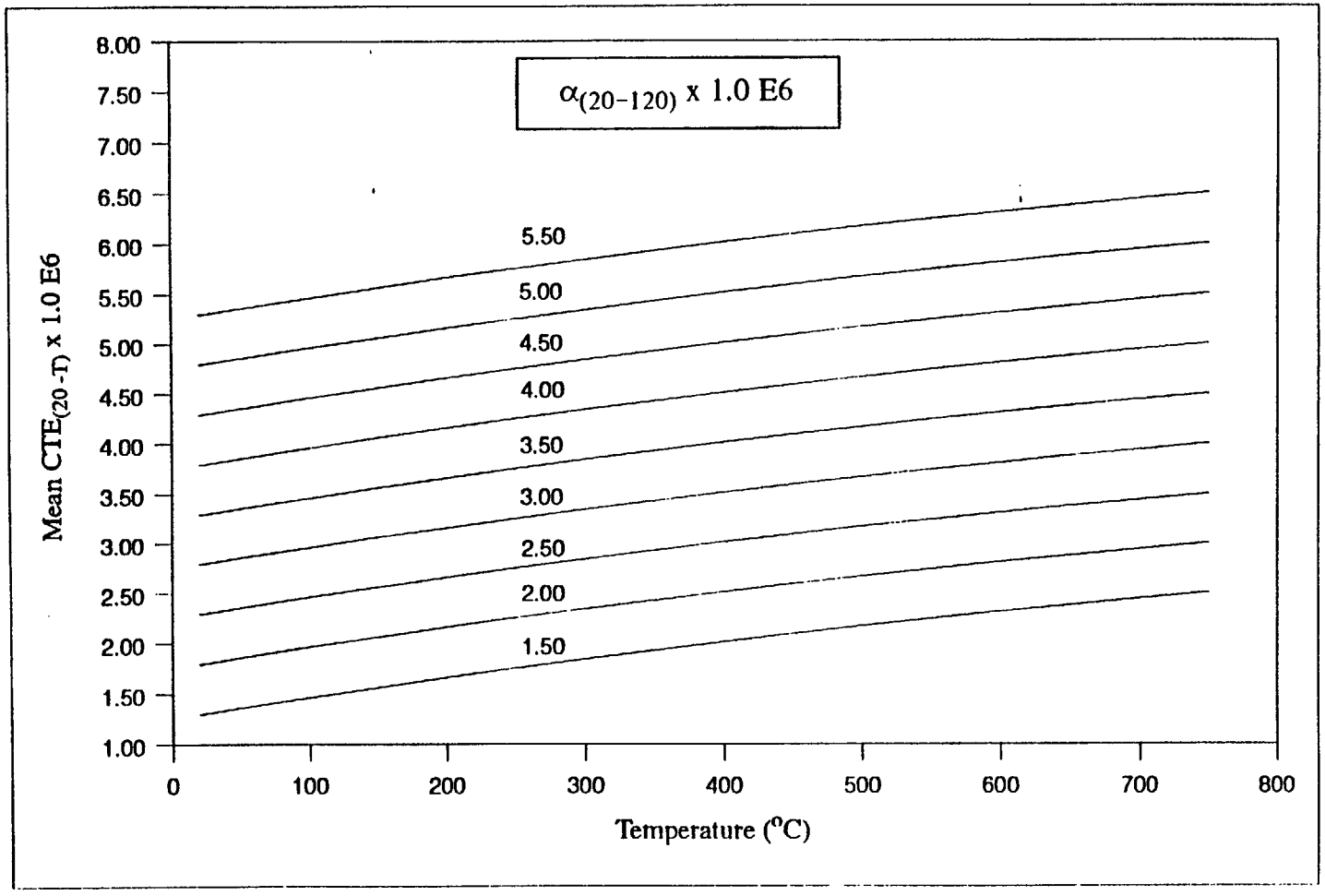

Figure 7. Mean CTE v Temperature & $\alpha_{(20\text{-}120)}$ for Gilsocarbon Graphite

Figure 8(a) & (b).

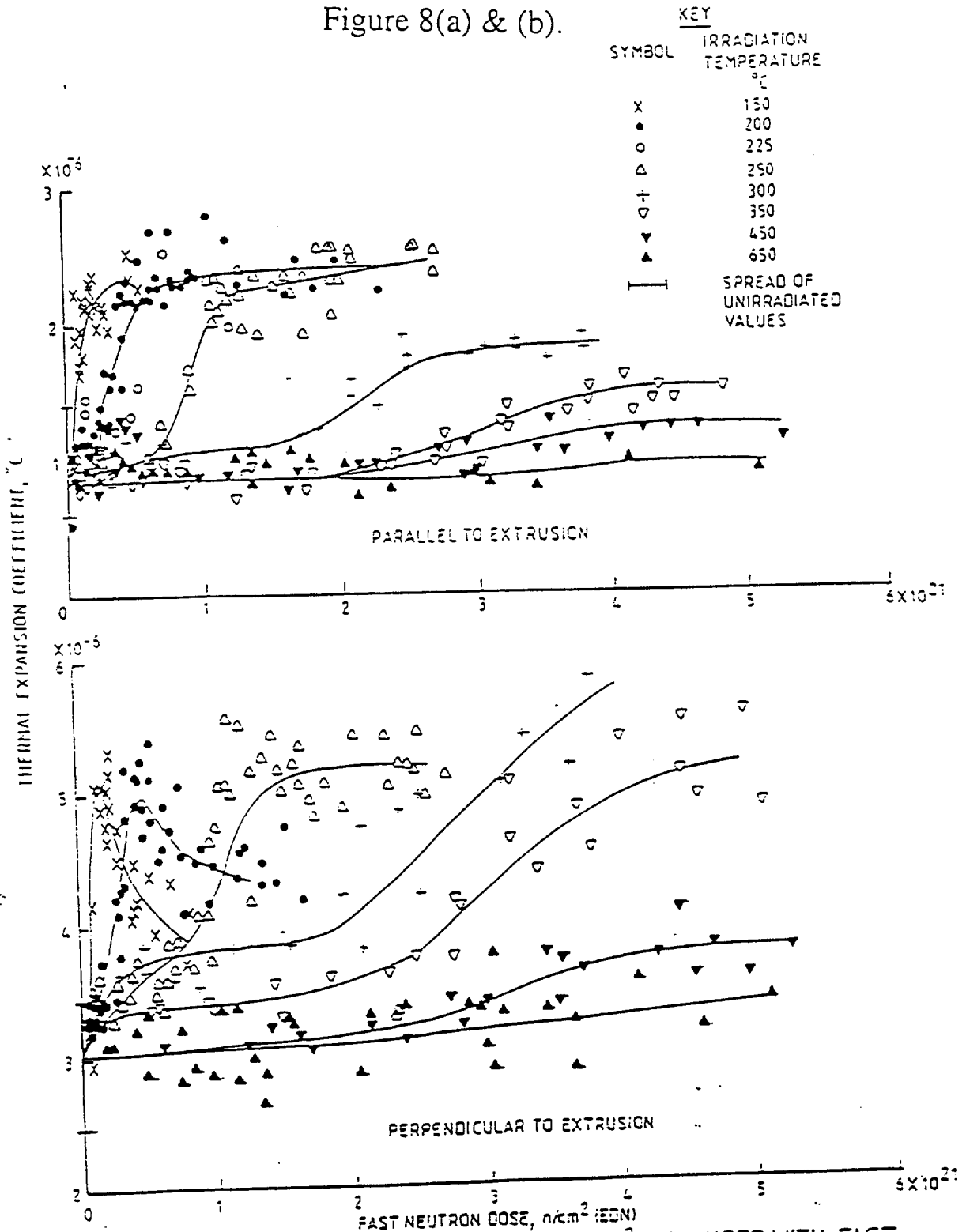

THERMAL EXPANSION COEFFICIENT (20-120°C) CHANGES WITH FAST NEUTRON DOSE: STANDARD DIDO Mk III HOLLOW FUEL ELEMENT DATA

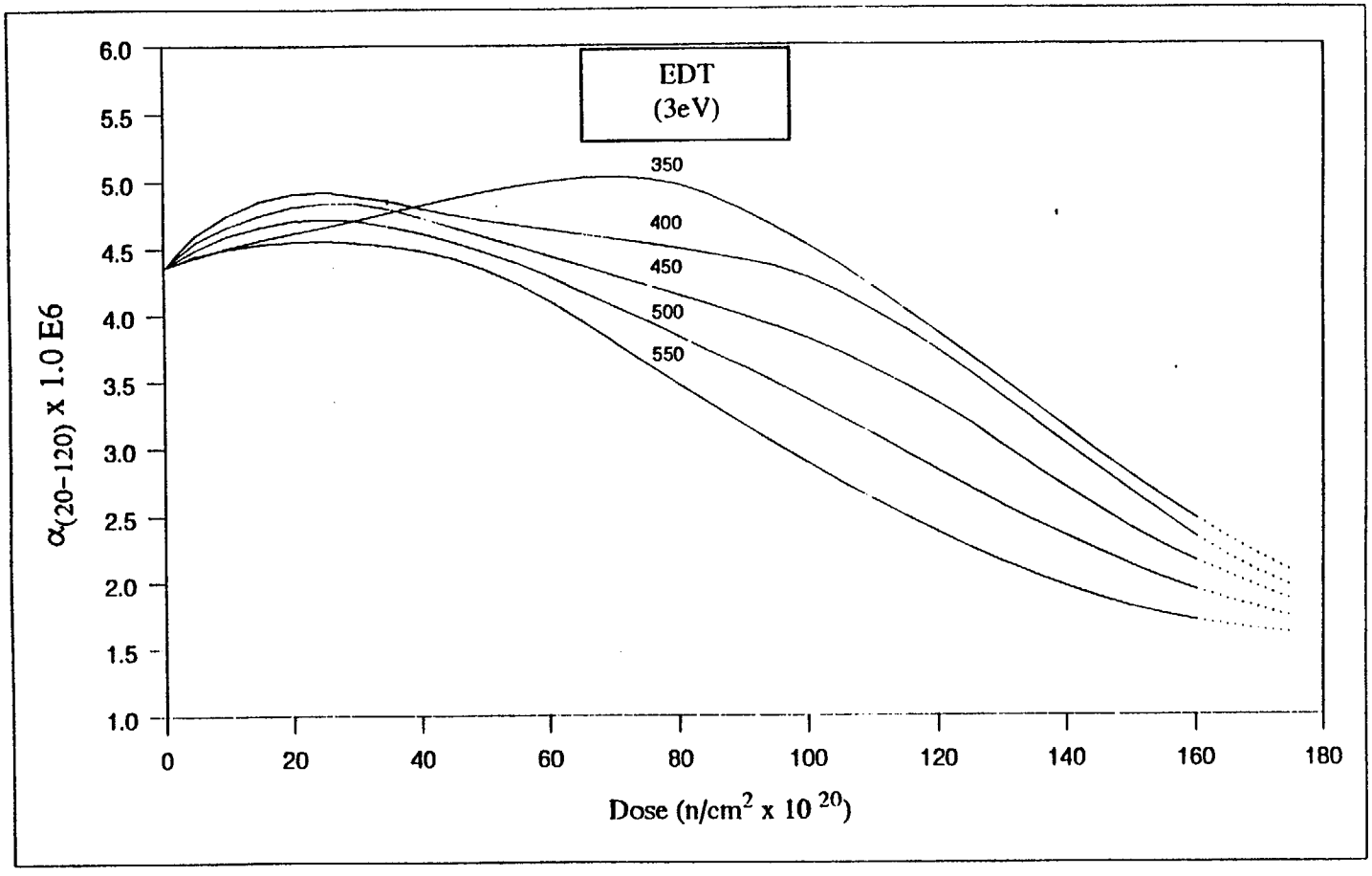

Figure 9(a). $\alpha_{(20-120)}$ v Dose & EDT for Gilsocarbon Graphite

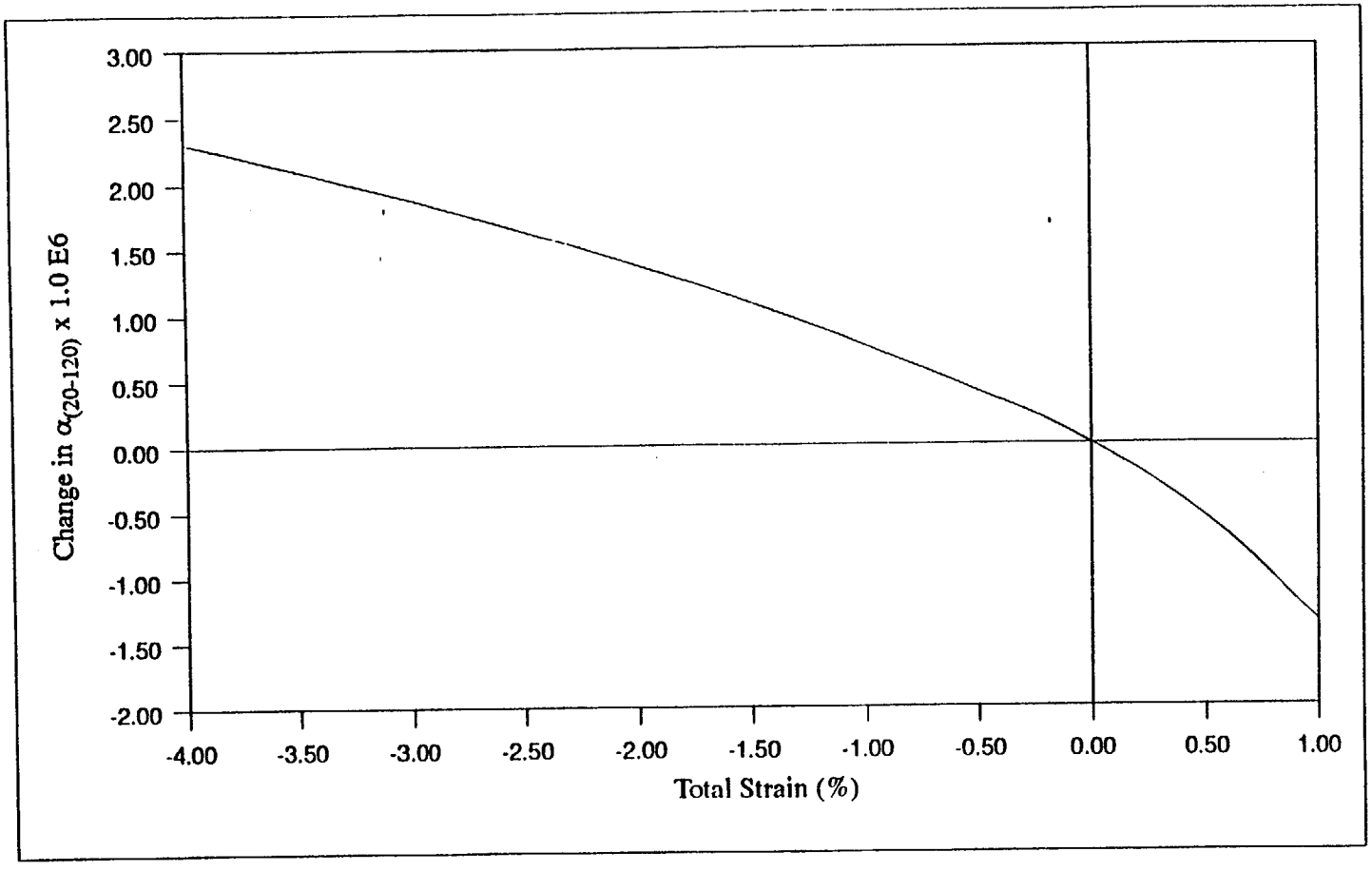

Figure 9(b). Change in $\alpha_{(20-120)}$ v Total Strain for Gilsocarbon Graphite

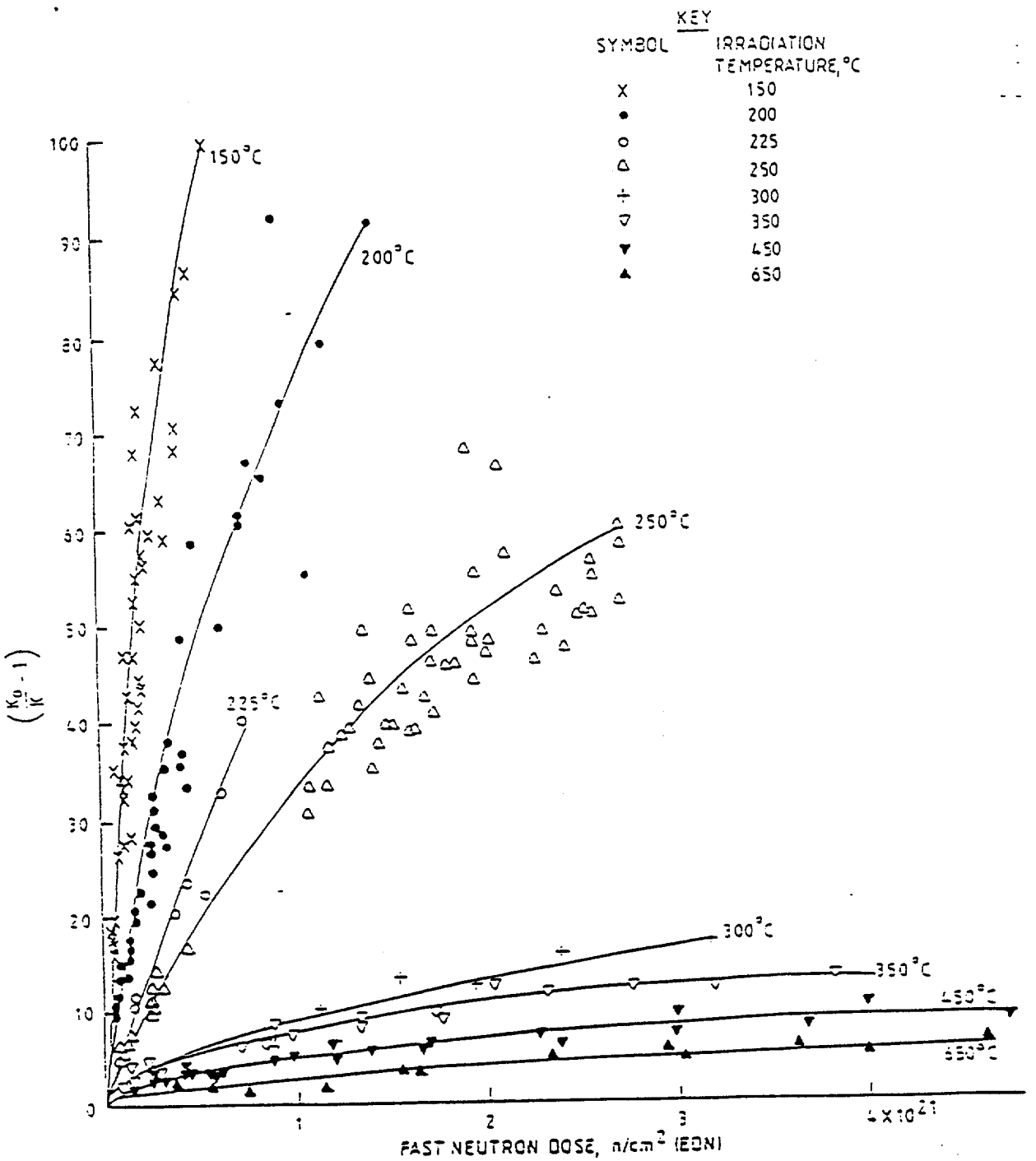

Figure 10. FRACTIONAL CHANGES IN THERMAL RESISTIVITY WITH FAST NEUTRON DOSE: STANDARD DIDO Mk III HOLLOW FUEL ELEMENT DATA

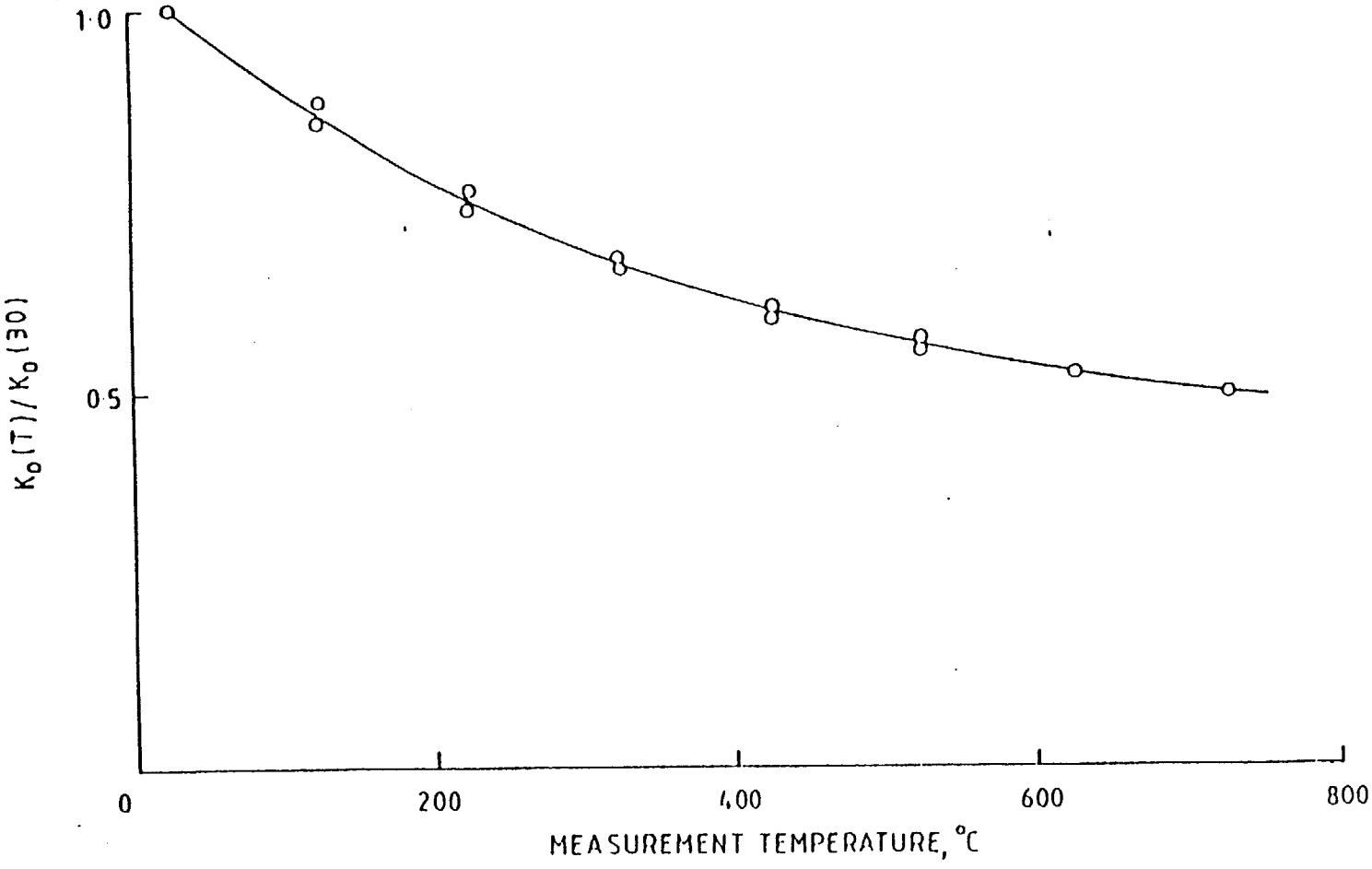

Figure 11. THERMAL CONDUCTIVITY TEMPERATURE DEPENDENCE OF UNIRRADIATED PGA GRAPHITE

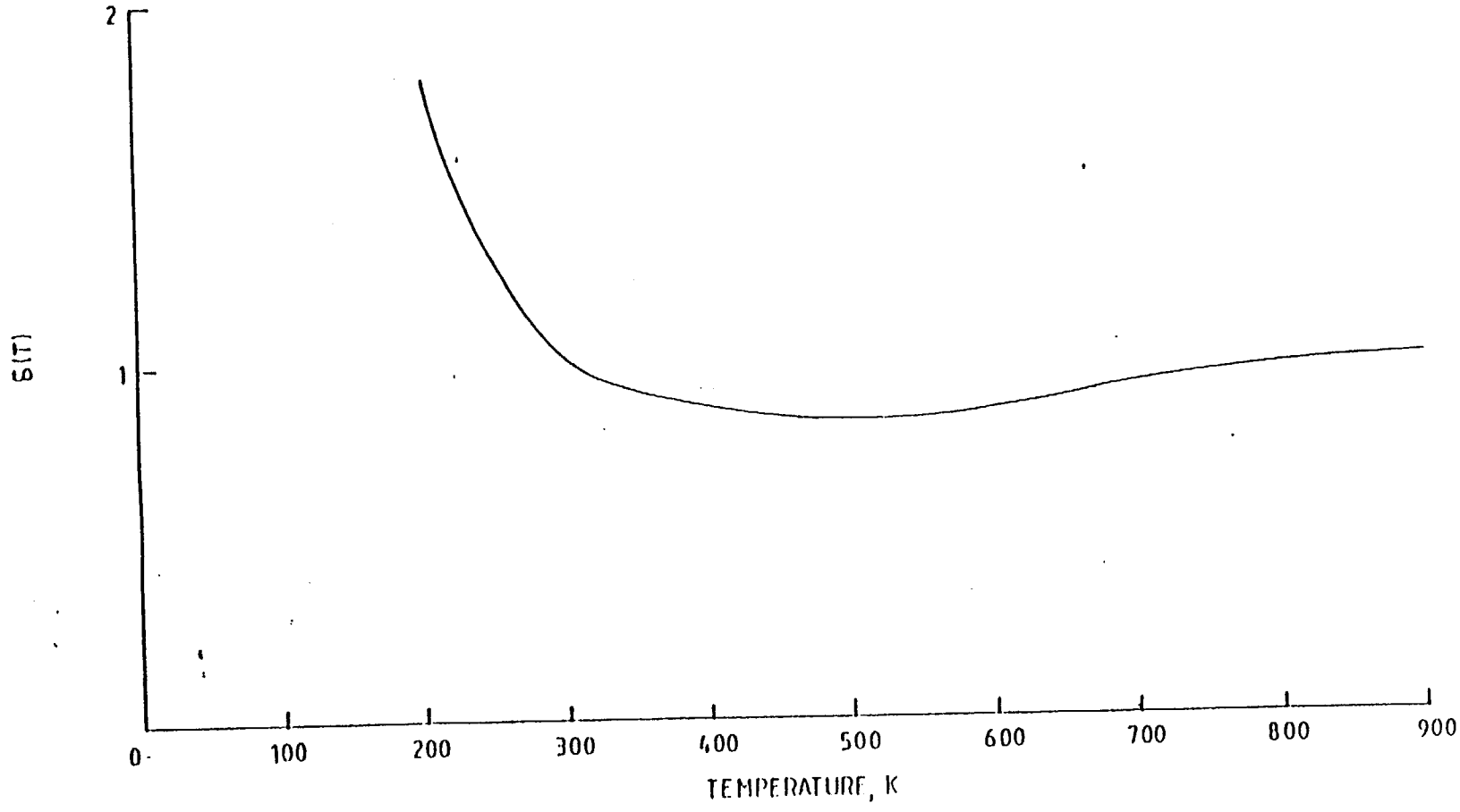

Figure 12. THERMAL RESISTANCE IN IRRADIATED GRAPHITE NORMALISED TO 300 K

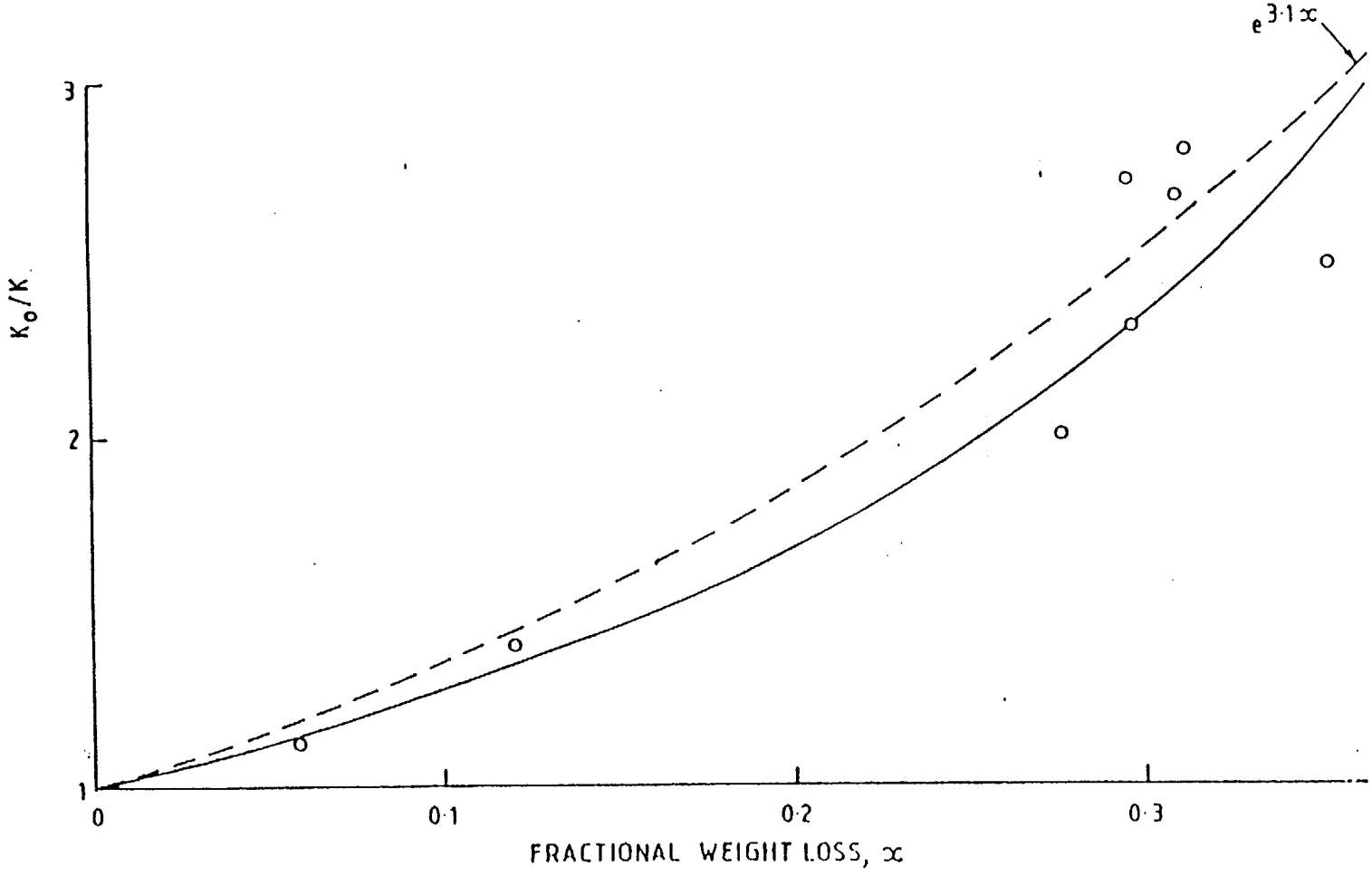

Figure 13. CHANGE IN THERMAL RESISTIVITY WITH RADIOLYTIC WEIGHT LOSS

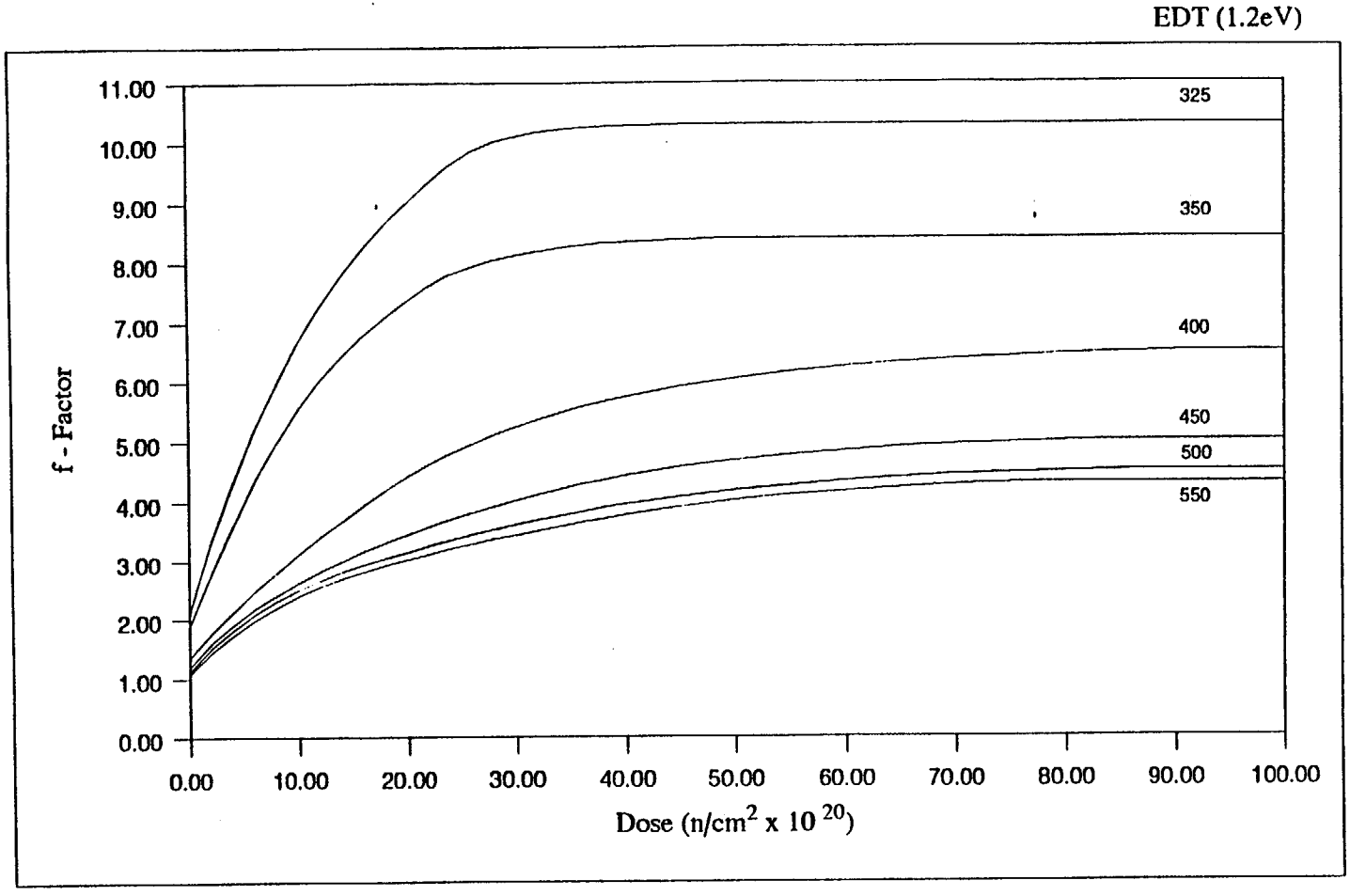

Figure 14. f-Factor v Dose & EDT for Gilsocarbon Graphite

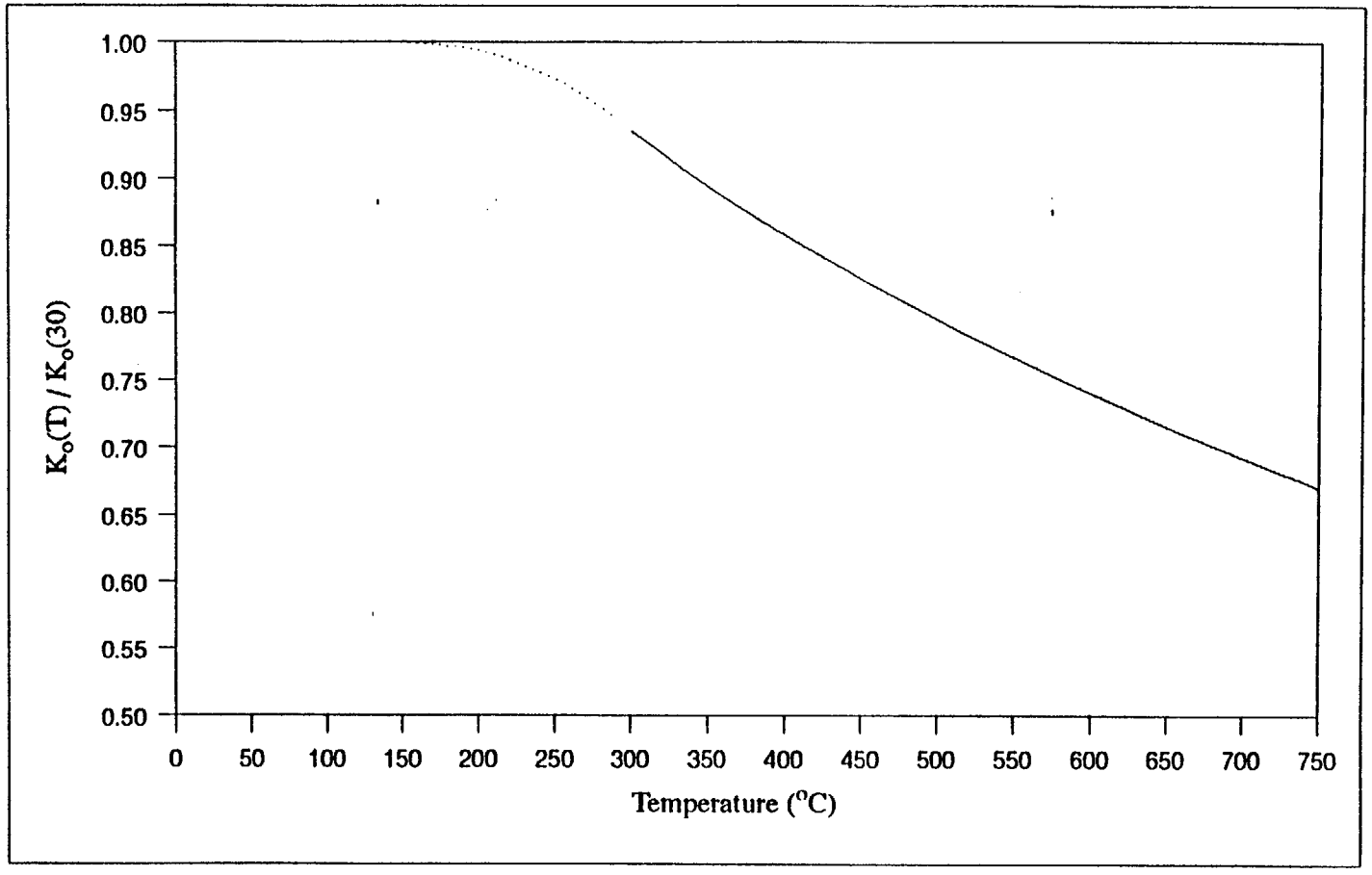

Figure 15. $K_o(T) / K_o(30)$ v Temperature, for Gilsocarbon Graphite from Heysham II / Torness Only

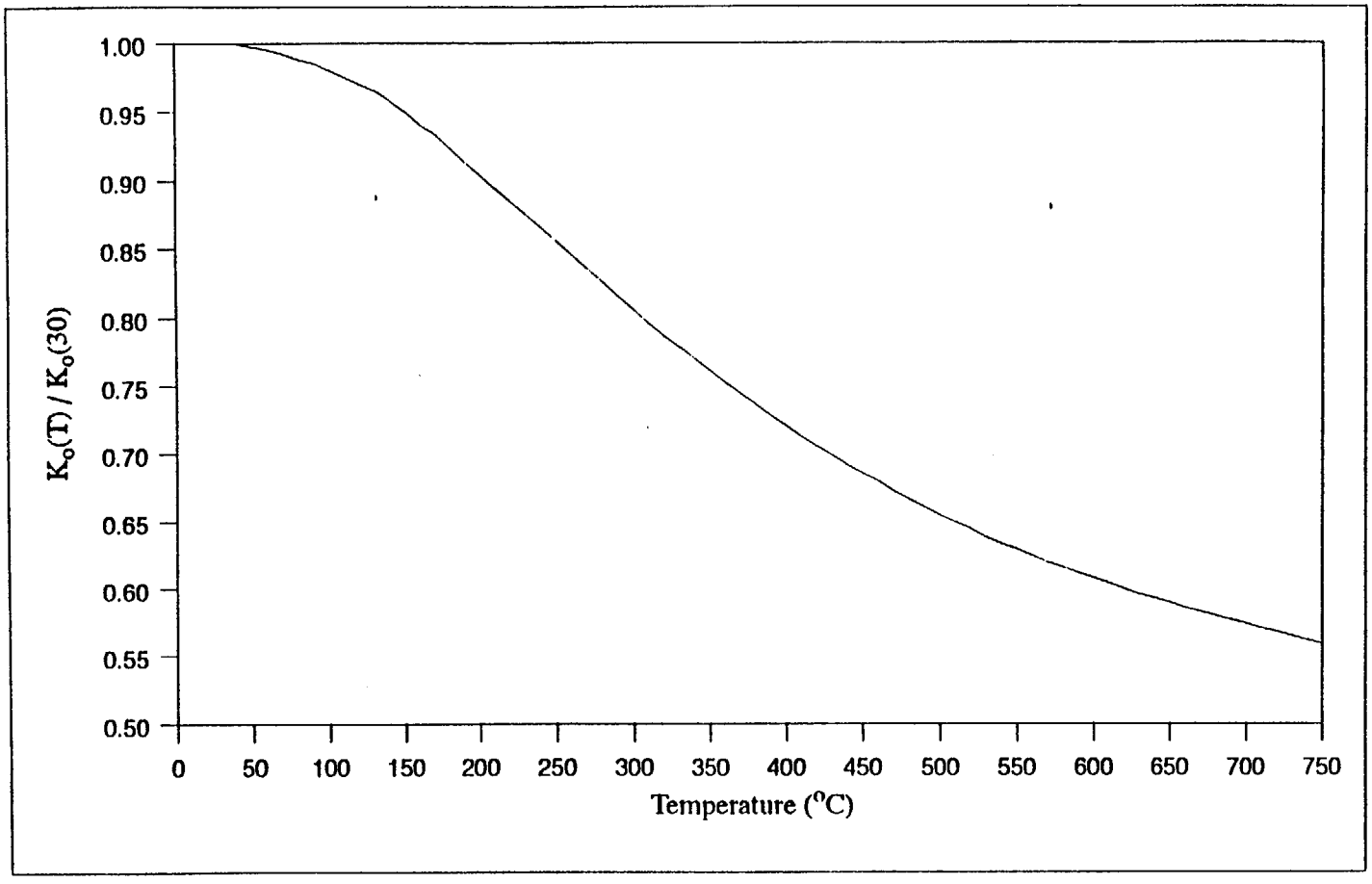

Figure 16. $K_o(T) / K_o(30)$ v Temperature, for Gilsocarbon Graphite for AGR's other than Heysham II / Torness

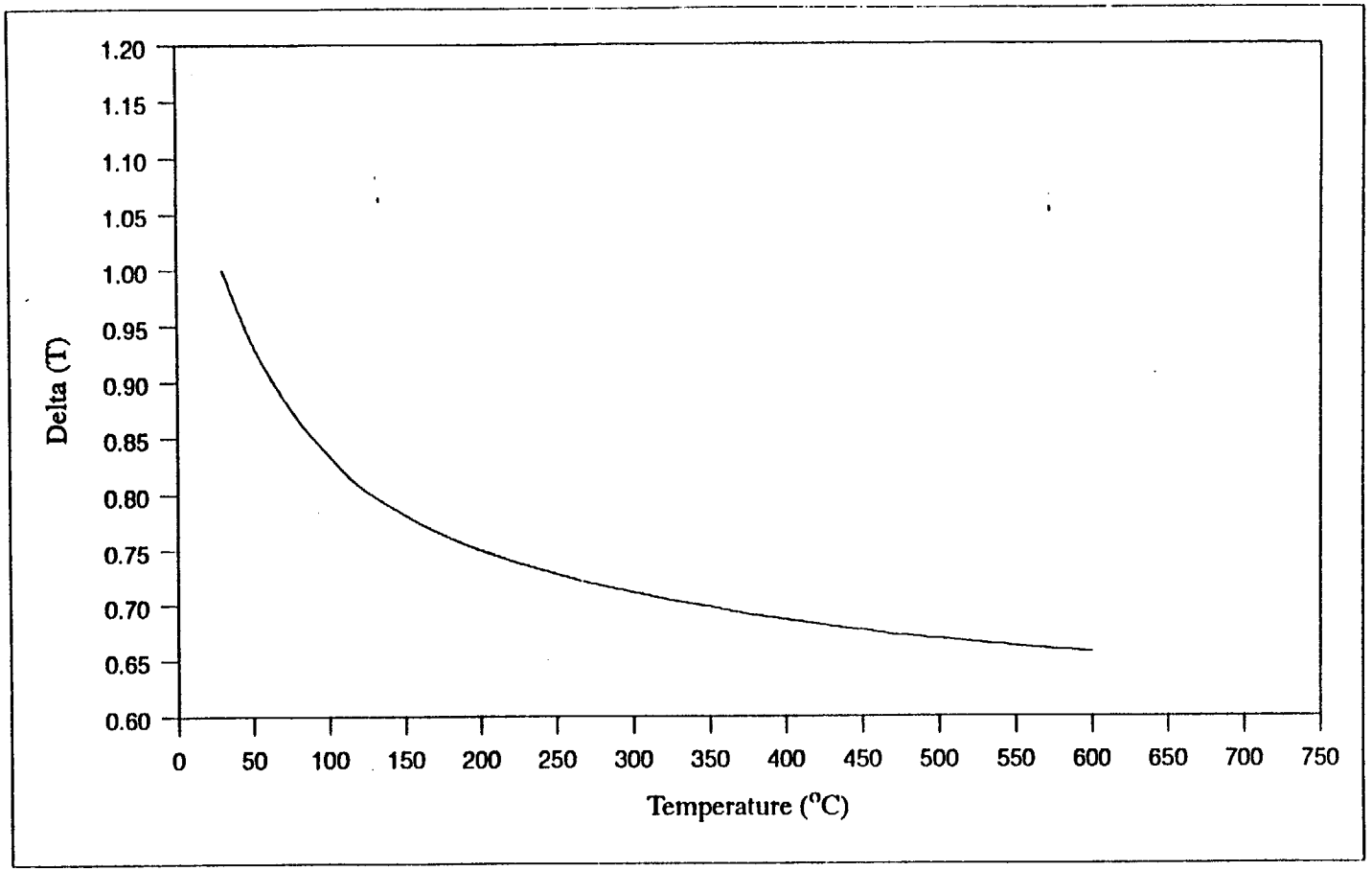

Figure 17. Delta (T) v Temperature for Gilsocarbon Graphite

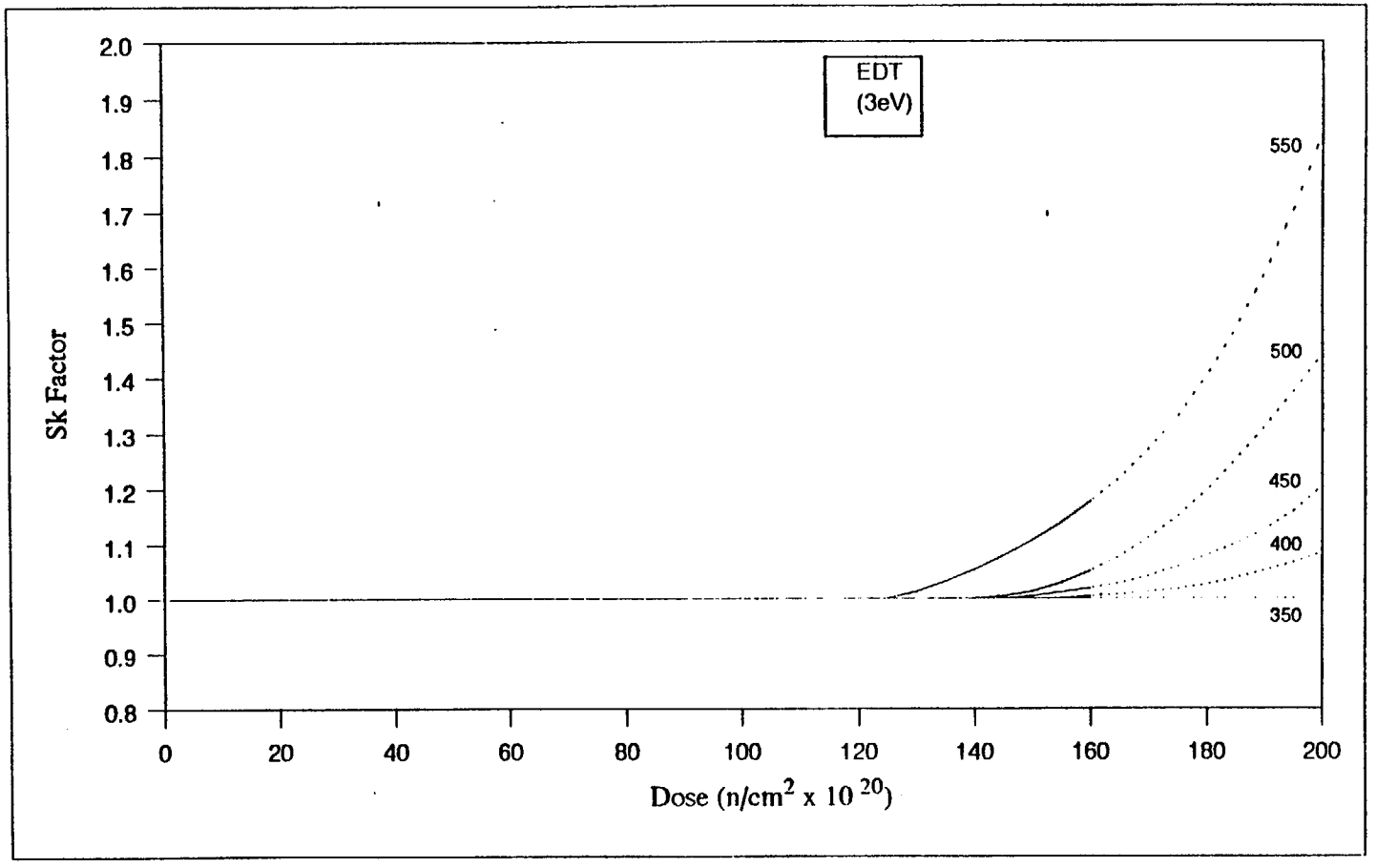

Figure 18. Sk Factor v Dose & EDT for Gilsocarbon Graphite

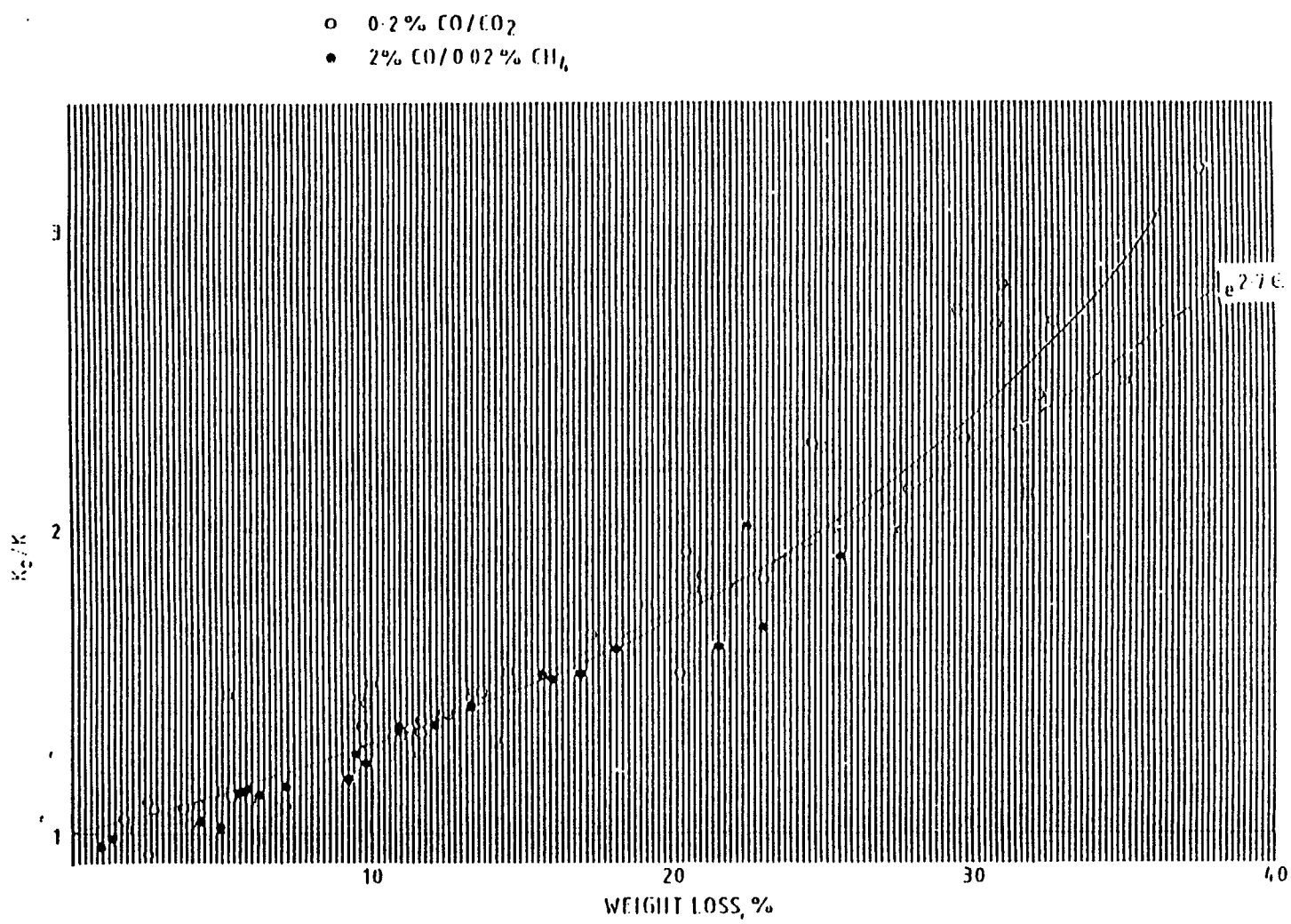

Figure 19. FRACTIONAL INCREASE IN THERMAL RESISTIVITY OF GRAPHITE CAUSED BY RADIOLYTIC OXIDATION

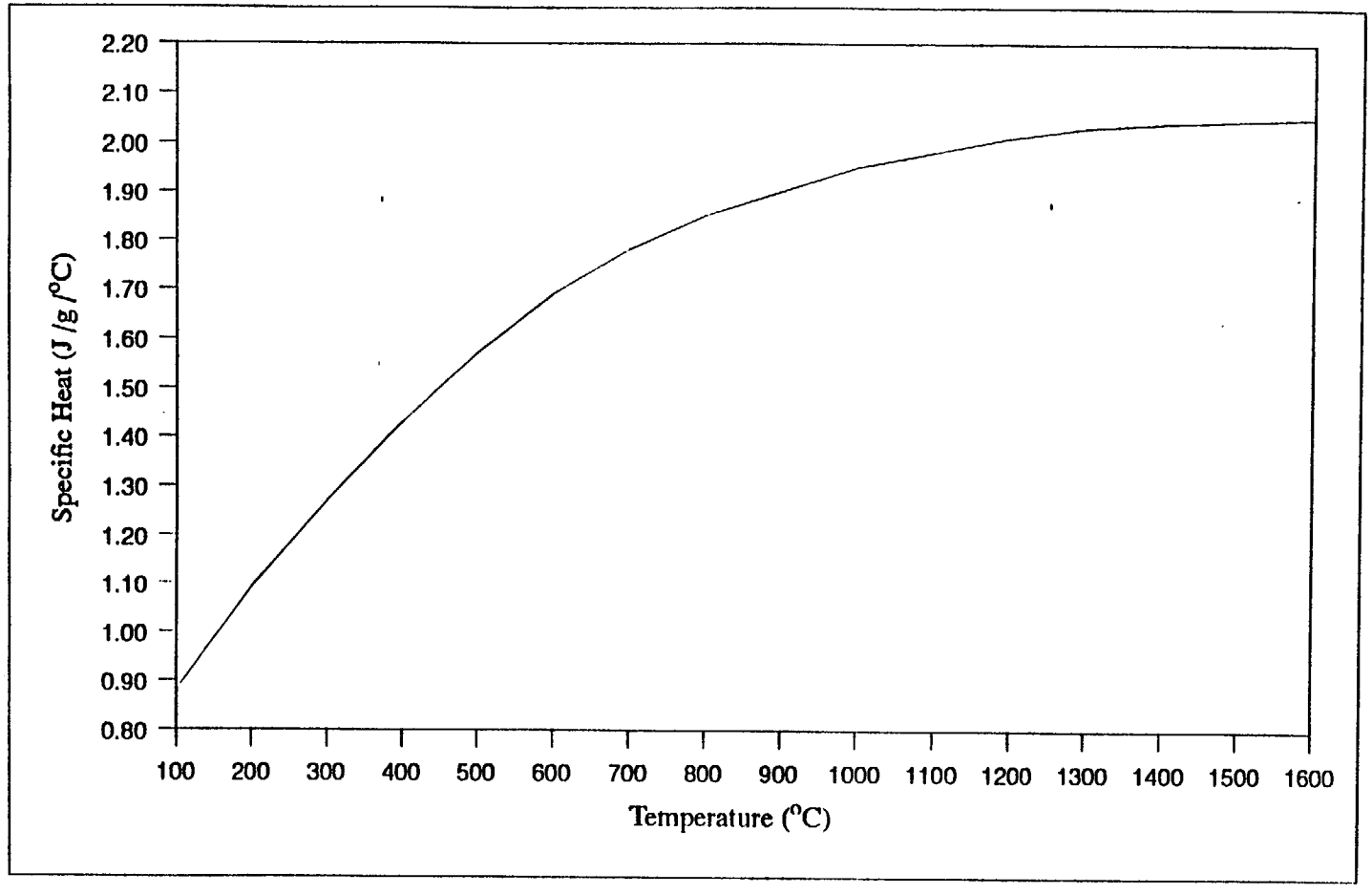

Figure 20. Specific Heat v Temperature for Gilsocarbon Graphite

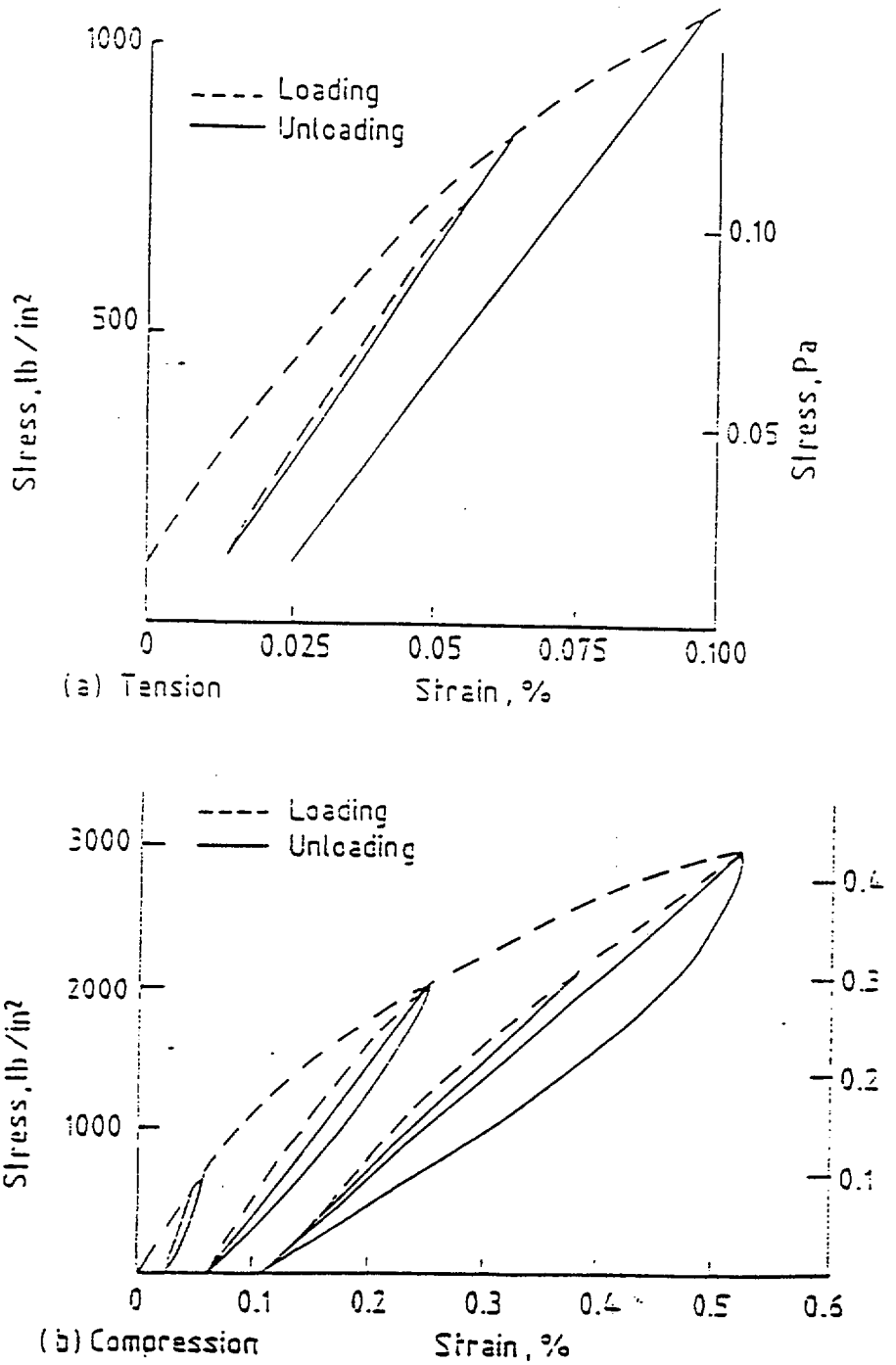

Figure 21. Stress-Strain Diagrams for Graphite

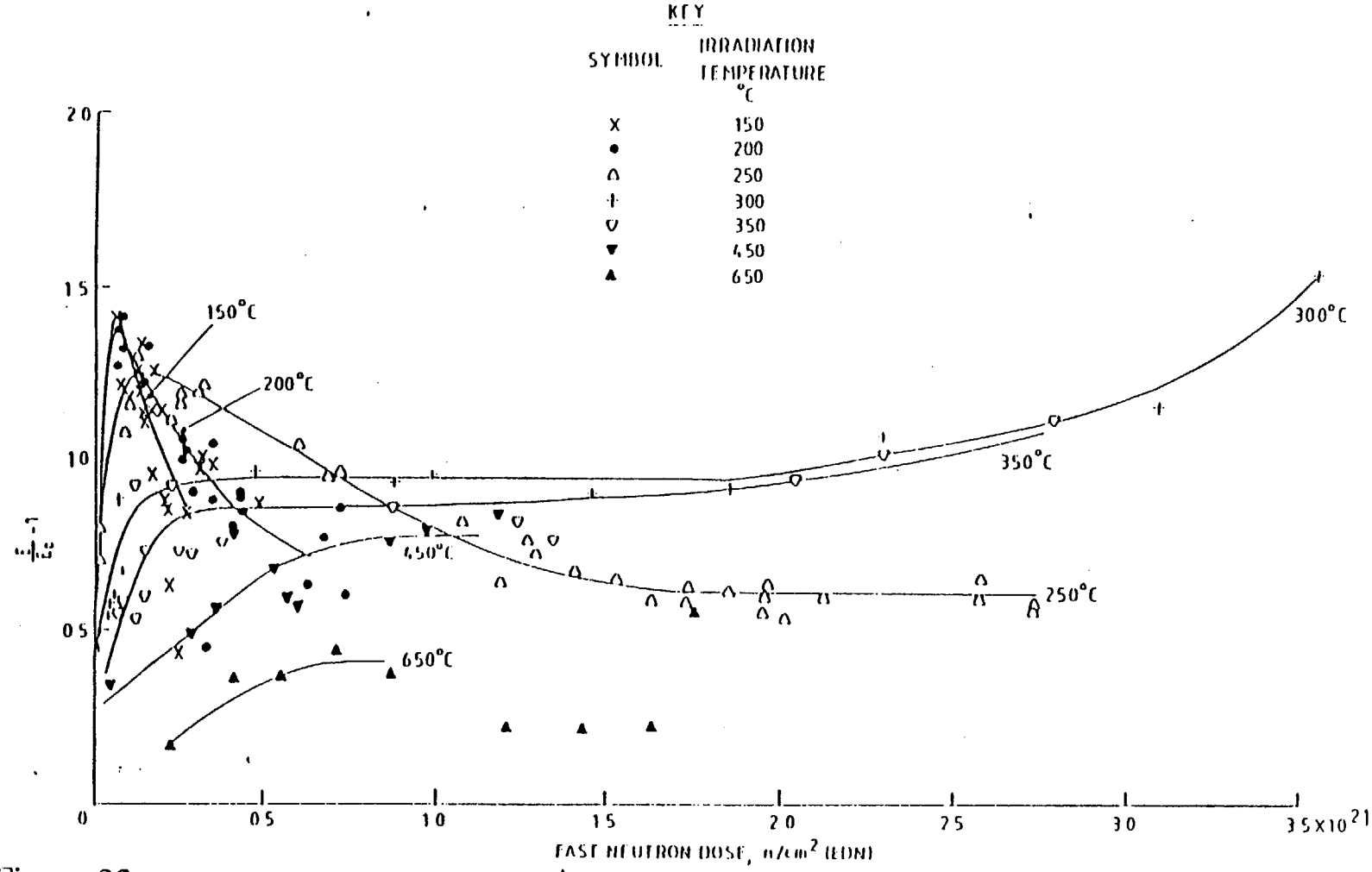

Figure 22. FRACTIONAL CHANGES IN YOUNG'S MODULUS WITH FAST NEUTRON DOSE: STANDARD DIDO Mk III HOLLOW FUEL ELEMENT DATA. PARALLEL TO EXTRUSION

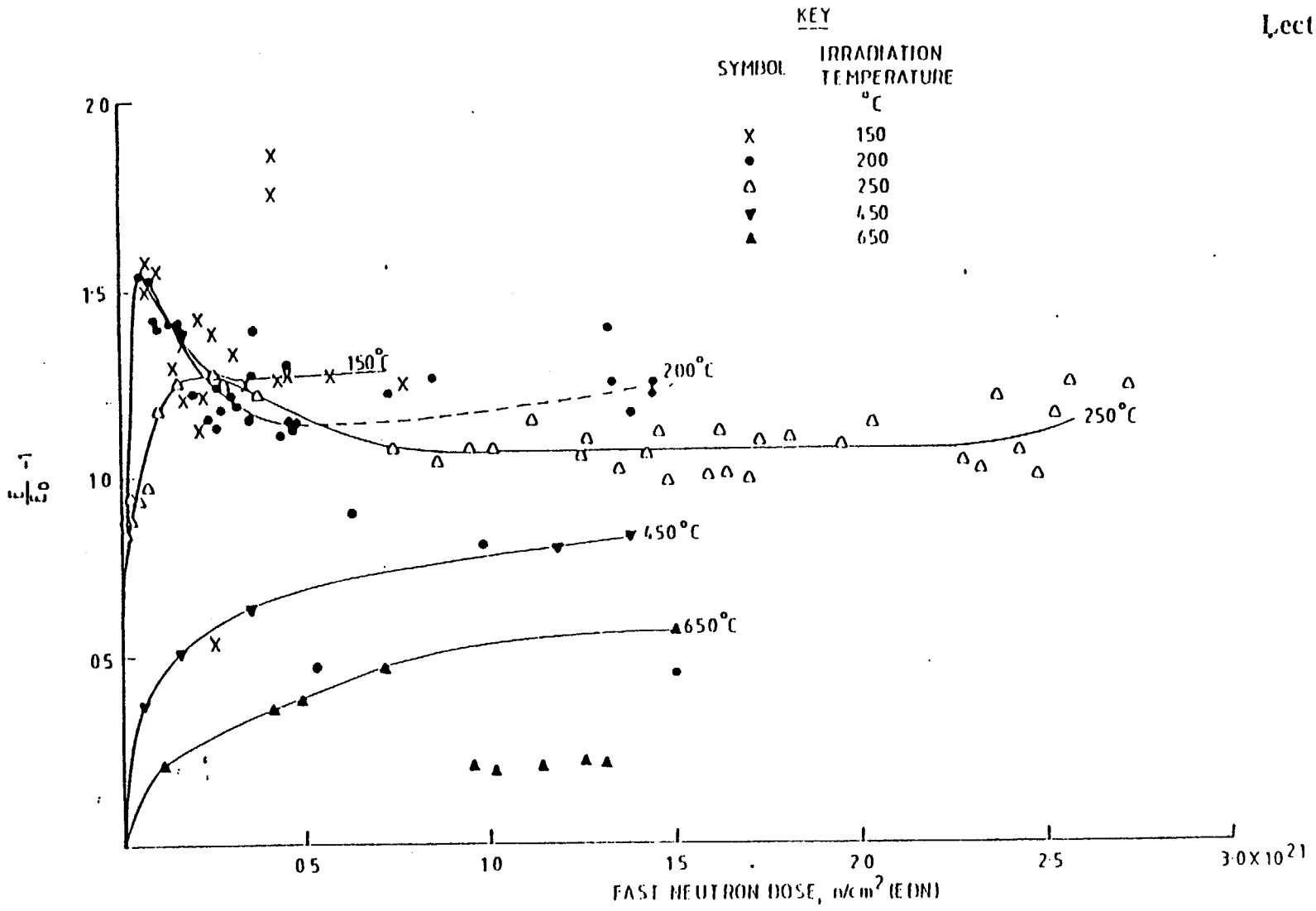

Figure 23. FRACTIONAL CHANGES IN YOUNG'S MODULUS WITH FAST NEUTRON DOSE: STANDARD DIDO MkIII HOLLOW FUEL ELEMENT DATA. PERPENDICULAR TO EXTRUSION

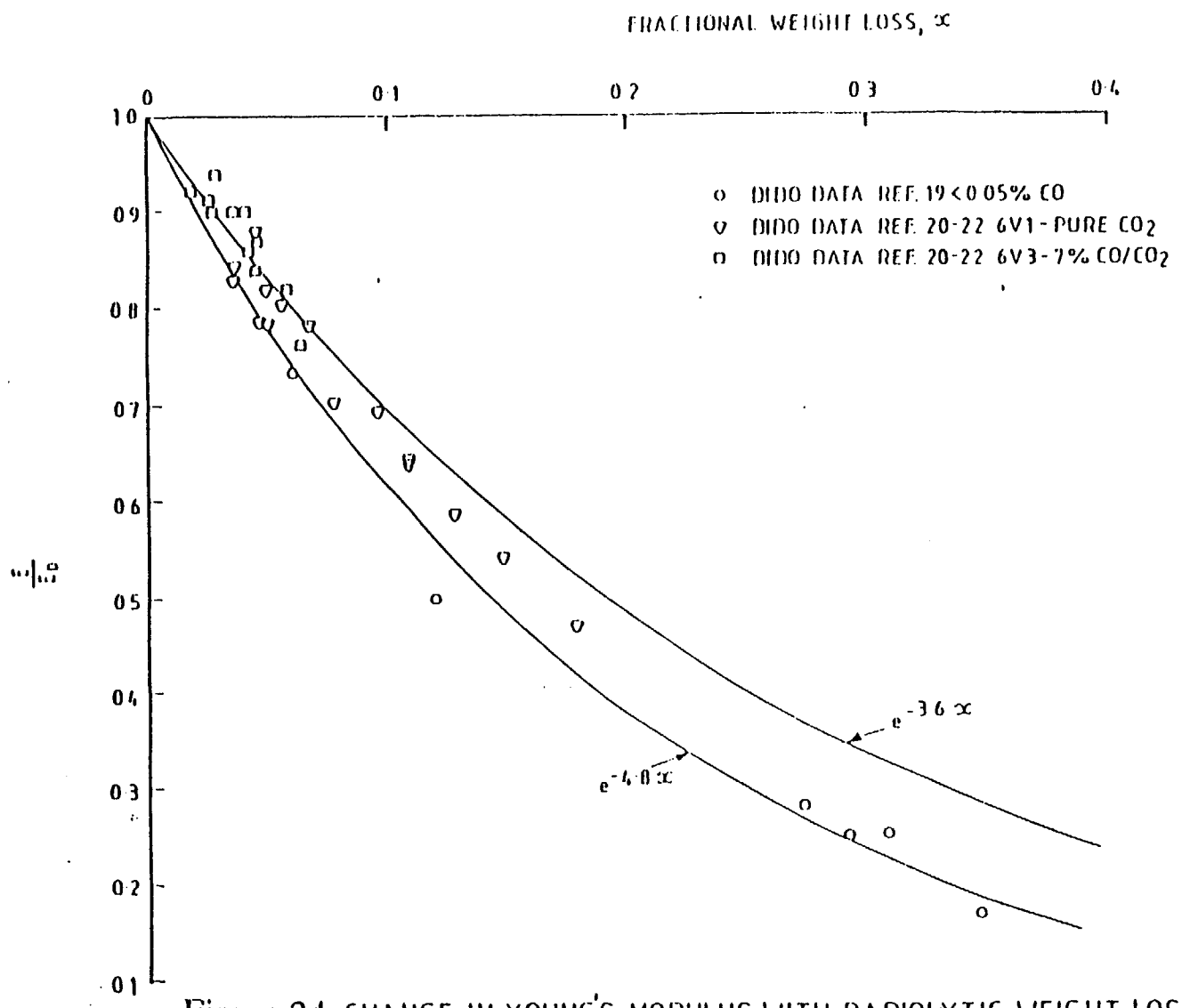

Figure 24. CHANGE IN YOUNG'S MODULUS WITH RADIOLYTIC WEIGHT LOSS

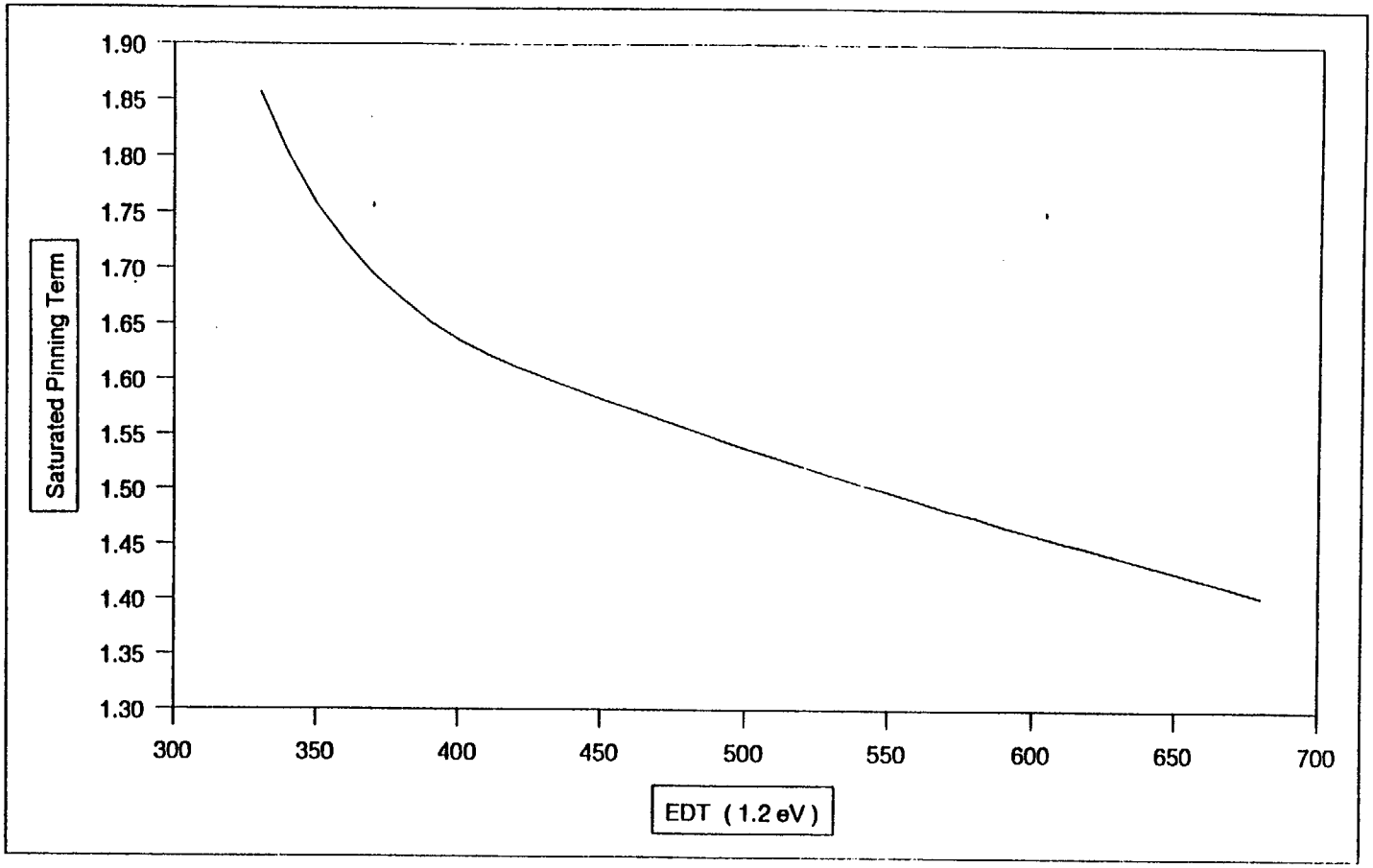

Figure 25. Saturated Pinning Term v EDT for Gilsocarbon Graphite

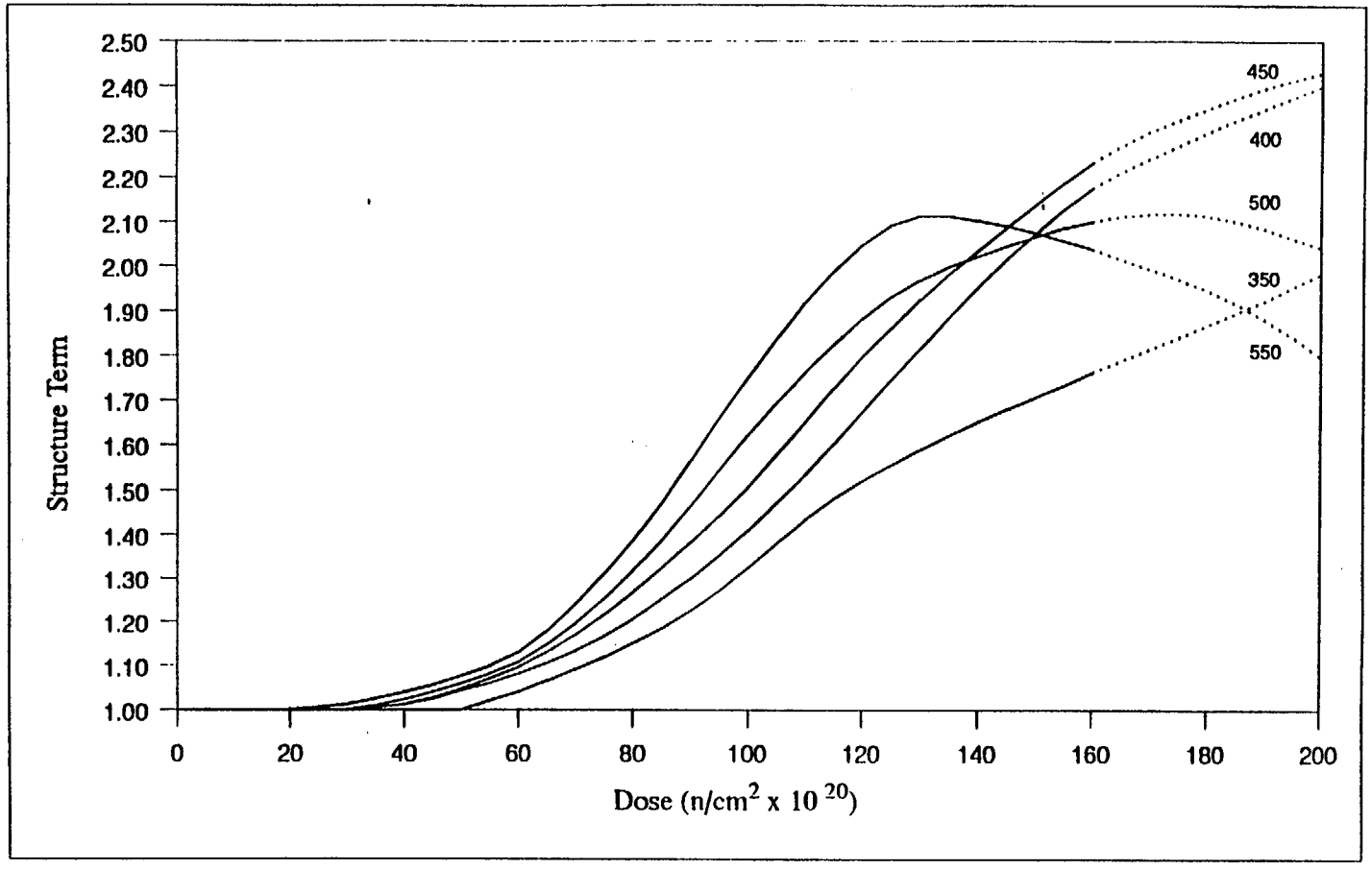

Figure 26. Structure Term v Dose & EDT for Gilsocarbon Graphite

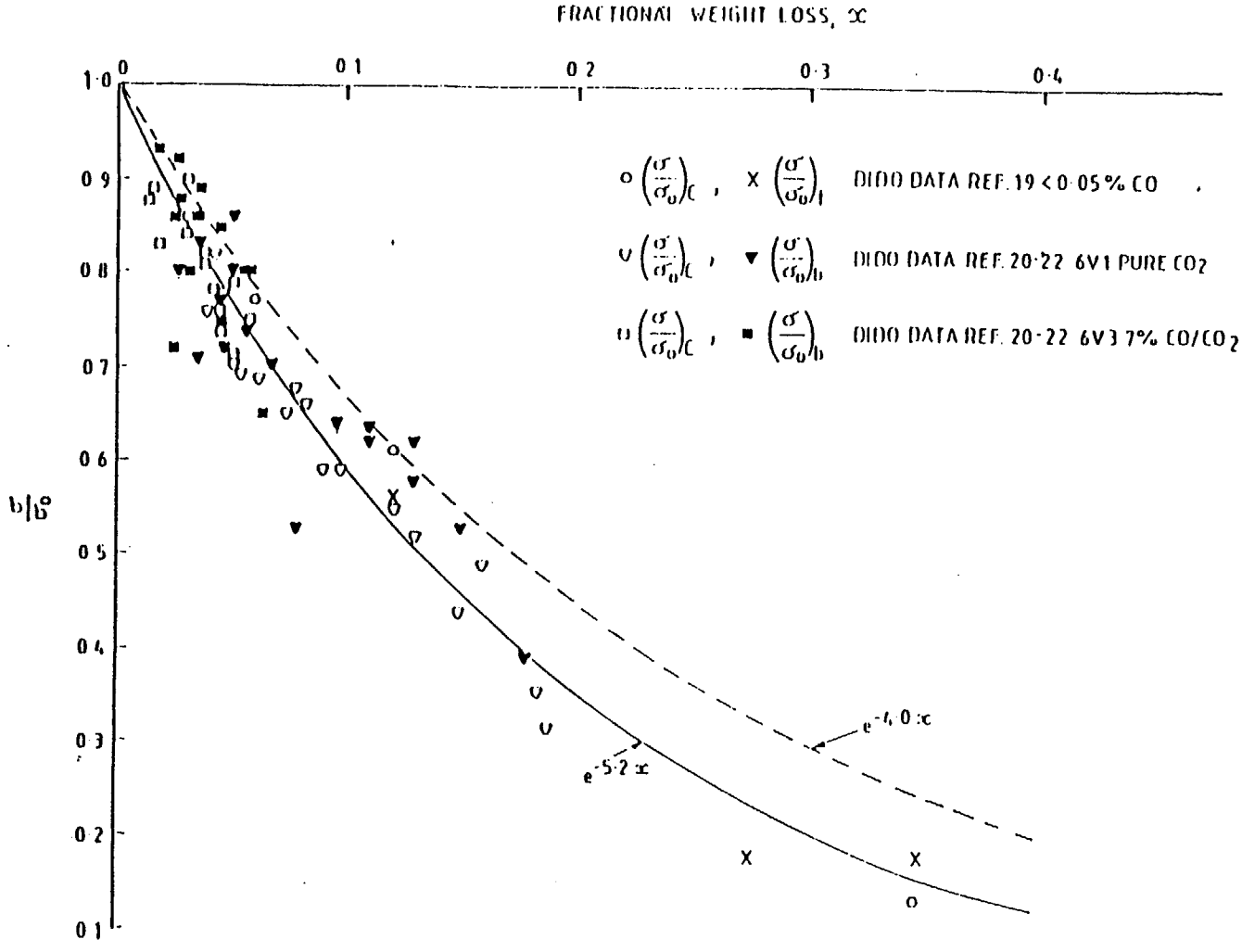

Figure 27. CHANGE IN STRENGTH WITH RADIOLYTIC WEIGHT LOSS

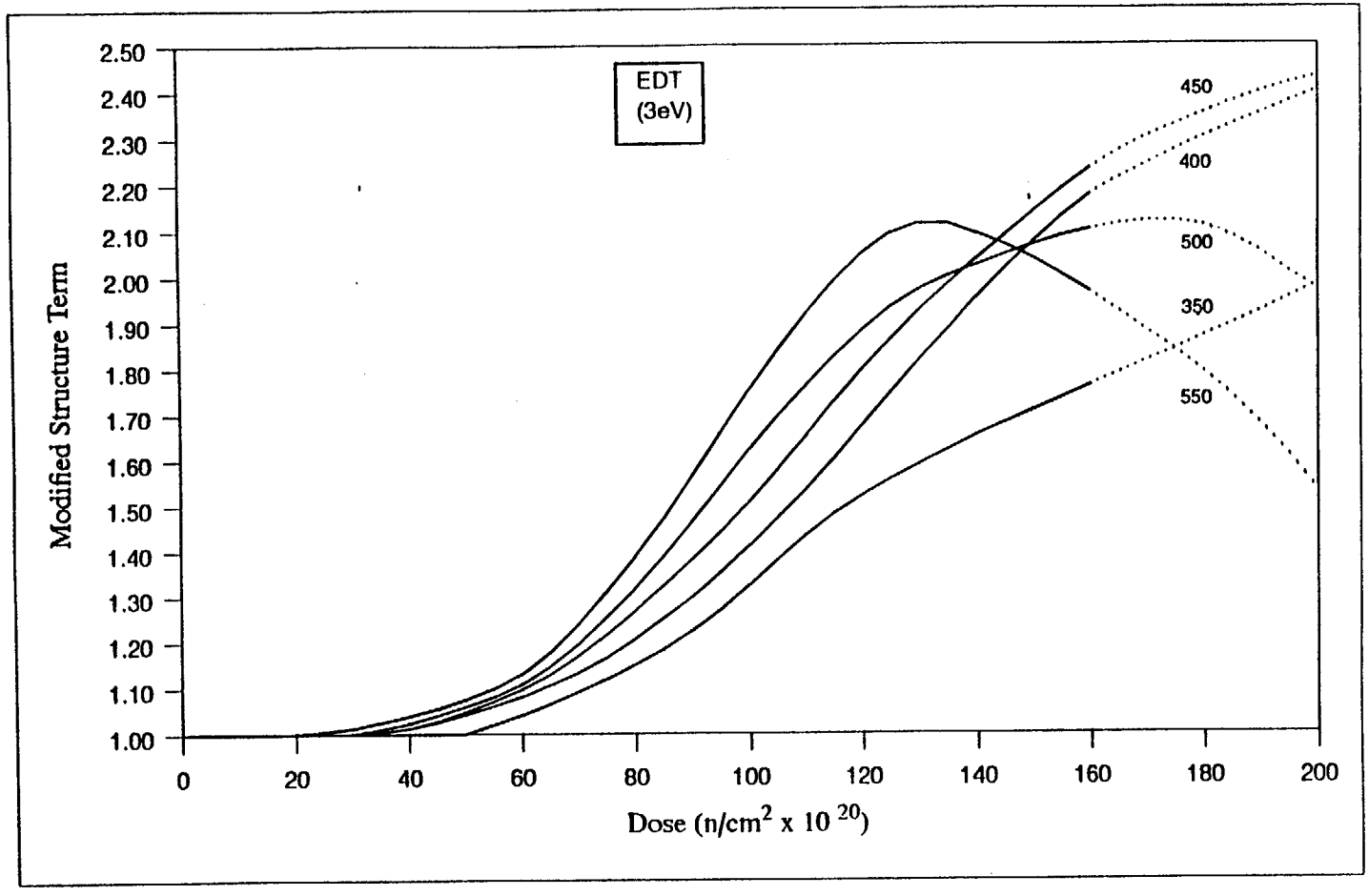

Figure 28. Modified Structure Term v Dose & EDT for Gilsocarbon Graphite

Fig 29. Stress required to fail in a single impact test versus the 3-point bend strength for different graphites

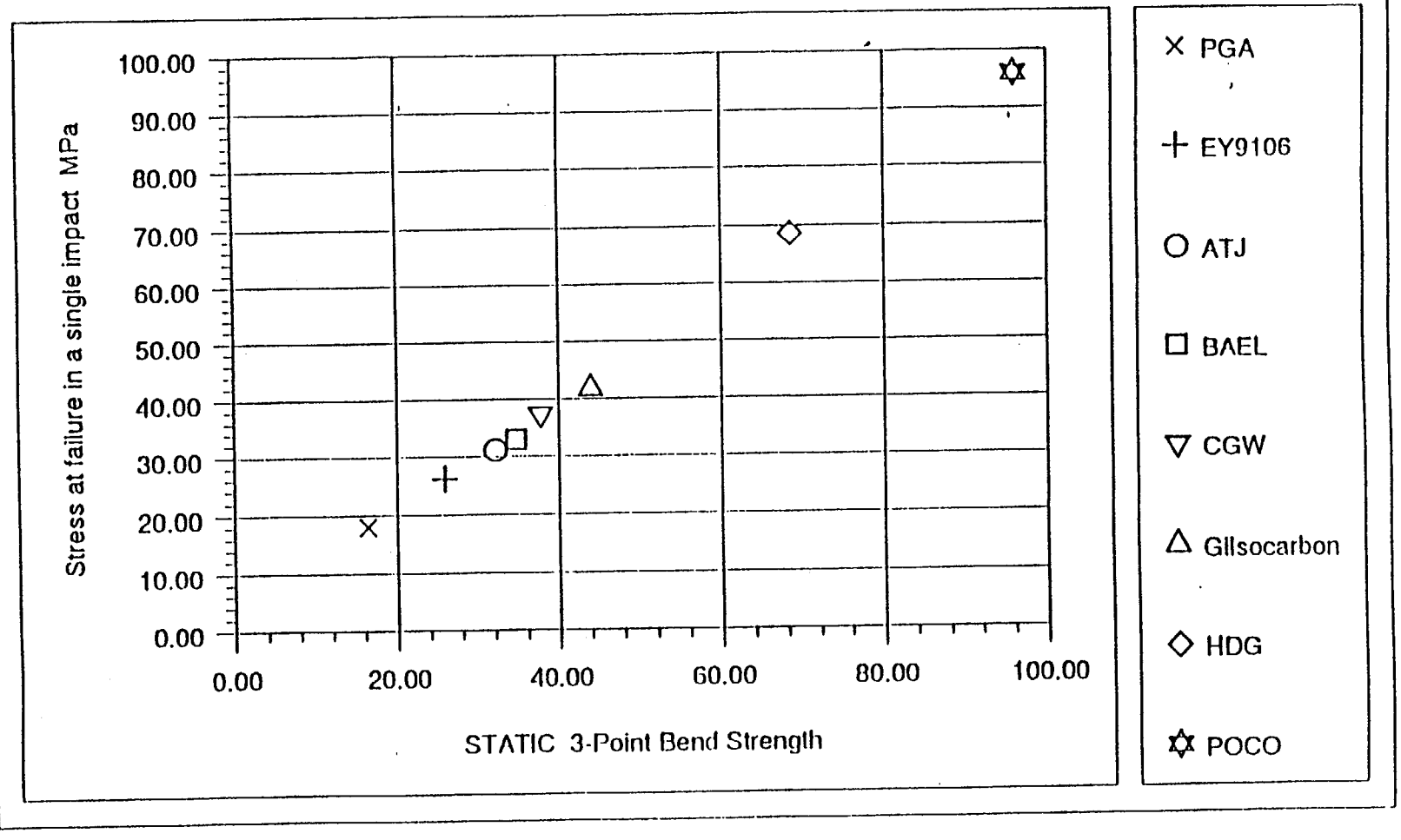

Fig 30. Energy required for failure of rod specimens after 50 impacts versus energy to fail 3-point bend specimen.

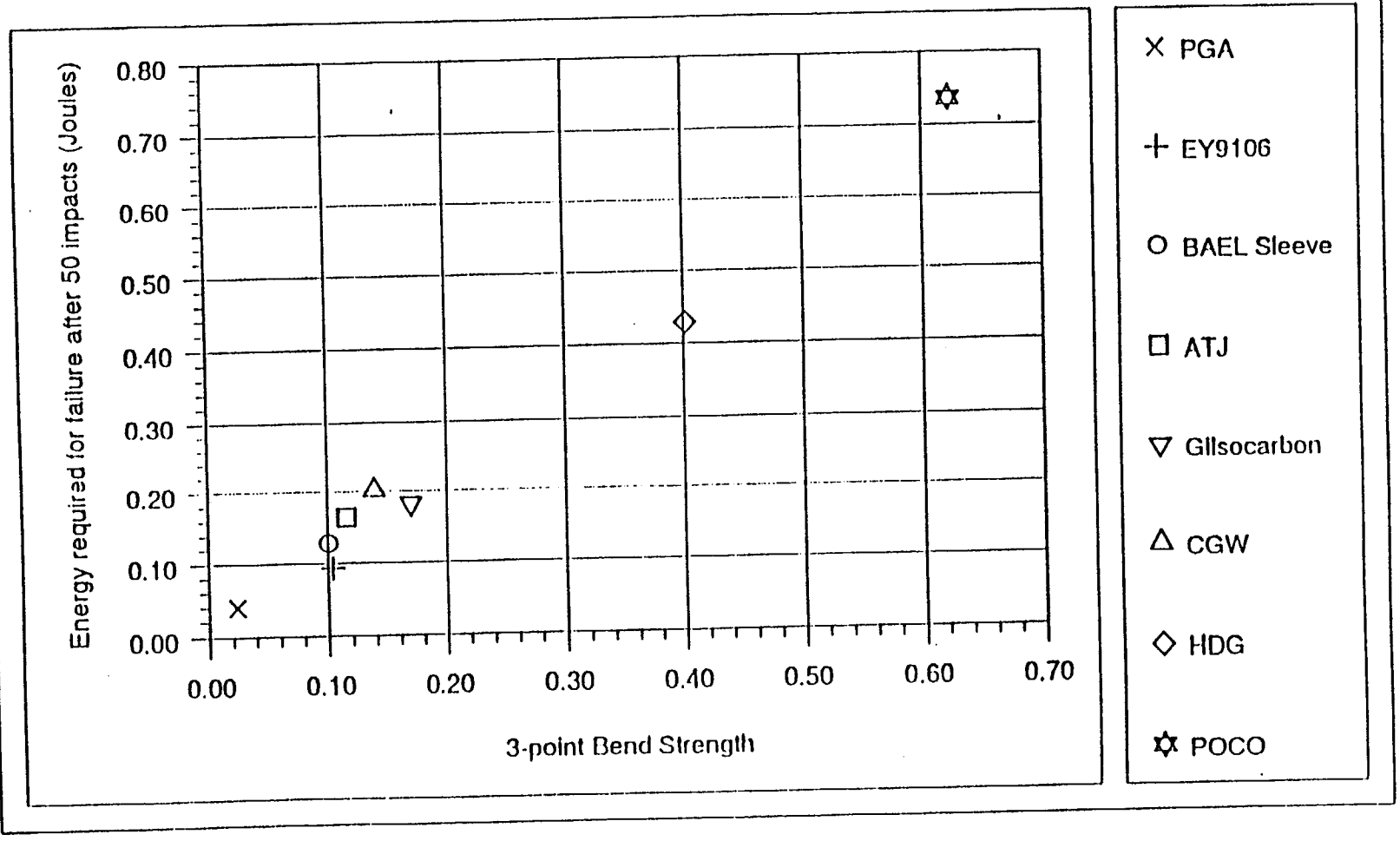

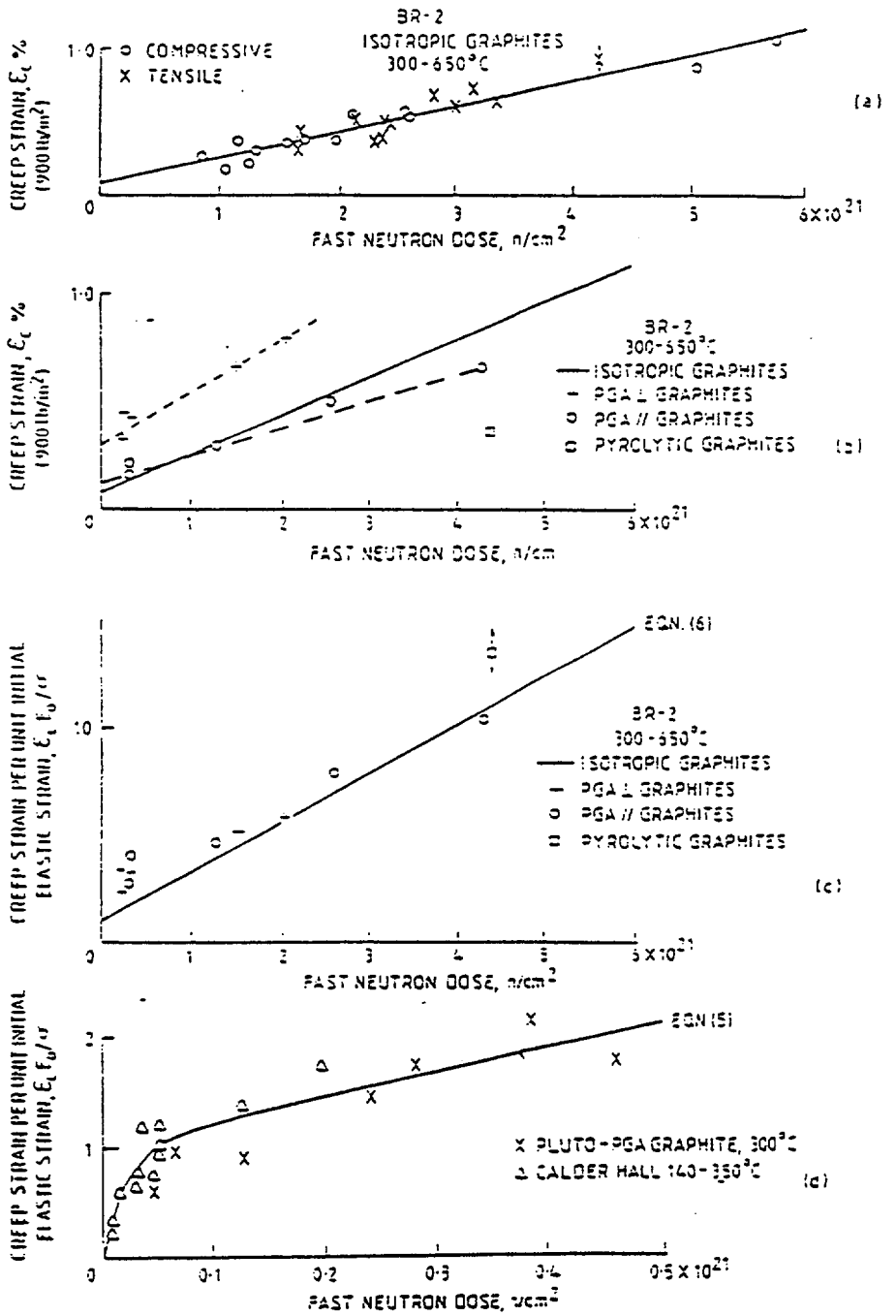

Figure 31. RELATION OF CREEP AND ELASTIC DEFORMATION OF DIFFERENT GRAPHITES INCLUDING PGA

GRAPHITE TECHNOLOGY COURSE

LECTURE 3

1. Thermal Oxidation in Air

Thermal oxidation of graphite in air is an important safety consideration in any situation where hot graphite may become exposed to air since the oxidation process is exothermic. A self-sustaining reaction, or even worse a runaway reaction, may ensue - particularly if stored energy is released as was the case in the Windscale Pile No 1 fire in 1957. Situations of interest in current safety studies include depressurisation by duct fracture of steel-pressure-vessel Magnox reactors, and waste disposal of irradiated graphite components by burial or other means.

Three possible reactions may occur in the presence of oxygen, and these may be represented by the following equations:

$$C + O_2 = CO_2$$

$$C + \tfrac{1}{2} O_2 = CO$$

$$CO + \tfrac{1}{2} O_2 = CO_2$$

All of the above reactions are exothermic, the first has the heat of reaction of 94k.cals/mole and the other two combine to give the same total end product and heat generation. With an excess of oxygen present mainly CO_2 will be produced, but with oxygen depletion such as may occur at high temperatures in large bricks due to diffusional control, the reaction may be limited to formation of CO.

1.1 Virgin Graphite Oxidation

In the presence of air, graphite temperatures have to be at least 300°C before any appreciable reaction will take place. The rate of oxidation increases with temperature, and numerous studies have shown that air reactivity is related empirically to temperature by the Arrhenius law:

$$AR = Ae^{-E/RT} \qquad (1)$$

where:

AR = Rate of graphite oxidation in air(air reactivity) usually expressed as fractional mass of original graphite consumed per unit time , μg/g.hr.

A = Pre-exponential constant, which is dependent upon both graphite type and the state of the graphite (ie whether virgin, irradiated, oxidised, contaminated, etc).

E = Activation energy, cal/mole, which is also dependent upon the state of the graphite.

R = Universal gas constant (= 1.986 cal/mole °C).

T = Temperature, °K

The standard measurement temperature for air reactivity is 400°C, and the value of air reactivity at 400°C for virgin graphite is largely dependent upon the purity of the material. For the commercial Magnox stations the mean virgin reactivity at 400°C is taken to be 3.2 μg/g.hr, but graphite variability is recognised by assuming a "rogue brick" reactivity of 10 μg/g.hr in fault studies using the RHASD computer code. It is important to recognise, however, that the graphite for each application will be different and dependent upon the method and raw materials of manufacture, and these may affect both the mean and spread values of air reactivity.

1.2 Activation Energy

Pure carbon has an activation energy of 60,000 cal/mole (usually expressed as 60 k.cal/mole), but quite low levels of contamination above about a few tens of ppm will reduce the activation energy to about 40 k.cal/mole. Very severe contamination may reduce the reaction rate to lower levels of the order of 30 k.cal/mole, but current studies generally assume a standard value of 40 k.cal/mole. However, whenever data are available on measured values of activation energy for a given application these should always be used. Figure 3.1 shows the effect on air reactivity rates at temperatures above 400°C of assuming different activation energy values.

Graphite is a porous material with a high surface area within the pore structure-typically 0.1 to 0.2 m^2/g. This can vary from one graphite to another leading to large variations in the pre-exponential constant A, and hence reactivity, while the activation energy, E, remains substantially constant. However, it should be noted that the nature of this in-pore oxidation leads to a breakdown in the Arrhenius law relationship (Equation 1) at high temperatures due to oxygen starvation within pores that are remote from external graphite surfaces. The reason for this is that in the majority of cases oxygen can only gain access to the interior pores by the process of diffusion. Furthermore, the by-products of oxidation (CO and CO_2) can only escape by diffusion. The diffusivity of gases within graphite is very much lower than in free space, and it is as a result of this low diffusivity that diffusional control can reduce the rate at which air reactivity increases with temperature. The transition to this stage depends upon a number of factors including component geometry, air reactivity and diffusivity, and would also be influenced by the existence of any pressure drops which induce permeable flow.

1.3 Effect of In-Pile Exposure

In-pile exposure causes the air reactivity of graphite to increase, and there are three possible ways in which this may occur:

i. By crystal damage due to fast neutron irradiation which creates crystal imperfections thus making more reaction sites available at which oxidation can occur.

ii. Due to radiolytic oxidation creating more porosity and hence surface area at which thermal oxidation in air may proceed.

iii. By contamination of the graphite during operation by materials which may either increase or inhibit the oxidation rate.

In this particular section we shall concentrate on the first two of these effects.

Whenever possible monitoring data should be used to establish relationships which define the increase in air reactivity of virgin graphite with fast neutron dose and radiolytic weight loss. Such data are available from Nuclear Electric's Commercial Magnox reactors from which the following equation has been derived for use in RHASD to calculate graphite heating under fault conditions of loss of coolant and air ingress:

$$Ri = Rv\{1 + 0.0035\ D.R\theta\} + 12.5\ \{1-\exp(-\frac{\tau}{3})\} \qquad (2)$$

where:

R_i	=	Irradiated air reactivity at 400°C in μg/g.hr
R_V	=	Virgin air reactivity at 400°C with a value of 3.2 μg/g.hr for regular use and a value of 10 μg/g.hr for the RHASD "rogue brick".
$D.R(\theta)$	=	Calder effective dose in MWD/Te(u)
τ	=	Graphite percentage weight loss due to radiolytic oxidation.

Data at other temperatures are then derived using an activation energy, E, of 40 kcal/mole since the combined effects of irradiation damage and radiolytic oxidation are assumed to have no effect on activation energy.

The use of Calder effective dose, $D.R(\theta)$, rather than Calder equivalent dose, D, is to take account of the fact that fast neutron irradiation at higher temperature produces less damage in graphite than is produced at lower temperatures due to the higher rate of annealing which takes place at high temperatures. The term Calder effective dose was coined in the early 1960's when it was believed that it correlated well with the measured increases in stored

energy and thermal resistivity. The relationship between $R(\theta)$ and Calder equivalent temperature is shown in Fig 3.2 from which it will be seen that $R(\theta)$ falls with increase in temperature up to a Calder equivalent temperature of ~380°C at which point a saturation level is reached. The relationship permitted reasonably accurate extrapolation of the limited data available at that time. Whilst the use of Calder effective dose has now been largely superseded, use of the term still persists in certain Magnox reactor applications such as air reactivity.

It is again emphasised that whilst equation 2 may be applicable to the Commercial Magnox Stations, a different relationship may well hold for other systems where appropriate data should be sought.

1.4 Contamination

Impurities create defects in the hexagonal lattice of graphite crystals which then act as sites for either enhancing or inhibiting the rate of air oxidation. Elements appearing in lower groups than carbon in the periodic table tend to be catalysts, notably metals. Many investigations have attempted to rank metals in order of catalytic effectiveness with very inconsistent results suggesting variability of experimental conditions and of the chemical form in which the metal was introduced, not to mention uncertainty in the initial impurity content of the graphite used. Some investigators have found lead to be the most catalytic metal which can give rise to increases of several orders of magnitude in graphite-air reactivity, whilst sodium, vanadium, manganese, silver, copper and ferrous metals all appear high on classification lists. Both lead and sodium (introduced as salt carried in the cooling) are suspected as contributors to increased air reactivity of the Windscale Pile graphite and hence as a possible cause of the 1957 fire. Very small amounts (~ a few ppm) of some contaminants can markedly affect air reactivity.

As has already been stated, E for pure carbon is ~60 k cals.mole, and with almost any contamination beyond a few tens of ppm causes a reduction in E to about 40 k cals/mole. Further reductions in E are possible for particular contaminants or very severe contamination.

Materials which inhibit air reactivity are defined as those materials added to the graphite which either seal the surface or which slow down the oxidation reaction by, for example, increasing the activation energy, E. The most significant inhibitors are the halogens (fluorine, chlorine, etc) and phosphorous, sometimes alone or in the form of compounds. One of the most effective inhibitors is $POCl_3$, whilst CCl_4 and CCl_2F_2 are known fire retardants.

Inhibitors are mainly of interest in the context of controlling or extinguishing graphite fires. Gaseous inhibitors are more appropriate in this context, and an inert gas such as nitrogen or argon would be suitable as a means of excluding oxygen. Carbon dioxide would inhibit graphite oxidation to negligible levels below about 700°C, but may not adequately suppress oxidation if other flammable materials are also present.

2. Radiolytic Oxidation in CO_2

2.1 Introduction

Two types of oxidation can occur in a CO_2 environment, namely thermal and radiolytic. Thermal oxidation is the purely chemical reaction between graphite and CO_2 which proceeds at a negligible rate below 625°C and is not important even for the hottest parts of AGR fuel sleeves operating at temperatures up to 675°C. Radiolytic oxidation, on the other hand, occurs when CO_2 is decomposed by fast neutron and gamma radiation (radiolysis) to form CO and an active oxidising species which reacts with the graphite. Graphite is a porous material and the oxidation takes phase predominantly within the graphite pores, proceeding at a rate which is proportional to the mass of CO_2 contained in the pores and the energy deposition dose rate absorbed by the CO_2, but is substantially independent of temperature within the range of practical interest. An explanation of the process of energy deposition in graphite is given in Appendix 3.1.

Radiolytic oxidation is important because the resultant weight loss may affect reactor economic performance by reducing moderating power and increasing permeability, and can cause significant changes in graphite properties and loss of strength. It is usually necessary to control the rate of oxidation since the weight loss in pure CO_2 would be intolerably high even in the relatively low-rated Magnox reactors. The oxidation rate is more than halved if the carbon monoxide concentration is allowed to build up naturally to about 1% by volume, and may be further reduced by the planned injection of minor concentrations of hydrogen and moisture. Whilst such measures are found to be adequate for controlling the rate of radiolytic oxidation in Magnox reactors, the more highly-rated AGRs require a more effective inhibitor such as methane which can reduce the rate of attach by about a factor of 10.

2.2 Standring Equation for Weight Loss

Radiolytic oxidation in Magnox reactors is generally assumed to occur uniformly throughout the open pore structure at a rate proportional to the radiation dose rate to the CO_2 contained within those pores. Standring[1] has derived a general expression for calculating the oxidation rate which has formed the basis for all graphite weight loss assessments and experimental analysis in the radiation chemistry field for many years. The derivation is as follows:

Consider a 1-g specimen of open porosity ϵ cm^3/g being oxidised by CO_2 at pressure p lb/in^2 absolute, temperature T°K and energy deposition dose rate, D W/.g, to graphite (and therefore to CO_2). [Pressure is expressed in lb/in^3 since these were the units most commonly used in reactor specifications.] Then the weight of CO_2 in the open pores:

$$= \varepsilon \rho_o \frac{p}{14.7} \frac{273}{T} g$$

where ρ_o = density (s.t.p) of CO_2 (1.98×10^{-3} g/cm^3).

The dose rate to the gas in the specimen:

$$= \varepsilon D \rho_o \frac{p}{14.7} \frac{273}{T} W$$

$$= \varepsilon D \rho_o \frac{p}{14.7} \frac{273}{T} \frac{10^{19}}{1.6} eV/sec$$

If G_{-c} represents the number of atoms of carbon gasified per 100 eV of energy absorbed by the gas, then in the 1-g specimen the rate of gasification

$$= \varepsilon D \rho_o \frac{p}{14.7} \frac{273}{T} \frac{10^{19}}{1.6} \frac{G_{-c}}{100} atoms/sec$$

$$= \varepsilon D \rho_o \frac{p}{14.7} \frac{273}{T} \frac{10^{19}}{1.6} \frac{G_{-c}}{100} \frac{12}{6 \times 10^{23}} g/sec$$

$$= 2.32\ 10^{-5} \frac{\varepsilon G_{-c} Dp\ \rho_o}{T} g/sec$$

substituting for $\rho_o = 1.98 \times 10^{-3}$ g/cm^3, this becomes

$$Rate = 1.656 \times 10^{-4} \times \frac{\varepsilon G_{-c} Dp}{T} g/g, h \quad (3)$$

$$= 145 \frac{\varepsilon G_{-c} Dp}{T} \% \text{ per year} \quad (4)$$

2.3 Controlling Parameters in the Standring Equation

2.3.1 Dose Rate

The energy deposition dose rate term, D, is a measure of the total energy absorbed in unit time from the scattering of γ- radiation and fast neutrons in the derivation of equation 3 it is assumed that the rate received by the graphite is the same as that absorbed by CO_2 in the pores of the graphite. In 1962, using a theoretical approach it was shown that a fraction k of the fission energy from the fuel caused heating in the moderator. From this the following equation for the mean dose rate to the moderator was derived:

$$D = \frac{kP}{W} \quad W/g$$

where: P = Reactor thermal power, MW
W = Weight of active core graphite (excluding reflectors), tonnes

k is typically 0.056 for the Calder reactors but higher at about 0.086 for AGRs

It is important to note that significant spatial variations in dose rate will occur within the graphite moderator and these are from two main sources. Firstly, there are axial and radial variations in dose rate within the core, so that axial and radial form factors must be applied to the mean dose rate, D, when evaluating peak values. The peak value may be determined from the equation:

$$D_{max} = \frac{D}{fa.fr}$$

where:

$$fa = \frac{mean\ fuel\ rating\ in\ a\ channel}{maximum\ fuel\ rating\ in\ a\ channel}$$

$$fr = \frac{mean\ channel\ rating}{maximum\ channel\ rating}$$

Secondly , there will be a marked radial variation in dose rate within the unit cell of any given reactor and this must also be taken into account when calculating the distribution of radiolytic weight loss within the unit cell. The variation is such that the dose rate will decrease in a radial direction away from the fuel element. It is possible to calculate the shape of the dose distribution curve for any given reactor parameters using reactor physics codes such as WGAM and MCBEND; a typical result for an AGR unit cell is shown in Fig 3.3.

Finally , it is important to recognise that the dose rate, D, in equations 3 and 4 above is the dose rate to the graphite moderator at the start of reactor life. Loss of moderator due to radiolytic oxidation will reduce the weight of graphite in the active core, and hence the dose rate will increase with time. The effect on weight loss of the progressive increase in dose rate with time is dealt with later in Section 2.3.5. The reduction in dose rate with time which occurs in every unit cell due to the fall in fuel rating attributed to reactivity loss is usually dealt with by averaging out such effects over the life of the fuel.

2.3.2 Pressure and Temperature Terms

The variations in pressure and temperature change the density of the gas in the graphite pores in the normal manner described by the Gas Laws. Experiments have shown that no other corrections for pressure and temperature are required for dependency of other terms in equations 3 and 4.

2.3.3 The G-c Term

The oxidation rate constant G-c is strictly only applicable to oxidations in pure CO_2 and is independent of pressure, temperature and graphite type. For a fixed set of conditions, different graphites exhibit different oxidation rates due to their different open porosity as demonstrated earlier. By definition, G-c is a measure of the number of atoms of carbon gasified by the oxidising species produced adjacent to the graphite surface by the absorption of 100eV of energy in the CO_2.

G-c varies with coolant gas composition. Although estimates vary, the generally accepted value for pure CO_2 is 2.35. The reason for any uncertainty is the experimental difficulty of ensuring the complete absence of carbon monoxide from the CO_2. The mechanism of radiolytic oxidation is represented by the following equations:

Gas Phase

$$CO_2 \xrightarrow{\text{radiation}} CO + O^*$$

$$CO + O^* \longrightarrow CO_2$$

Graphite Surface

$$O^* + C \longrightarrow CO$$

where O^* is an active oxidising species formed by radiolysis of CO_2.

Carbon monoxide thus inhibits radiolytic oxidation by gas phase de-activation of the active oxidising species. The presence of only 1% of CO can reduce G-c by a factor of about 2 as may be seen from Fig 3.4 which is a plot of the experimental data that fits the relationship:

$$G\text{-}c = 1.05 + \frac{1.32}{1 + 8.5[CO]}$$

where [CO] is the carbon monoxide concentration in volume percent.

Further reductions in G-c are possible by the addition of low concentrations of moisture to coolants containing carbon monoxide. The data from experiments at 1.2% CO are shown in Fig 3.5 from which reductions in G-c due to moisture effects of up to 35% are apparent.

Much larger reductions in G-c are possible by the use of methane as an inhibitor. The effect is shown in Fig 3.6 which demonstrates that methane is more effective in reducing G-c than is the case with moisture. The use of methane as an inhibitor of radiolytic oxidation has been largely confined to AGRs where high inhibition factors are required to negate the effects of higher dose rates. For AGR applications, the use of G-c is not appropriate since with methane inhibition the oxidation process no longer proceeds at a uniform rate throughout the pore structure. This topic is covered in Section 3 of these notes.

2.3.4 The Porosity Term

The initial open porosity, ε_o, of any individual piece of graphite can be determined by measurement, and the value so obtained used in equations 3 and 4 to calculate the oxidation rate. However, as is described below, synthetic graphites usually exhibit in rapid increase in open porosity during the very early stages of oxidation and a more reliable estimate of the initial oxidation rate and its subsequent increase with weight loss is obtained by making allowance for this effect. To do this it is necessary to use the "effective" initial open porosity, ε_e, instead of ε_o in equations 3 and 4. It should also be noted that the convention of expressing oxidation as a percentage of the original weight automatically requires porosity to be expressed in cm^3/g. However, when studying increases in porosity with in-pile oxidation it is more suitable to use cm^3/cm^3, π_o.

The total porosity, π_T, of graphite comprising both open pores, π_o , and closed pores, π_c, and these are related to bulk density, ρ_B, by the following equations:

$$\pi_T = \left(1 - \frac{\rho_B}{\rho_C}\right) cm^3/cm^3 \qquad (5)$$

$$\pi_o = \left(1 - \frac{\rho_B}{\rho_{He}}\right) cm^3/cm^3 \qquad (6)$$

$$\pi_C = \rho_B \left(\frac{1}{\rho_{He}} - \frac{1}{\rho_C}\right) cm^3/cm^3 \qquad (7)$$

where: ρ_c = crystal density of graphite (2.23 g/cm^3)

ρ_{He} = Helium density of graphite, g/cm^3

Note that the helium density is based on the total volume of crystals and closed pores contained within a given mass of graphite. Helium density is therefore lower than crystal density, but is higher than bulk density.

The treatment of porosity changes in Magnox reactors where PGA is radiolytically oxidised in coolant gas comprising carbon dioxide with additions of carbon monoxide and moisture but with little or no methane present, and where the oxidation may be considered to occur uniformly throughout the porous structure, can be carried out using the following approach developed by Standring[1].

Unoxidised PGA has an open porosity amounting to about 20% of the bulk volume of the graphite whilst a further 4 to 6% is closed porosity which is inaccessible to the coolant gas. Experimental work has shown[1] that approximately 40% of this closed porosity is opened up before the graphite has sustained 2% weight loss, whilst subsequent oxidation only increases the o.p.v. in proportion to the weight loss, Fig 3.7. The constant of proportionality is the reciprocal of the helium density which is constant from 2% up to at least 30% oxidation, since this allows for enlargement of open pores plus an opening up of the closed pores, both occurring in proportion to the graphite consumed. There is evidence that much of this initial 40% of closed-pore volume opens up at very low oxidation (0.04%) and it has therefore been recommended that it should all be assumed to open up instantaneously at the commencement of oxidation. The subsequent increase in open pore volume can be represented by the equation:

$$\pi_x = \pi_e + \frac{\rho_{Bo}}{\rho_{He}} \cdot \frac{x}{100} \qquad (8)$$

where: π_x = Open pore volume at x% oxidation, cm^3/cm^3

π_e = Effective initial open pore volume, cm^3/cm^3

ρ_{Bo} = Initial mean bulk graphite density, g/cm^3

ρ_{He} = Mean helium density after 2% oxidation, g/cm^3

Thus the initial rate of graphite oxidation given by equations 3 and 4 would use effective open pore volume, ε_e, and become:

$$g_o = 1.656 \times 10^{-4} \times \frac{\varepsilon_e G_c D p}{T} \quad g/g\ hr \qquad (9)$$

$$= 145 \frac{\varepsilon_e G_c D p}{T} \quad \% \text{ per year} \qquad (10)$$

where: g_o = initial rate of graphite oxidation per unit time

It can be shown that allowance for the effect of increasing porosity on cumulative weight loss, C_t, can be made by use of the following equation[1] , which assumes that:

i. All gas in an open pore of any size is equally effective in gasifying graphite at the walls of that pore.

ii. Dose rate to the graphite is constant.

$$C_t = A \left[\exp \frac{g_o t}{A} - 1 \right] \qquad (11)$$

where: C_t = Percentage weight loss in t years

g_o = Initial oxidation rate at t = o, percent per year, from equation 10

$A = \frac{100\pi_e}{(1 - \pi_e)}$

Curves of cumulation weight loss, C_t, versus $g_o t$ for constant dose rate to gas are shown in Fig 3.8 for selected values of π_e.

2.3.5 Cumulative Weight Loss and Constant Reactor Power

Equation 10 may be written in a different form in which the dose rate term, D. is substituted by kP/W as in equation 3. Thus:

$$g_o = 145\ \varepsilon_e G_c \frac{kP}{W} \cdot \frac{p}{T} \quad \% \text{ per year} \qquad (12)$$

From equation 12 it will be apparent that the rate of weight loss will increase with loss of moderator mass, W, if reactor power remains constant. Standring has again shown[1] that cumulative weight loss, C_t, for a reactor operated at constant power is governed by the equation:

$$\frac{A^2}{100\pi_e} \log_e \left(1+\frac{C_t}{A}\right) - \frac{A}{100} C_t = g_o.t \qquad (13)$$

The use of this equation yields higher cumulative weight losses than are obtained using equation 11 as may be seen from Fig 3.9 which gives the resultant curves of C_t versus $g_o t$, and which may be compared with the corresponding curves for constant dose rate seen in Fig 3.8.

2.4 DIFFUSE Code

The treatment radiolytic oxidation in Advanced Gas-Cooled Reactors is radically different and much more complex than that employed in Magnox reactor weight loss calculations, and the reasons for this are as follows. Methane is a significantly more effective inhibitor than carbon monoxide. It inhibits by forming a protection species on the surface of the graphite pores which then competes with the graphite for the active oxidising species that escape deactivation by the carbon monoxide. The mechanism for radiolytic oxidation and inhibition can be represented by the following equations:

Gas Phase

CO_2 ——————> $CO + O^*$

$CO + O^*$ ——————> CO_2

CH_4 ——————> P

where O^* is the active oxidising species formed by radiolysis of CO_2 and P is a protection species formed from methane oxidation.

Surface

$$O^* + C \longrightarrow CO$$

$$O^* + P \longrightarrow OP$$

where OP is the deactivated gaseous product of methane destruction.

Experimental data indicate that the protective species is extremely effective in suppressing radiolytic oxidation, and indeed for methane concentrations of practical interest, oxidation in the large majority of the pores is virtually eliminated. However, it appears that methane is denied access to some parts of the pore structure, and it is in these pores - known as the reactive pores - where the oxidation is concentrated. It is for this reason that the Standring equations no longer apply and, as will be seen later, a different approach is required.

The methane that is destroyed within the graphite pores must be replaced if inhibition is to remain effective. However, the rate of methane destruction is quite high in relation to the gas flow rates due to permeation and diffusion, and hence there may be a significant reduction in methane concentration at positions within the bricks which are remote from external surfaces. A further complication arises from the fact that methane destruction and radiolytic oxidation result in the formation of water and carbon monoxide within the pore structure, and for similar reasons the concentrations of these constituents builds up to higher levels within the bricks. Since both methane destruction rates and radiolytic oxidation rates are functions of all these minor constituents in the coolant gas, it is necessary to determine their distribution within the graphite bricks taking into account not only pore structure changes but also the numerous external factors which influence these complex processes.

The governing equations for evaluating coolant composition distribution within two-dimensional geometries must be solved by computer techniques, and the DIFFUSE code was developed for this purpose. Having solved for methane, carbon monoxide and water profiles the code is then required to determine radiolytic oxidation and weight loss profiles as a function of time, and this is done using finite elements. Several versions of DIFFUSE have been developed, the more important of which are DIFFUSE 4 by Russell and DIFFUSE 6 by Davies[3]. Details of the DIFFUSE 6 code are given in Section 2.5.

2.5 Controlling Parameters in DIFFUSE 6 Calculations

2.5.1 Diffusion Equations

The basic unknowns in DIFFUSE 6 are the methane, C_1, moisture, C_2, and carbon monoxide, C_3, gas concentration profiles. These are calculated from the following set of second order differential equations:

$$\nabla^T (D_{10} \nabla(C_1)) - \nabla(v.C_1) - K_1 = 0 \quad (14)$$

$$\nabla^T (D_{20} \nabla(C_2)) - \nabla(v.C_2) + K_1 \, STOX + 0 \quad (15)$$

$$\nabla^T (D_{30} \nabla(C_3)) - \nabla(v.C_3) + K_1 \, STOX \, 1 + K_2 \, STOX \, 2 + 0 \quad (16)$$

The first term in each equation is the pure diffusion contribution, and the diffusion coefficients D_{10}, D_{20} and D_{30} are the effective diffusion coefficients in graphite of methane in CO_2, moisture in CO_2 and carbon monoxide in CO_2, respectively. (See Section 2.5.2). The second term in each equation is the contribution from porous flow (due to permeation), and υ is the velocity vector for CO_2 flow through porous media. (See Section 2.5.3).

The second term in each equation is the contribution from porous flow (due to permeation) and is defined in Section 2.5.3.

The last term(s) are the sink and source terms which define methane destruction, and moisture and carbon monoxide formation, and are defined in Sections 2.5.4 and 2.5.5.

2.5.2 Diffusion Coefficients

The free gas diffusion coefficients of gas 1 and gas 2 (eg methane in CO_2 moisture in CO_2 and carbon monoxide in CO_2), D_{12}, are obtained from the expression:

$$D_{12} = \frac{BT^{3/2}\sqrt{\frac{1}{M_1} + \frac{1}{M_2}}}{Pr_{12}^2 \, I_D} \quad (17)$$

where:

$$B = \left[10.7 - 2.46\sqrt{\frac{1}{M_1} + \frac{1}{M_2}}\right] \times 10^{-4}$$

T	=	Temperature, K
M_1, M_2	=	Molecular weights of the two gases
P	=	Absolute pressure in atmospheres
r_{12}	=	Mean collision diameter for the two gases, Ångstrom
I_D	=	Collision integral for diffusion given as a function of kT/ε_{12}

The collision diameter and integral used in equation 17 are obtained from standard tables using the mean value of ε_{12}/k defined by:

$$\frac{\varepsilon_{12}}{k} = \sqrt{\left(\frac{\varepsilon_1}{k}\right)\left(\frac{\varepsilon_2}{k}\right)}$$

where:	k	=	Boltzmann constant, 1.38×10^{-6} ergs/k
	ε_{12}	=	Energy of molecular interaction

Standard values of ε/k are available for carbon dioxide, methane, carbon monoxide and water.

The effective diffusion coefficient in graphite is very much lower than in free gas and is given by:

$$D_{eff} = \lambda D_{12} \qquad (18)$$

where λ is the ratio of diffusion in graphite to diffusion in free gas.

D_{10}, D_{20} and D_{30} in equations 14, 15 and 16 are the effective diffusion coefficients in graphite of methane in CO_2, moisture in CO_2, and carbon monoxide in CO_2, respectively.

The diffusivity ratio, λ, will increase with weight loss due to the increase in open porosity. DIFFUSE 6 incorporates several options whereby λ is allowed to vary either linearly or quadratically with either weight loss or dose. The variation can also be controlled by use of threshold values below which a linear variation is obtained and above which a quadratic variation is obtained.

2.5.3 Porous Flow

When graphite is subjected to a pressure gradient, ∇P, gas will permeate through the graphite pores (porous flow) in accordance with Darcy's equation:

$$v = \frac{B_o}{\mu} \nabla P \qquad (19)$$

where: v = Velocity vector for CO_2 flow through porous graphite (see equations 14 to 16)

B_o/μ = Permeability coefficient for virgin graphite, cm^2/atmos, s.

Under impressed flow, the pressure profile under steady state conditions is determined from continuity (conservation of mass) considerations using the equation

$$\nabla(\rho v) = 0$$

$$ie \quad \nabla\left(\frac{P}{RT}\right)\left(\frac{B_o}{\mu}\nabla P\right) = 0$$

where: R = Universal gas constant.

which may be written:

$$A^{\bullet}.\nabla\,(P.\nabla P) = 0 \text{ where } A^{\bullet} = \left(\frac{B_o}{\mu}\right)\left(\frac{1}{RT}\right)$$

or

$$or \quad K.\nabla^2\,(P^2) = 0 \text{ where } K = \frac{A^{\bullet}}{2}$$

The finite element method is used to calculate the pressure profile which is then used to calculate v during the gas concentration calculation which is in turn fed into equations 14, 15 and 16.

In DIFFUSE 6 the graphite permeability coefficient may be calculated using options which allow B_o/μ to vary either linearly or quadratically with either weight loss or dose. The variation can also be controlled by the use of threshold values below which a linear variation is obtained and above which a quadratic variation is obtained.

2.5.4 Methane Destruction, K_1

Methane is destroyed by radiolysis at a rate which is proportional to the local values of dose rate, open pore volume and $G(-CH_4)$ value, the latter being known as the methane destruction rate parameter and is defined as the number of molecules of methane destroyed per HeV (HeV = 100 eV) of energy absorbed by the CO_2 in the graphite open pores. The destruction

of methane gives rise to the formation of carbon monoxide and water in accordance with the equation:

$$CH_4 + 3\,CO_2 \rightarrow 4\,CO + 2\,H_2O$$

This equation defines the normally accepted values of the stoichiometry for H_2O formation from CH_4 destruction (STOX = 2), and for CO formation from CH_4 destruction (STOX1 = 4), used in equations 15 and 16.

The sink term for methane destruction, K_1, in equations 14 to 16 is defined as:

$$K_1 = B_2.M.W(p).V(p).G(-CH_4) \times 10^6 \qquad (20)$$

where:

B_2 = Physical constant (= 1.036 x 10^{-7}) HeV Mole/J Molecule

M = Molecular weight of CO_2

W(p) = Dose rate to graphite at mesh position (p) watts/g

V(p) = Total open pore volume at mesh position (p) cm^3/cm^3

$G(-CH_4)$ = Number of methane molecules destroyed per 100eV of energy absorbed by CO_2 contained within the graphite pores.

$G(-CH_4)$ is a complex function of the methane, carbon monoxide and moisture concentrations, and temperature. The recommended expression is:

$$G(-CH4) = \frac{2.2}{1 + \frac{[CO]}{[CH_4]}.\exp\left(\frac{4900}{R_cT}\right).\{k5 + k6.\frac{[H_2O]}{[CO]}\}} \qquad (21)$$

where:

$[CH_4]$, [CO] and $[H_2O]$ are the concentrations of methane, carbon monoxide and moisture, respectively, vpm.

R_c = Gas constant (= 1.9869) cals/°C Mole

T = Temperature, °K

k_5 and k_6 are constants (k_5 = 0.00208, k_6 = 0.0868)

K_1 (equation 20) is then used as a nodal load vector in the finite element formations.

In DIFFUSE 6 the total open pore volume is assumed to vary with weight loss according to

the relationship:

$$V(p) = V_o + \hat{x}(p)\ (1-V_o)$$

where: V_o = Initial total open pore volume, cm^3/cm^3

$\hat{x}(p)$ = Mean weight loss at a point over the current time increment, %.

The dose rate variation with weight loss is defined in Section 2.5.6.

2.5.5 Graphite Oxidation, K_2

Carbon monoxide is also produced from graphite oxidation in accordance with the equation:

$$C + CO_2 \rightarrow 2CO$$

Again, this equation defines the normally accepted value of the stoichiometry for carbon monoxide formation from graphite oxidation (STOX2 = 2) used in equation 16.

The source term for the production of CO from graphite oxidation , K_2, is defined as:

$$K_2 = B_2.M.W(p).V_o.AR_o.\frac{B_1.\rho_s}{V_s}.f_i(p) \times 10^6 \qquad (22)$$

From a comparison with equation 20, it may be seen that:

$$K_2 = B_2.M.W(p).V(p).G(-c)$$

$$where \quad G(-c) = AR_o.\frac{B_1\rho_s}{Vs}$$

$$and \quad V(p) = V_o f_i(p)$$

AR_o = Initial graphite attack rate at 674K and 41 bar for the coolant composition at mesh point (p), g/g.h. $^{mW}/g$.

B_1 = Constant for DIDO rig (= 0.069302 x 10^8 when rig temperature and pressure are 673K and 41 bar, respectively)

ρ_s = Graphite density in DIDO rig specimens (= 1.8) g/cm^3

V_s = Open pore volume in DIDO rig specimens (= 0.121) cm^3/cm^3

V_o = Initial total open pore volume, cm^3/cm$_3$

$f_i(p)$ = Factorial increase in rate of weight loss due to all relevant factors at mesh position (p) , as defined in Section 2.5.7.

The graphite attack rate parameter is a function of methane and carbon monoxide concentration which may change with respect to time. The recommended values of AR_o for Gilsocarbon graphite at 400°C and 41 bar are given in Table 3.1 and illustrated in Fig 3.10.

2.5.6 Dose Rate Variation

In order to include as much flexibility into DIFFUSE 6 as possible, several options are included to allow for increases in local dose rate as a function of mean brick weight loss at any given time. The dose rate, W, at any position in the brick cross-section is thus assumed (at time zero) to be governed by the equation:

$$W = \bar{W} [\mu' + \Delta + \nu'.g] \, d(r) \qquad (23)$$

where:

W = Mean local dose rate to graphite, watts/g

μ' = Constant fraction of dose rate

Δ = Incremental fraction of dose rate which may vary with time

$\upsilon'.g$ = Fraction of dose rate associated with moderator/fuel ratio, g

d(r) = Dose rate factor in brick

Increases in dose rate due to weight loss are assumed to occur in the ratio:

$$\textit{Factorial increase in dose rate} = \frac{1}{(1 - \frac{\bar{x}}{100})}$$

where:

$\bar{x}$ = mean section weight loss, %

The options available in DIFFUSE 6 for increase in dose rate due to radiolytic weight loss are:

$$W = \bar{W}\left[\frac{\mu' + \Delta}{\left(1 - \frac{\bar{x}}{100}\right)} + \nu.'g\right] d(r)$$

$$W = \bar{W}\left[\mu' + \Delta + \nu.'g\right]\frac{d(r)}{\left(1 - \frac{\bar{x}}{100}\right)}$$

$$W = \bar{W}\left[\mu' + \Delta + \nu.'g\right] d(r)$$

The latter equation represents no effect of weight loss on dose rate.

2.5.7 Reactive Pore Volume (RPV) Model

The RPV model is based on the theory that radiolytic oxidation in inhibited coolant is concentrated within a small fraction of the total open pore volume known as the reactive pore volume. The oxidation rate within the RPV is a function of gas composition, and the rate of graphite weight loss is assumed to increase proportionately with increase in RPV. Although the RPV model can be specified in terms of several pore groups in which each group is characterised by its pore entrance diameter (PED) or pore entrance width (PEW), DIFFUSE 6 is limited to a single pore group.

For RPV calculations, the initial RPV at a given mesh point p, $RPV'_o(p)$, assumed to be directly proportional to the initial radiolytic oxidation rate:

$$RPV'_o(p) = OPV_o.\frac{AR_o}{AR_s}$$

Experiments have shown that for a standard initial graphite attack rate, ARs, in the DIDO rig of 0.2×10^{-3} g/g.h.mW/g at 41 bar and 673K, the initial RPV value, OPV_o, for a single pore group is 0.03 cm^3/cm^3. AR_o is the initial graphite attack rate at 41 bar and 673K for the coolant in question (from Table 3.1 and Fig 3.10).

It should, however, be noted that DIFFUSE 6 has the option of performing a Strandring type calculation for which

$$RPV'_o(p) = OPV_o$$

High weight loss experiments in inhibited coolant have shown that the graphite oxidation rate does not go on increasing expontentially as predicted by the Standring relationship for PGA

radiolytically oxidised in CO_2. The results indicated that the rate (and by implication RPV) increased with weight loss by about a factor of 3 after which there was no further increase in attack rate, ie RPV had saturated at 3 times the initial value, as may be seen in Fig 3.11. This rule has been assumed to apply regardless of initial RPV, and the calculation routines therefore incorporate a pore efficiency factor, F, to adjust RPV in accordance with one of the following relationship

RPV(p) = RPV' (p).F(PED) for cylindrical pores
RPV(p) = RPV' (p).F(PEW) for slab-shaped pores

where F(PED) and F(PEW) define the reactive pore efficiency factor versus pore entrance diameter or width. Tables are available giving values of efficiency factor to give saturation of RPV following oxidation to 3 times the initial RPV.

The initial rate of graphite oxidation at mesh point (p) is given by:

$$Rate_o(p) = 9.92076 \cdot 10^8 \, AR_o(p) \, \frac{P}{T} \, W_o(p) \quad \% \text{ per year} \qquad (24)$$

where the numerical constant is obtained from:

$$\frac{100}{P_s \cdot 14.504} \, T_s \cdot 24 \cdot 365.25 \cdot 10^3$$

with P_s = Pressure in experimental rig (41 bar)

T_s = Temperature in experimental rig (673K)

$AR_o(p)$ = Initial graphite attack rate at 41 bar and 673K for the coolant composition at mesh position (p), g/g.h.mW/g.

P and T are pressure, psia, and temperature T, K, at position (p)

$W_o(p)$ = Initial energy deposition dose rate at position (p), W/g.

Having defined the initial rate of graphite oxidation, $Rate_o(p)$, in equation 24, the weight loss in the i_{th} interval of time $\Delta x_i(p)$ is given by:

$$\Delta x_i(p) = Rate_o(p).fi(p)dt$$
$$x\ i(p) = x_{i-1}(p) + \Delta x_i(p)$$

where fi(p) is the mean factorial increase in rate of weight loss over the i_{th} time increment and is defined as:

$$f_i = \left(\frac{RPV_i}{RPV_o}\right) \cdot \left(\frac{W_i}{W_o}\right) \cdot \left(\frac{AR_i}{AR_o}\right) \qquad (25)$$

where: $\left(\frac{RPV}{RPV_o} \right)$ = Mean factorial increase in RPV averaged over the ith time increment (including an allowance for pore efficiency changes).

$\left(\frac{W}{W_o} \right)$ = Mean factorial increase in dose rate averaged over the ith time interval (including allowance for weight loss effects)

$\left(\frac{AR}{AR_o} \right)$ = Mean factorial change in initial attack rate averaged over the ith time increment due to changes in coolant composition.

Appropriate techniques are included in DIFFUSE 6 to ensure correct integration of weight loss in each time step.

RPV is assumed to increase with loss of graphite at crystal density, ie no allowance is made for opening up of closed porosity, hence:

$$RPV_i\,(p) = RPV_o + \frac{\rho_{B_o}}{\rho_c} \cdot \frac{x_i(p)}{100}$$

However, an option is available for allowing reductions in RPV due to fast neutron pore closure:

$$RPV_i\,(p) = RPV_o + \frac{\rho_{B_o}}{\rho_c} \cdot \frac{x_i(p)}{100} - closure$$

Summarising, the essential steps in DIFFUSE 6 are as follows:

For each time step calculate:

i. Diffusion and permeability coefficients updated to allow for the effects of weight loss.

ii. New pressure profile in brick section.

iii. Factorial increase in dose rate due to weight loss.

iv. Gas composition distribution.

v. Initial graphite attack rate at each mesh point corresponding to new coolant gas composition distribution.

vi. Factorial changes in initial graphite attack rate (since startup) due to changes in coolant gas composition.

vii. Factorial increases in RPV due to weight loss.

viii. Overall factorial increase in the rate of graphite weight loss due to changes in dose rate, gas composition and RPV.

ix. Total weight loss at each mesh point by appropriate integration of the weight loss in each time step.

3. Effect of Radiolytic Oxidation on the Physical and Mechanical Properties of Graphite

Experimental data on PGA graphite radiolytically oxidised in nominally pure CO_2, and on AGR moderator and fuel sleeve graphite radiolytically oxidised in methane-inhibited coolants, has indicated that the thermal conductivity, Young's modulus and strength changes due to oxidation alone were changed by an exponential factor e^{ax}, where x is the fractional weight loss and a is a constant which is dependent upon both graphite type and property change. The following table compares values of the constant a for three property changes of three types of graphite.

Property Change	Gilsocarbon Moderator Graphite (inhibited coolants)	AGR Fuel Sleeve Graphite (inhibited coolants)	PGA Graphite (Nominal Pure CO_2)
Thermal Resistivity $\left[\frac{K_o}{K}\right]_{ox}$	+2.7	+2.3	+3.1
Young's Modulus $\left[\frac{E}{E_o}\right]_{ox}$	-3.4	-3.4	-4.8
Strength $\left[\frac{\sigma}{\sigma_o}\right]_{ox}$	-3.7	-3.9	-5.2

In the above table K_o, E_o and σ_o are unirradiated values, whereas K, E and σ are oxidised values of the properties.

Radiolytic weight loss should be assumed to have no effect on the coefficient of thermal expansion of graphite.

Studies of the effect of radiolytic oxidation on dimensional changes of graphite indicate no effect before the onset of shrinkage reversal (ie turnaround). However, the onset of shrinkage reversal was shown to be increasingly delayed with increase in weight loss. The effect is only relevant for Gilsocarbon graphite in AGRs. The rules for calculating the effect on dimensional changes of radiolytical weight loss inhibited coolants are detailed in the notes for Lecture 2.

References

1. Standring J. Calculation of the graphite weight-loss in Civil Magnox and Advanced Gas-cooled Reactors. Journal of Nuclear Energy, Parts A and B, 1966, Vol 20 pp201 to 217.

2. Russell P D D. A user's guide to the APC graphite weight loss computer code DIFFUSE 4. 1979. APC/R 1514

3. Davies M A. A theory manual for DIFFUSE 6. 1991. AEA-RS-5117.

APPENDIX 3.1

ENERGY DEPOSITION IN GRAPHITE

During the maintenance of the chain reaction in a reactor, energy is deposited in the moderator because of the following neutron cycle.

Fast neutrons due to fission in the fuel escape from the fuel after some small energy loss due to inelastic scattering. During the inelastic scattering process small fractions of energy escape from the fuel in the form of gamma radiation. The fast neutrons escaping from the fuel will be elastically scattered in the moderator, losing energy to the moderator in the process. The choice of the graphite pitch is such that a much degraded fission neutron spectrum diffuses back to the fuel. This spectrum predominates in neutrons having thermal energies.

A small fraction of the thermal neutrons are captured by moderator atoms, producing gammas; a larger fraction are captured by canning materials, releasing high-energy gamma rays; the majority of the thermal neutrons, however, induce fission in the fuel, producing prompt fission and fission product decay gammas in addition to high-energy fission fragments, fast neutrons, betas, etc.

Some of the neutron spectrum diffusing back into the fuel will be in the energy band in which resonance capture occurs in the fuel; high-energy gamma rays will be produced by neutron capture. Some of the high-energy neutrons returning to the fuel will produce fast fission in the fuel, resulting in further fast neutrons and gammas.

To sum up, the energy deposition in the graphite is due to slowing down of fast neutrons and gamma rays (prompt fission, capture, fission product decay and inelastic scattering) arising in the fuel plus a small amount due to capture gammas arising in graphite. The components of the heating due to capture gammas and the majority of the prompt fission and fission product decay gammas will be proportional to the thermal neutron flux in the channel. The components of the heating due to slowing down of fast neutrons and inelastic scattering gammas will be proportional to the fast neutron flux.

Attack Rate Parameter for RPV Model gm/gm per hr per mW/gm x 10**8							
	Carbon Monoxide						
Methane	2500	5000	75000	10000	15000	20000	25000
0.0	0.822	0.641	0.505	0.411	0.312	0.270	0.247
25.0	0.656	0.548	0.442	0.366	0.286	0.253	0.235
50.0	0.526	0.470	0.388	0.327	0.263	0.237	0.224
75.0	0.423	0.404	0.341	0.293	0.241	0.222	0.214
100.0	0.343	0.348	0.301	0.262	0.222	0.209	0.204
125.0	0.280	0.301	0.267	0.236	0.205	0.196	0.194
150.0	0.230	0.262	0.237	0.213	0.190	0.185	0.186
175.0	0.192	0.228	0.211	0.193	0.176	0.174	0.178
200.0	0.161	0.200	0.189	0.175	0.164	0.164	0.170
225.0	0.137	0.177	0.170	0.160	0.152	0.155	0.163
250.0	0.118	0.157	0.153	0.146	0.142	0.147	0.156
275.0	0.104	0.140	0.139	0.134	0.133	0.140	0.150
300.0	0.092	0.126	0.127	0.124	0.125	0.132	0.144
325.0	0.083	0.114	0.116	0.114	0.117	0.126	0.138
350.0	0.076	0.104	0.107	0.106	0.111	0.120	0.133

Table 3.1 - Attack Rate Parameter as a Function of Methane and Carbon Monoxide Concentration for Gilsocarbon Graphite at 400 degrees C and 41 bar

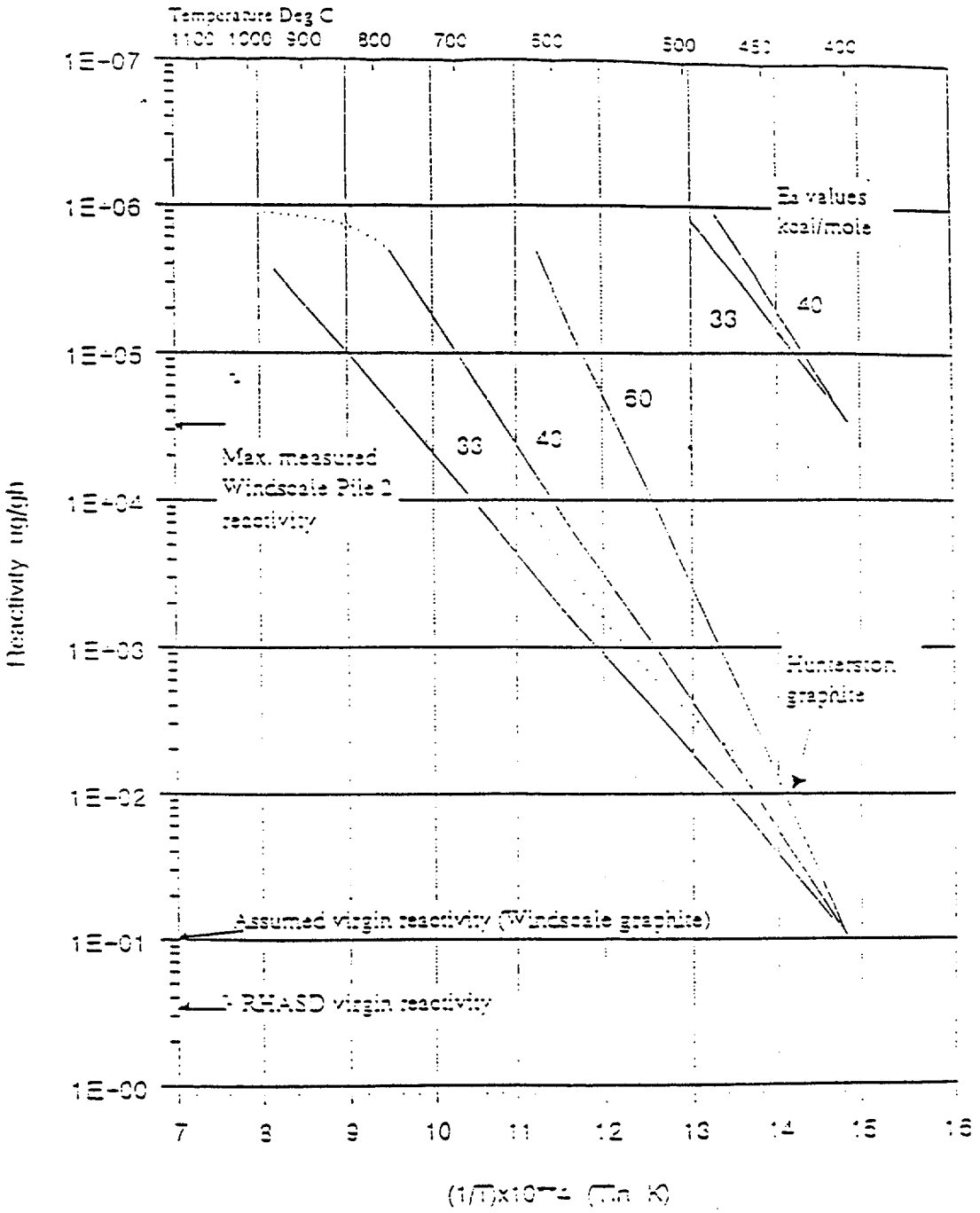

Figure 1. Arrhenius Diagram: Plots of Graphite Air reactivity

VARIATION OF R(θ) WITH CALDER EQUIVALENT TEMPERATURE

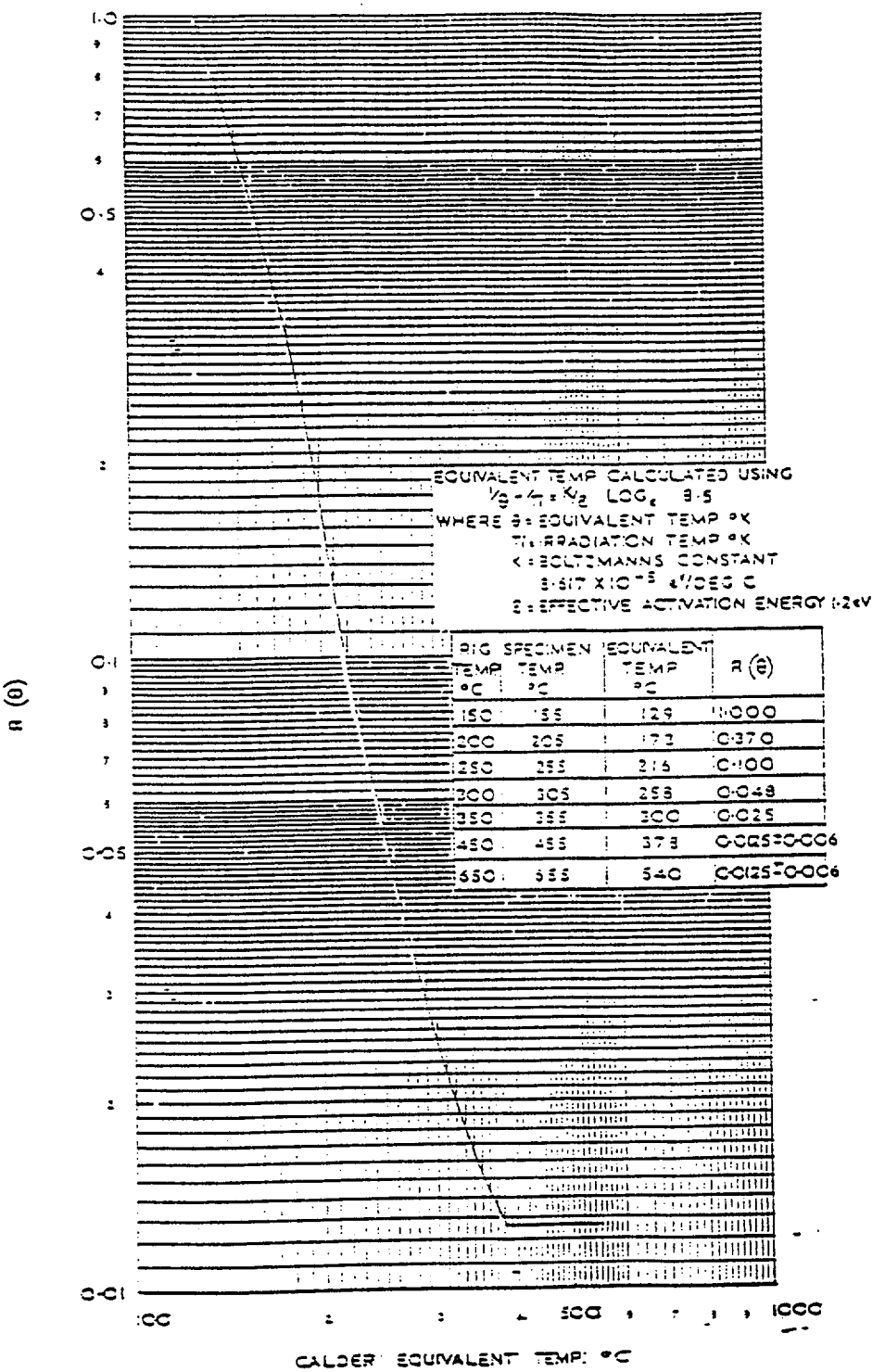

Figure 2.

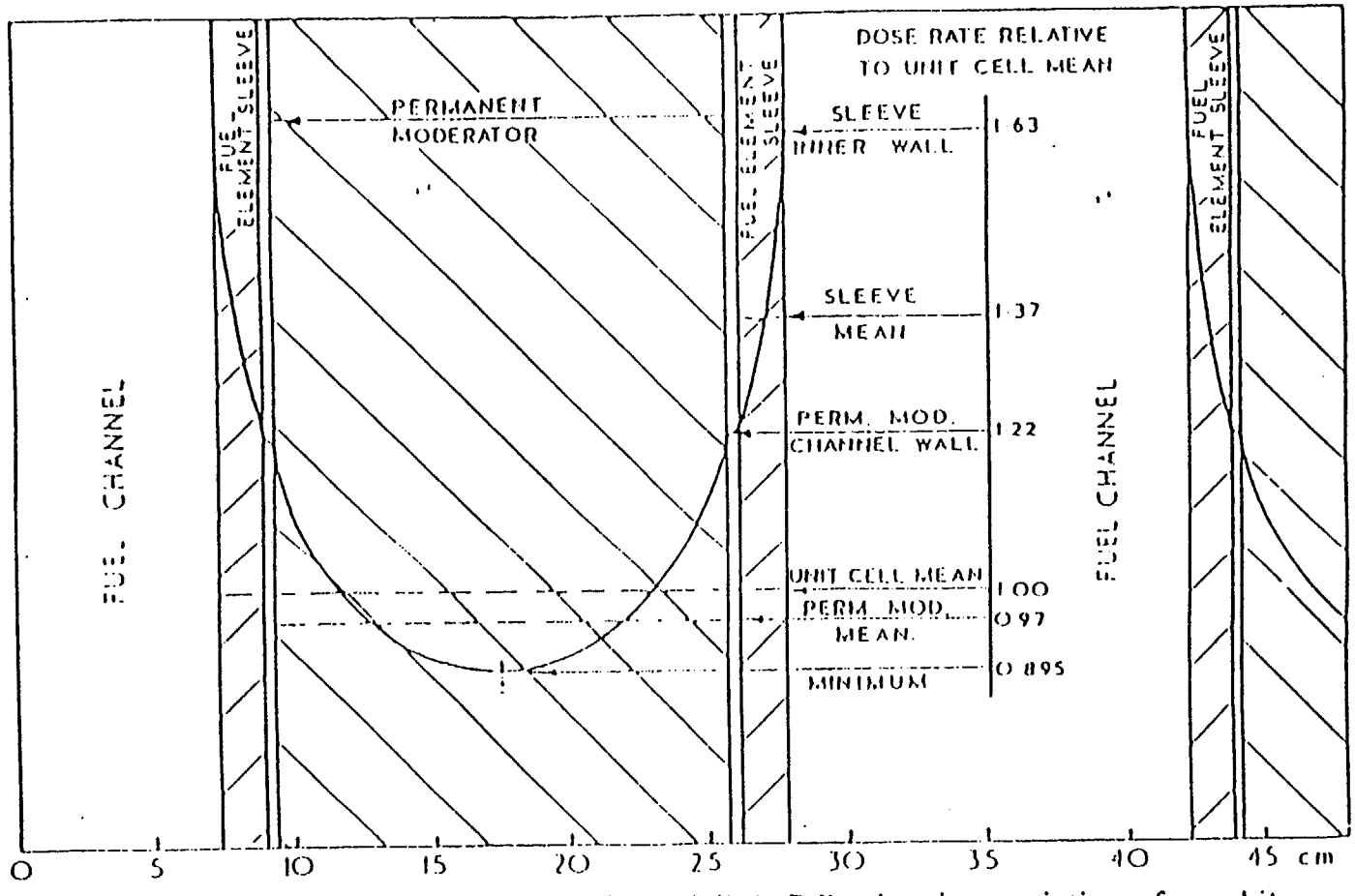

Figure 3. Section through core of typical Civil A.G.R. showing variation of graphite dose rate within a unit cell.

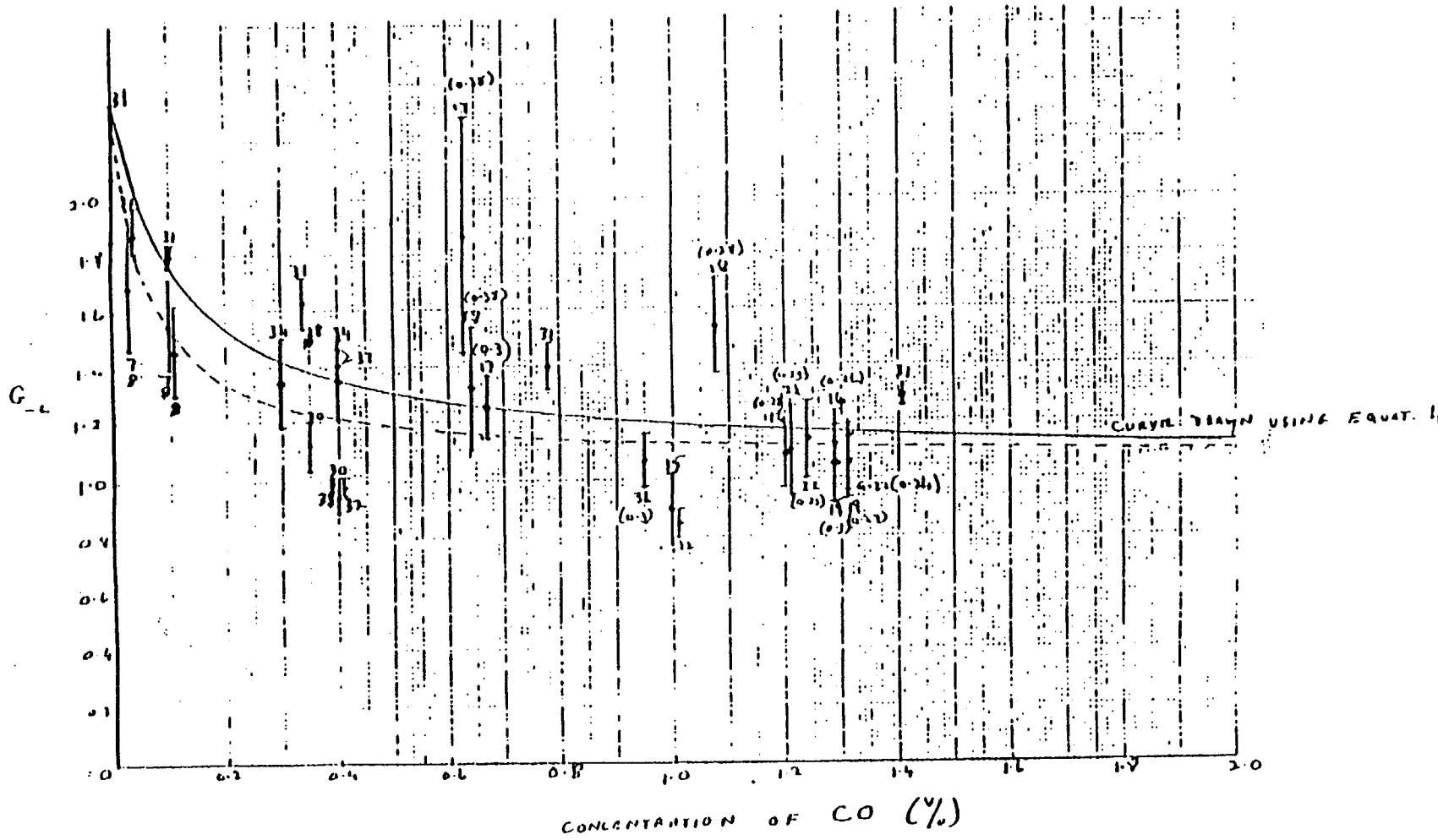

Figure 4. Variation of G_c with CO Concentration

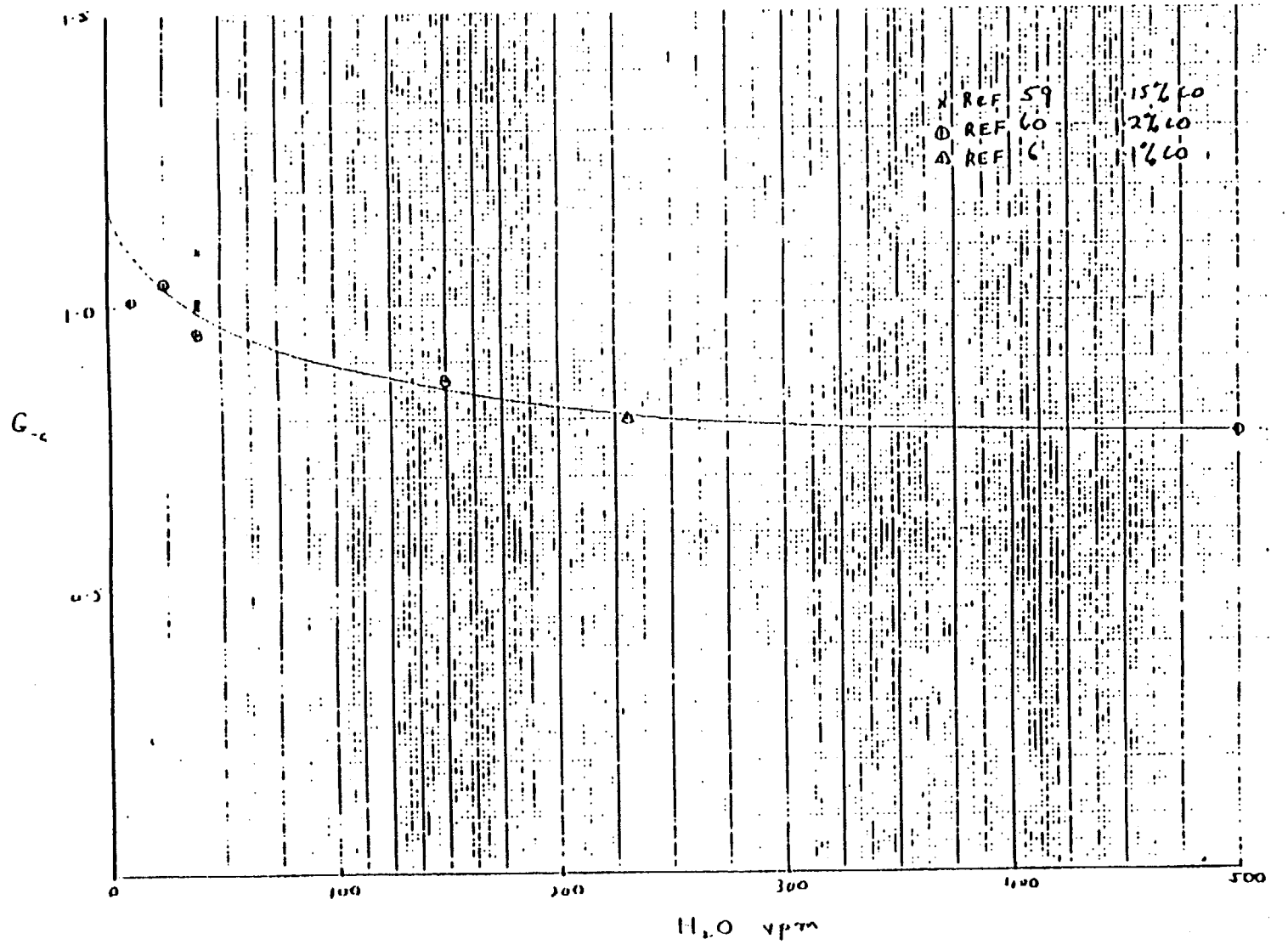

Figure 5. Variation of G_c with Moisture in a Normal 1.2% CO/CO_2 Mixture

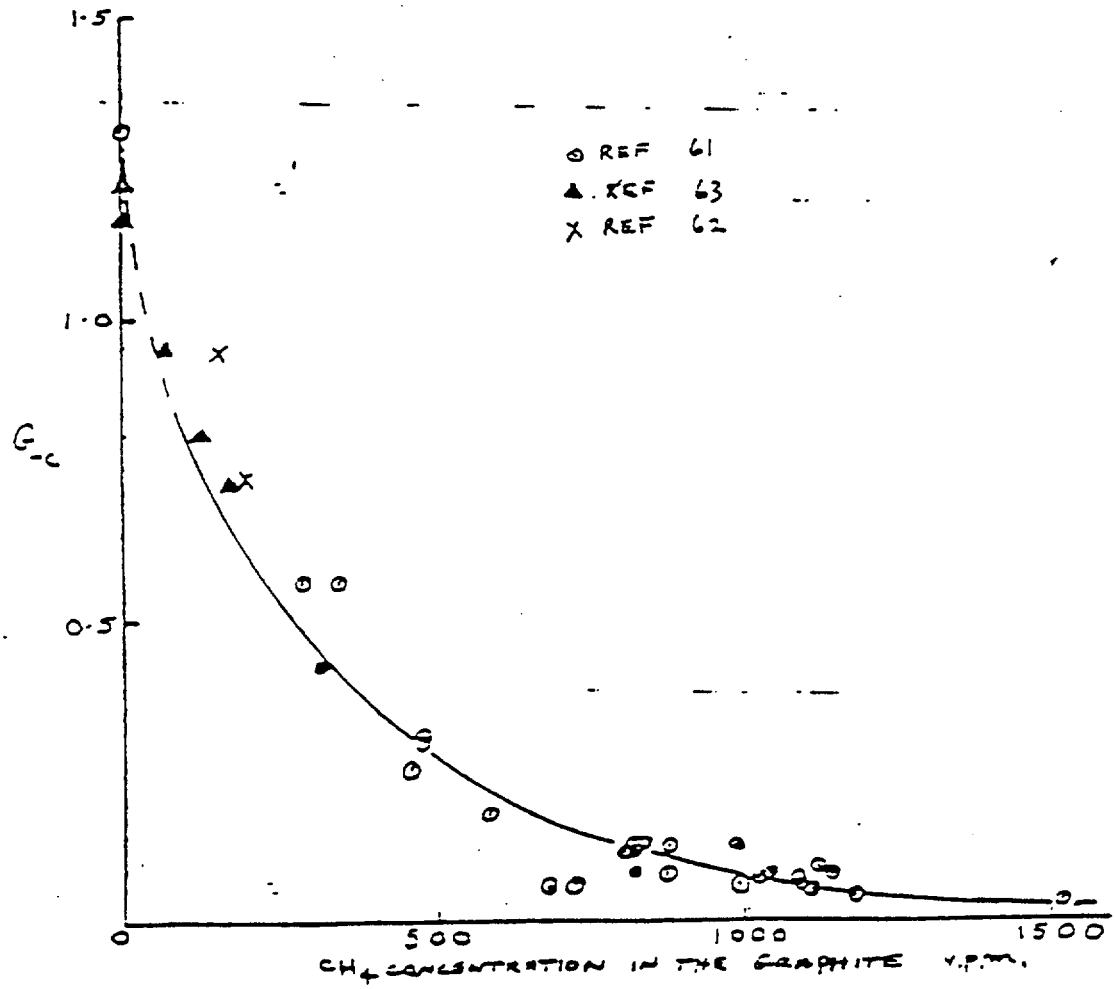

Figure 6. The Effect of CH_4 Concentration on G_c for Mixtures Containing 1.0 - 1.5% CO

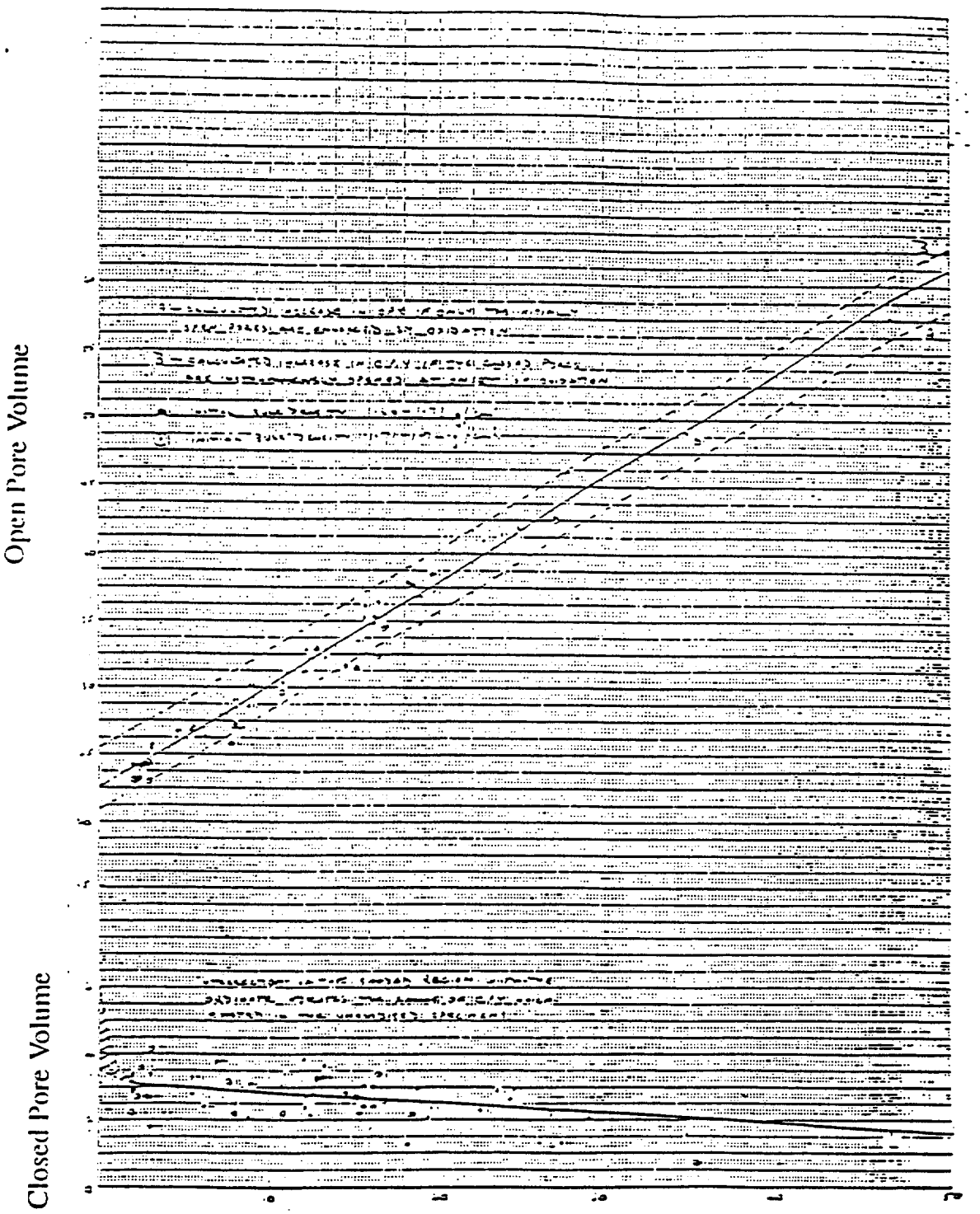

Figure 7. The Effect of In - Pile Weight Loss on the Porosity of PGA Graphite

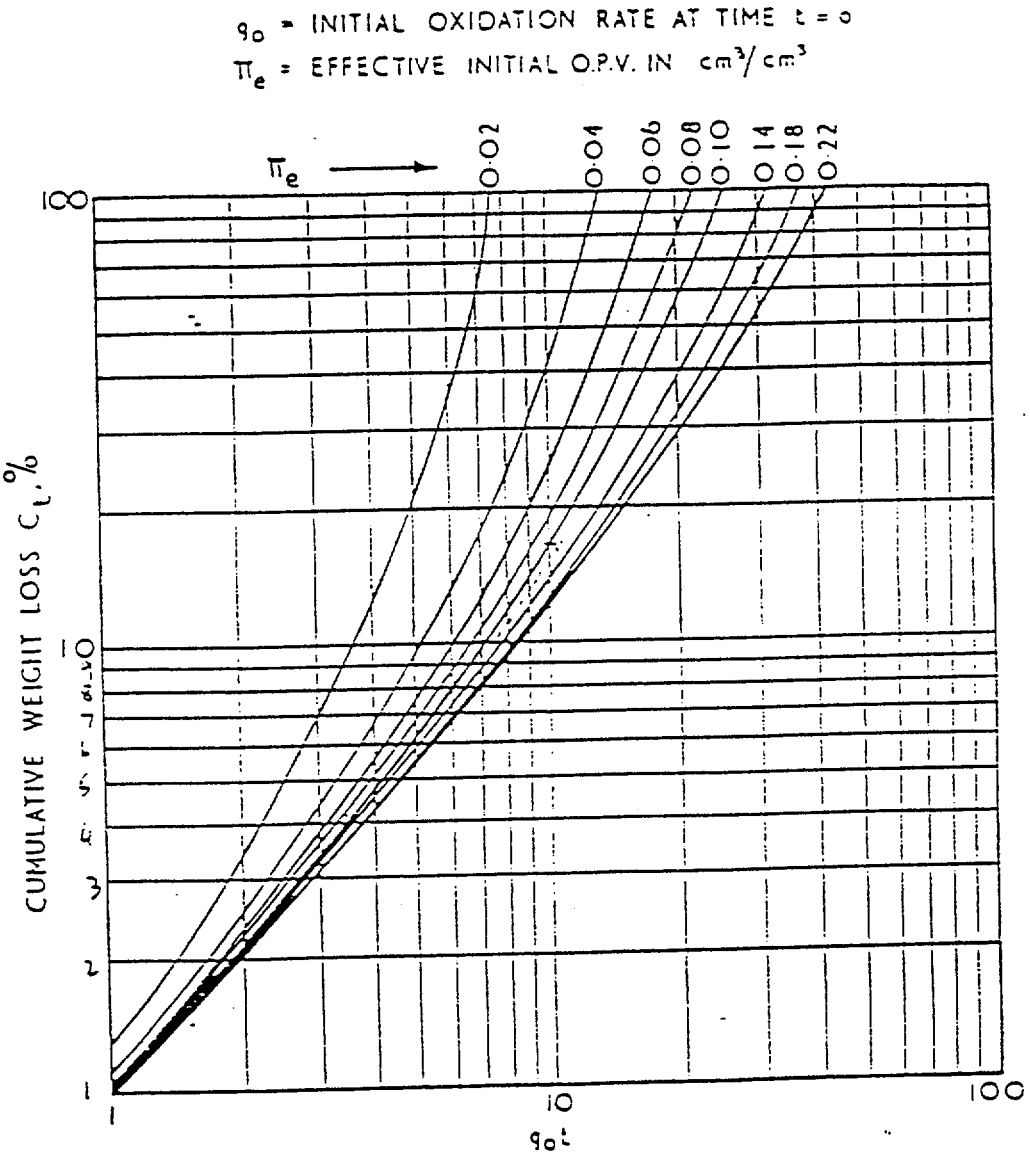

Figure 8. Effect of Increase in Porosity on Cumulative Weight Loss when Dose Rate to Gas is Constant

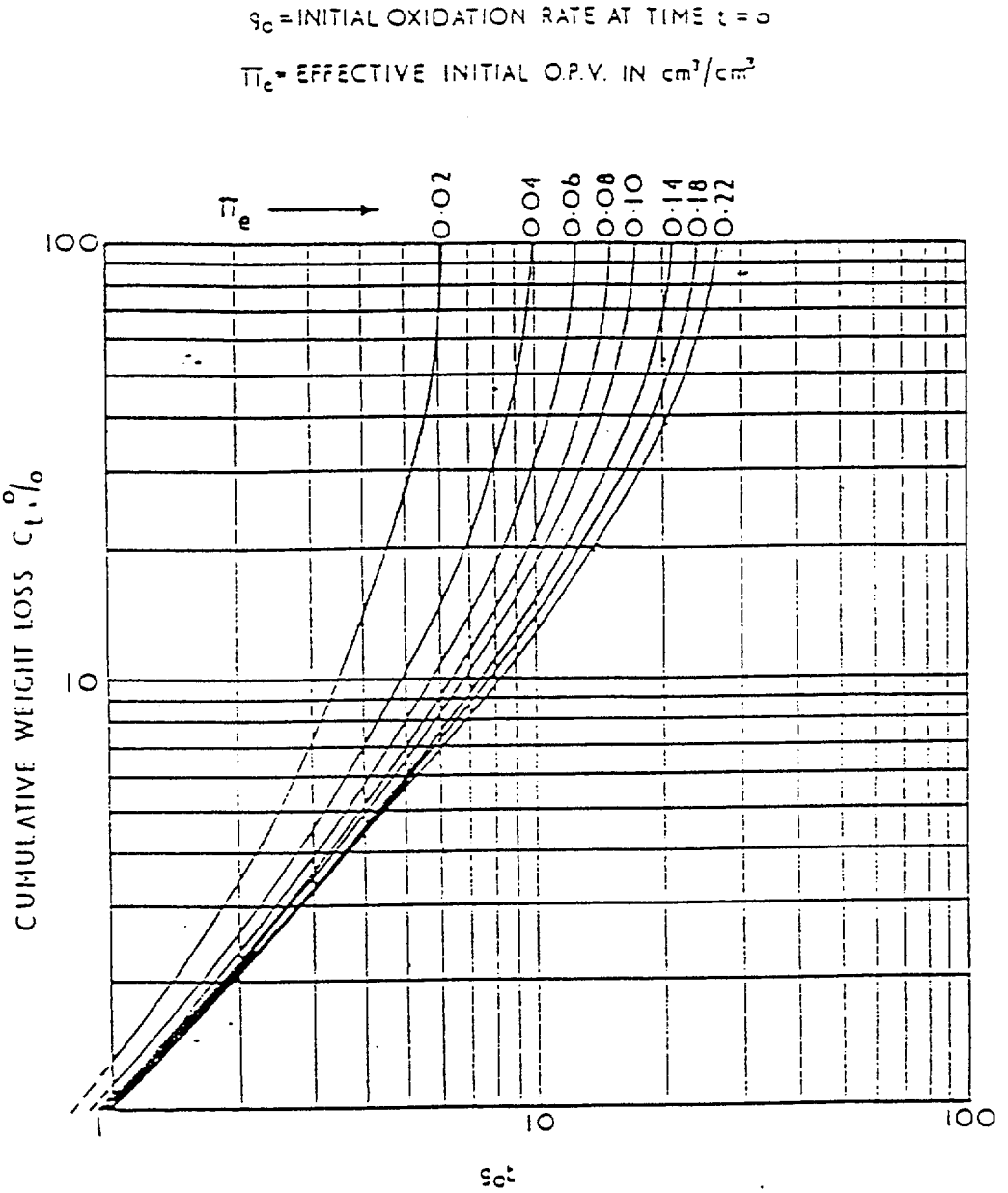

Figure 9. Effect of Increase in Porosity on Cumulative Weight Loss for a Reactor Operated at Constant Power

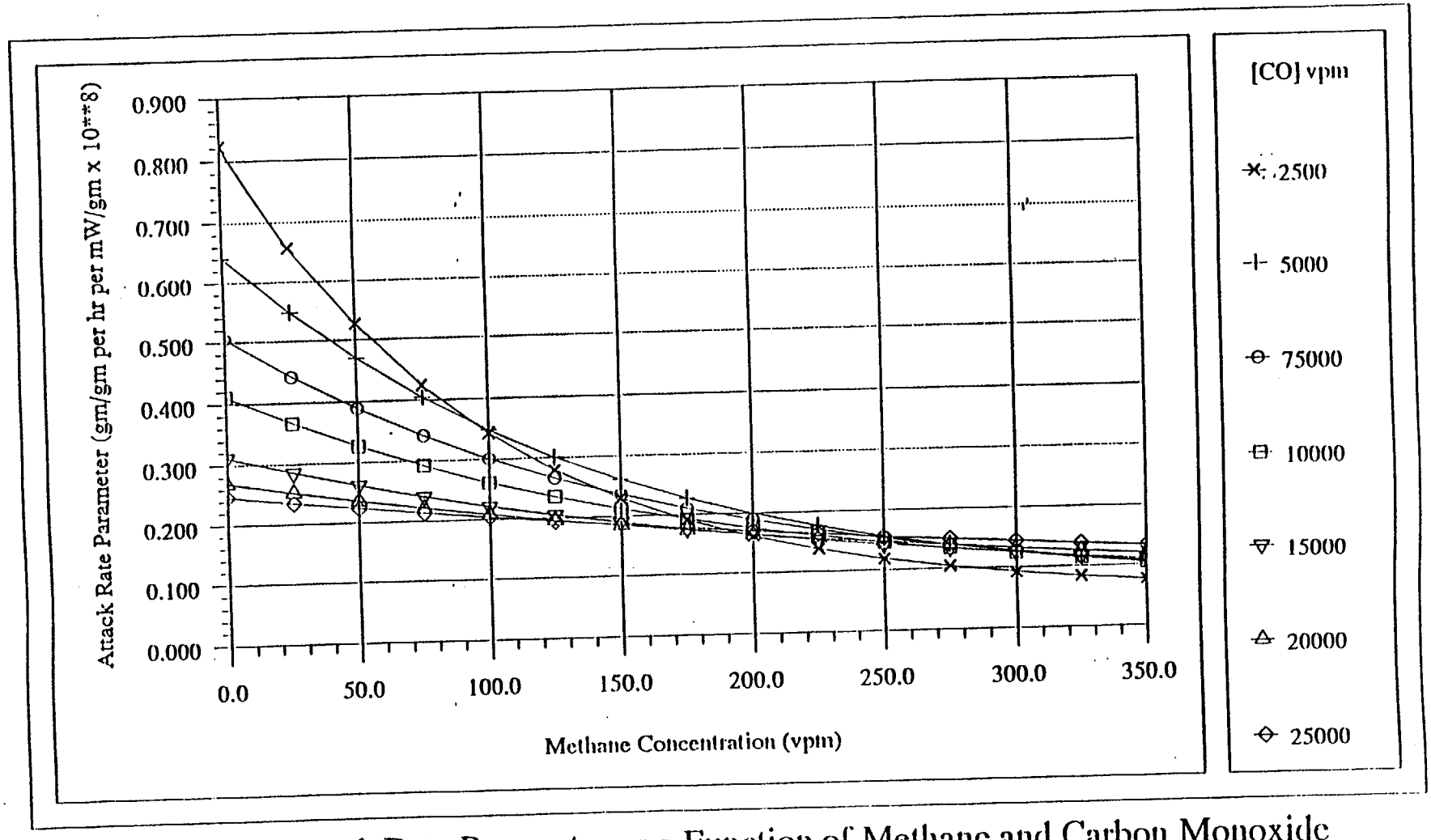

Figure 10. Attack Rate Parameter as a Function of Methane and Carbon Monoxide Concentration for Gilsocarbon Graphite at 400 degrees C and 41 bar

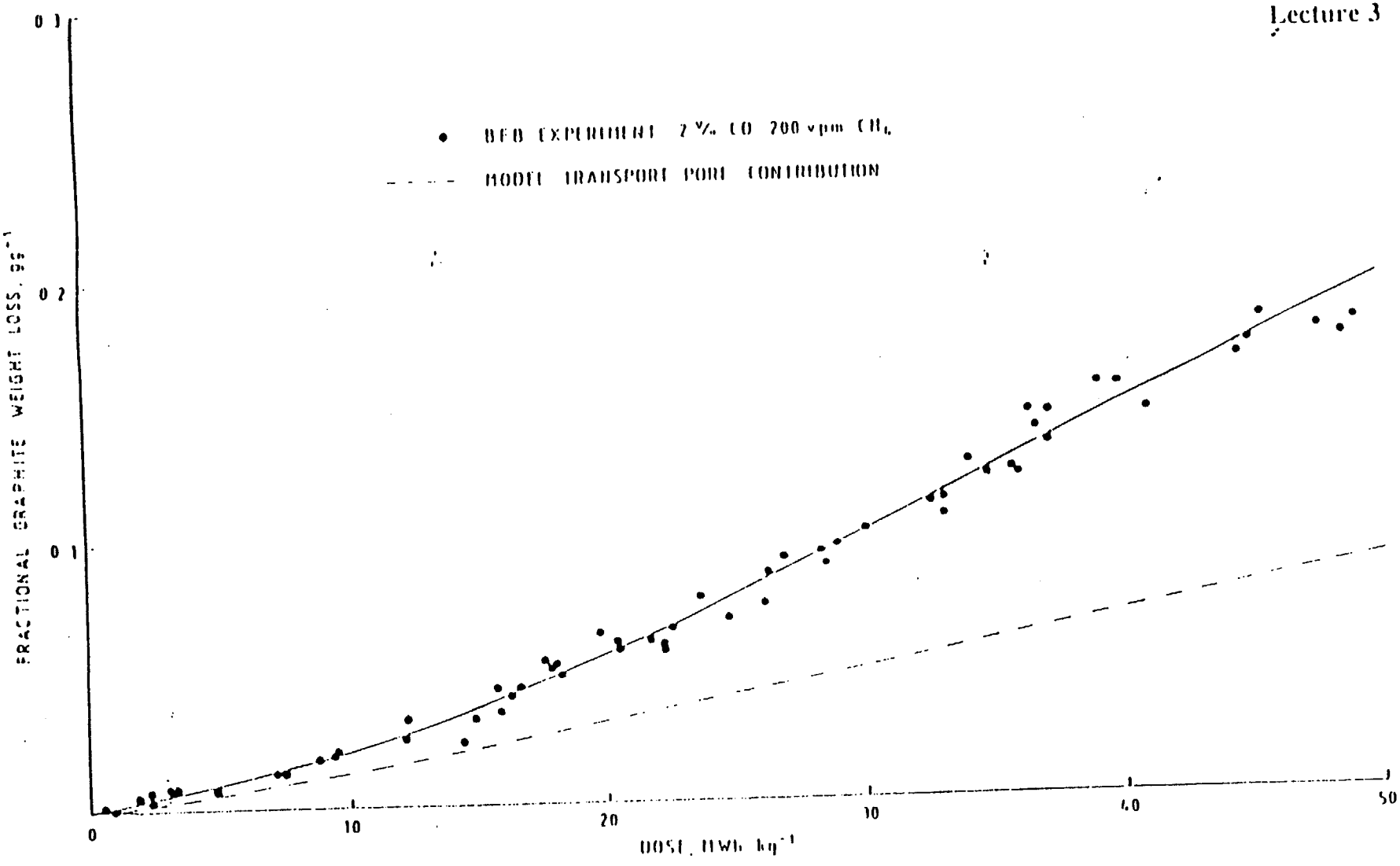

Figure 11. EXPERIMENTAL WEIGHT LOSS DATA FOR 0.02% CH_4/2% CO COOLANT AND CALCULATED TRANSPORT PORE CONTRIBUTION

GRAPHITE TECHNOLOGY COURSE

LECTURE 4

1. Moderator Structure Design in the UK

The early designs of moderator structure in the UK such as BEPO and the Windscale Piles operated at atmospheric pressure and, using air as coolant, rejected the heat produced in the uranium fuel through a tall chimney. Thus the problem was one of shielding with overriding need for preservation of fuel and control rod alignment. Operational difficulties included the need to limit the build-up of stored energy in the graphite by regular annealing.

With the higher power densities necessary for economic electric power production came the need for high pressure containment, increased coolant flows and significantly higher operating temperatures. The more severe operating conditions under which the graphite was required to operate necessitated major changes in moderator design aimed at mitigating against the dimensional and physical property changes suffered by the graphite under the combined effects of fast neutron damage and radiolytic oxidation in the CO_2 coolant. These requirements intensified with the arrival of the Advanced Gas-cooled Reactors when not only improved designs, but also improved graphite became necessary.

The following sections of this lecture trace the history of graphite structures used in the UK power reactors from Calder Hall onwards, outlining the development of moderator structure designs adopted to generate electricity safety and efficiently for the full design lifetime of the reactor.[1]

2. The Calder Moderator Structure

When the graphite moderator structure for the Calder hall reactors was designed, it was erroneously believed that fast neutron irradiation caused the graphite to grow in both the perpendicular and parallel directions to the extrusion axis of the bricks, and that the ratio of these growth rates was respectively about 6:1. In plan view the structure was to be a regular 24-sided polygon, 1100cm across corners by 800 cm high, with the fuel elements placed in 1696 vertical channels 10.6 cm diameter spaced on a square 20 cm lattice pitch. The predicted growth rates were such that if the core had been constructed as a solid structure comprising bricks 20 cm square by 80 cm high with their extrusion axes placed vertically, the diameter would have increased during irradiation by a maximum of about 16 cm and the height by a maximum of about 3 cm. The structure would have come barrel-shaped and resulted in unacceptable inter-channel leakage due to the tilting of bricks, and caused difficulties in inserting and removing control rods and fuel elements due to the distortion of channels.

These difficulties were overcome by adopting the form of construction shown in Figures 4.1 and 4.2 in which the core comprised layers of bricks slightly smaller than 20 cm square having their extrusion axes placed vertically, interleaved with two layers of rectangular tiles having their extrusion axes placed horizontally and parallel with the long sides. It was argued that if all the tiles in the bottom layer were arranged with their long sides running

North to South forming parallel chords across the core face, and those in the top layer were arranged with their long sides running East to West, and garter restraints were placed around the periphery of the tile layers, the bricks would be located in their correct lattice position with a gap around their four vertical sides. Displacement of the channels during irradiation would thus occur at the lower axial rate.

With this arrangement, however, the tiles become oval during irradiation and this would have caused them to interfere with fuel handling operations and made spigot location between bricks and tiles impracticable. To obviate these difficulties the tile bore was made slightly larger than the brick bore, and the bricks and tiles were located relative to one another by means of the cruciform keys shown in Figure 4.2. In addition, to minimise neutron streaming through the Wigner gaps, the bricks were rotated by 2° about their vertical axes relative to the lattice centre lines, each layer being twisted in a direction relative to those immediately above the below it. Control rod holes were formed by machining quadrant fillets on the long edges of four abutting bricks.

The peripheral reflector was built solidly, ie without Wigner gaps as the growth in this region was estimated to be negligible. Small gaps were, however, provided in the inner portions of the upper and lower reflectors, and the tile layers at the top and bottom of the core were made single tiles of much greater thickness than those in the intermediate layers. Circumferential garter restraints situated at each of the eleven tile layers were used to provide the necessary radial forces to hold the core structure together, and these restraints were suitably designed to accommodate the large tangential strains imposed upon them and to expand and contract thermally at the same rate as the graphite reflector.

The core structure was supported on a diagrid over which a layer of abutting steel support plates was laid. Differential thermal expansion between the steel support system and the graphite structure was accommodated by supporting each column of bricks on a ball-bearing having flat tracks. Location of the core structure relative to the diagrid was effected by means of radial keys attached to the bottom circumferential restraint engaging in keyways on the upper surface of the diagrid, and by spigotting the bottom bricks of the centre four columns into the core support plate.

Steel castings, generally referred to as charge pans, were placed on the top surface of the graphite structure to form a robust funnel portion at the top of the coolant channel and hence facilitate fuel charging operations. The charge pans similarly guided the control rods, provided location for the bottom end of the charge chute, were a convenient point to attach burst cartridge detection piping and provide ballast to hold down the top reflector bricks. Although a separate charge pan could have been provided for each coolant channel, it was found most convenient to serve 16 channels with one charge pan.

3. Civil Magnox Reactor Designs

The basic features of the Calder reactors were retained throughout the civil programme in particular the use of stacked columns of graphite bricks forming vertical fuel channels. Channel lattice pitching remained within the limits 19 - 20 cm with 9 - 10 cm diameter fuel channels utilising bricks approximately 80 cm high. Table 4.1 sets down the leading design particulars for each reactor in chronological order of building. The significant increase in

fuel channel numbers between Calder and the first two civil reactors will be noted. A further large increase in both fuel channels and output was achieved at Wylfa taking fullest advantage of the concrete pressure vessel.

Changes to the graphite structure of quite fundamental nature were made during the design and construction stages as irradiation data at higher neutron doses (more approximating to reactor life) became available from research reactors. These changes are described in the following sections.

3.1 Dimensional Change

In the Calder Hall design, end location of tile-to-tile and tile-to-brick was obtained by keys and keyways placed on the 0° and 90° axis of the channel. This form of keying was only retained at Berkeley. Later designs with tiles at Bradwell and Hinkley Point adopted off-set keys as shown in Figure 4.3. Larger ledges in the fuel channel occur on shrinkage but out of channel coolant leakage is reduced.

The first Magnox stations planned to adopt a double tile layer as in Calder for lateral location of the graphite brick columns. However, as experimental irradiation data on dimensional change became available at higher doses, greater complexity of behaviour was identified. Shrinkage of graphite was shown to occur parallel to the direction of extrusion at temperatures between 150 and 450°C and at temperatures above 300°C in the direction perpendicular to extrusion with growth below 300°C in the latter case.

Slackness in the structure following shrinkage became possible and the solution found was largely influenced by the stage reached in design and construction. For Berkeley, Bradwell and Hinkley Point 'A', which had reached an advanced stage in graphite machining, solutions using zirconium pins were adopted to maintain the channel lattice pitch as shown typically in Figure 4.3. The penalty of the low neutron absorption cross-section of zirconium is acceptable on performance considerations. The Trawsfynydd design was less advanced and a single tile at each brick junction utilizing radial keys on the 90 and 45 axes of the brick was adopted, located in a stable peripheral graphite arch, Figure 4.4.

Later stations at Dungeness, Sizewell, Oldbury and Wylfa adopted side radial keying on the bricks. The peripheral graphite bricks were attached to steel structures which resulted in these bricks being moved radially as steel with change in temperature but the larger Wylfa reactor returned to the compressed arch type of construction to limit radial movement to that of graphite. With movement of the peripheral bricks as steel, those within form a complete mesh and, with imposed movement at the periphery, the lattice pitch of the fuel channel is opened and closed over the whole reactor. Absolute uniformity of lattice pitch in practice is not achieved as a working clearance must be provided in the keys and keyways requiring that allowance be made, in defining charge and control rod path, for the resulting brick freedom being taken up adversely.

The high shrinkage along the axis parallel to extrusion had further consequences on the reactor design necessitating increased allowances for differential column shrinkage to cover spread of experimental data and variation of dose in adjacent brick columns. This had implications mainly on the charge pan design which surmounts the graphite structures

providing location for the fuel and control rod guide tubes. To avoid interference to fuel and control rod movement only small angular deviations from the horizontal can be tolerated. This is most readily achieved by a charge pan covering a large number of channels with well spaced three point support. However, a practical limit to size of a charge pan is imposed by the thermal movement between individual channels within the steel charge pan and accurate alignment of the fuelling chute to the channel. The charge pans carry the burst cartridge detection extraction points for individual fuel channels and may be used to support the sample piping on route out of the vessel. Berkeley, Bradwell and Hinkley Point 'A' used charge pans supported on the graphite with special feet to minimise tilt whilst Trawsfynydd used a system of individual channel charge pans with a surmounting upper plate to locate the guide tubes. Later stations suspended the charge pan from the pressure vessel standpipe, in certain cases with a permanent built-in chute for fuelling, allowing the graphite columns to shrink away with channel continuity maintained by flexibly mounted sleeves.

Dimensional change data presented a further problem due to the variation of irradiation damage within individual moderator bricks. A brick at the core/reflector boundary or with a cross neutron flux gradient experiences higher shrinkage on one side than the other resulting in brick bow. As movement within the reactor structure is restricted at the tiled or keyed layers the columns cannot take up free standing positions and wedge shaped gaps result. From Hinkley 'A' onwards serviette ring type seals, made of magnox and located in grooves, have been incorporated at brick junctions to restrict out of channel leakage. (See Fig 4.5).

Up to Trawsfynydd differential radial thermal movement between the diagrid/support plate and the graphite columns was allowed for by incorporating ball bearing support as at Calder. Access was possible below the diagrid for gag adjustment during commissioning, but with the required higher gas inlet temperatures movements were such that even with built-in cold pre-set, clearances against the diagrid member became inadequate. For Trawsfynydd the complete channel inlet assembly was set above the levelling plate but it required that gag adjustment had to be carried out from charge pan level.

Later reactors with inlet temperatures around 250°C were built with side restraints moving radially as steel so that the lower reflector bricks in the moderator were spigotted directly into the levelling plates. On return to the rigid graphite reflector arch concept for Wylfa a system of rocking support pillars was introduced each carrying four graphite columns on a single levelling plate. This avoided use of ball bearings, which are limited by long term indentation and their low resistance to impact loading.

3.2 Stored Energy

Build up of stored energy in the graphite increases with irradiation dose but anneals out faster at higher temperatures. Stored energy, therefore, influences design most in the bottom half of the reactor. Pessimistic extrapolation of data in the early design stages prior to Trawsfynydd suggested a severe problem and detailed studies were carried out to provide removable channel sleeving schemes. These introduced a stagnant gas barrier between the sleeves and the brick thereby providing thermal insulation from the coolant gas to raise the permanent graphite to a safe temperature. Removable sleeves were introduced into three of the later Chapelcross reactors, and sleeves integral with the fuel elements were adopted at

Hunterston A and Tokai Mura. The need for this undesirable complication was removed when data improved, but the reactors chronologically later than Trawsfynydd all adopted gas inlet temperatures above 200°C to avoid the possibility of a self-sustaining release of stored energy.

3.3 Fault Considerations

At a very late stage in the design and manufacture of the restraint systems for Berkeley and Bradwell the possibility of failure of the main gas ducts was postulated as the worst credible accident. Assessment showed that pressure build-up in the Wigner gaps, resulting from escape of gas from voidage within the graphite under depressurisation, necessitated reinforcement of the restraint structures. The more onerous duty was met at Bradwell, Trawsfynydd and Dungeness 'A' by provision of a surrounding cage structure to restrain radial and overturning movements. Additional elastic garter restraints were provided at Berkeley and Hinkley Point 'A'. At Berkeley the proximity of the cylindrical pressure vessel prevented gross movement and at Hinkley Point 'A' the problem of tilt was met by the provision of dowels at brick interfaces in the peripheral arch.

The change to use of a concrete vessel for Oldbury and Wylfa removed the burst duct fracture as a criterion of restraint design and permitted use of a more restricted pressure circuit breach for gas pressure collapse.

Features to meet earthquake conditions, eg stepping of the levels of bricks in adjacent columns as was adopted at Latina and Tokai Mura, have not been considered necessary for United Kingdom conditions.

4. AGR Moderator Structures

The higher power densities experienced by the AGR cores necessitated the specification of an improved graphite (Gilsocarbon) and an upper moderator temperature of 500° C in order to contain irradiation induced dimensional changes at high dose within acceptable limits.[4] The amount of coolant flow required to achieve this was too large to be taken in parallel with the fuel channel flow without causing unacceptable degradation of outlet gas temperature. The flow was therefore taken in series with the channel flow by directing about 50% of the circuit flow downwards through re-entrant passages formed around the moderator bricks and fuel sleeves to remove the 6% of fission heat which appears in the moderator. After passing through the moderator it mixes with the rest of the coolant which by-passes the core before flowing up the fuel channels. This feature was first introduced into the Windscale AGR prototype.

This change in concept led to a significant increase in the diameter of the brick bore in relation to the lattice pitch, the ratio of these dimensions being approximately 2 to 3, as compared to the value of 1 to 2 used in the Magnox cores which reduced the material available for incorporating radial keys between the channel bores. Thus although the principle of radial keying the core components was retained, it was necessary to make significant changes in the arrangement of the bricks and keys.

The design which evolved for the civil AGRs comprised large hollow 16-sided moderator bricks, one for each fuel channel, connected together by two types of key in a square lattice pitch arrangement as shown in Fig 4.6. Plain rectangular section keys (loose keys) were used between the abutting faces of adjacent bricks on the zero and 90°C axes, and cruciform keys integral with square interstitial bricks (interstitial keys) were used to connect adjacent bricks on the diagonal axes.

A typical AGR moderator design is shown in Fig 4.7 which illustrates the Heysham II/Torness structure. The reactor core is a 16 sided stack of graphite bricks, connected at the periphery to a steel restraint tank. The core contains 332 fuel channels, 89 interstitial control channels and 163 interstitial secondary shutdown channels for the insertion of nitrogen and (for 32 of them) boron beads. The structure incorporates integral graphite and steel shields to reduce radiation levels so that personnel can enter the reactor pressure vessel for inspections.

Columns of large polygonal bricks, 11 high , form the fuel channels whilst smaller square-shaped bricks form either interstitial channels or act as filler bricks. In the radial reflector/shield the bricks are solid, but have small axial holes provided for cooling and insertion of steel shielding rods.

The graphite bricks are inter-connected by graphite keys to provide stability of the assembly and to maintain the vertical channels on their correct lattice pitch. Direct access to each fuel channel is provided by charge tubes that pass through a steel pressure dome which segregates the cool high pressure re-entrant coolant from the hot low pressure channel outlet gas. The lower ends of these charge tubes spigot directly into the top of the core and it is therefore essential to match the thermal expansion of the graphite with that of the pressure dome. This is achieved by connecting the peripheral reflector bricks of the radially keyed core to a steel restraint tank as shown in Fig 4.7, and spigotting the bottom reflector bricks into the steel support plates which are, in turn, radially keyed to the diagrid. Cool re-entrant gas is directed over the inner surface of the pressure dome, the restraint tank and the diagrid thus ensuring near equal thermal expansion of these components. This arrangement enables the core to expand and contract "as steel" under the influence of thermal movements of the diagrid and restraint tank, and allows each brick the freedom to accommodate its own thermal and irradiation - induced dimensional changes without interference.

The keying system is effective over approximately the centre third of each brick except in the top and bottom layers of the core where the keys are practically the full height of the bricks. This keying system extends to the core boundary where restraint rods connect the polygonal bricks to restraint beams at the inter-layer joints. There are 16 of these beams per inter-layer, each attached to the restraint tank by ball-ended restraint links. These links allow for vertical differential thermal movement between the steel tank and the graphite structure.

The key/keyway clearances in the top reflector are made much tighter than the rest of the core. This ensures that the top of each core channel and the bottom of each charge tube are accurately located throughout core life, thus avoiding undue distortion of the charge path. The tighter clearances are made possible by the much lower irradiation dose rates prevailing at the reflector level.

The depth and width of the keys and keyways are optimized to provide maximum strength so that the structure can withstand anticipated core loads with an adequate safety margin when due allowance is made for loss of strength due to radiolytic oxidation. These loads include static loads due to brick bowing, restraint movement and gas pressure differentials, and dynamic loads from a seismic disturbance.

On top of the core is the upper neutron shield comprising overlapping square-section graphite and steel bricks . Below the core is the lower neutron shield comprising graphite bricks of similar design into which are inserted the steel fuel element support stands and their catchpots. The whole graphite structure is supported on, and located by, a series of large steel support plates which rest on a diagrid.

Coolant flow through the core follows two routes. The larger re-entrant fraction flows downwards through the inter-brick gaps and sleeve/brick bore annulus to cool the graphite. The smaller bypass flow passes beneath the diagrid and then flows upwards through the lower neutron shield where it mixes with the re-entrant flow before entering the base of the fuel stringers.

4.1 Radiolytic Oxidation

Radiolytic oxidation is an important consideration in reactor design because it reduces graphite strength, may change the dimensional behaviour of the graphite and, by removing moderator, may bring about the need for increased fuel enrichment. The addition of small concentrations of methane to the coolant gas is known to greatly reduce the rate of oxidation, but it was realised that methane destruction by radiolysis could bring about severe depletion of the inhibitor at positions within the moderator bricks remote from machined surfaces on account of the very low diffusivity of nuclear graphite. Calculations indicated that this could give rise to unacceptably high weight loss at the brick interior, and so several methods of improving methane access were investigated.

Increasing methane concentration in the coolant was ruled out because this gave rise to unacceptable levels of carbonaceous deposition on the fuel cladding surface resulting in loss of heat transfer efficiency. Inducing a permeable flow of coolant gas through the pores proved impractical in the early AGRs since the required pressure drop across the brick wall was not available. The solution adopted was to drill a number of axial holes through the thickest parts of the bricks in order to reduce the length of the diffusion paths. By the time Heysham II and Torness were constructed it became possible to engineer a radial pressure drop of about 0.07 bar between the brick outer surface and the brick bore. This feature was therefore adopted as a means of inducing permeable flow of coolant through the graphite pores, although the drilling of axial holes was still retained as a safeguard.

5. AGR Fuel Sleeve Design

Graphite was first used as a structural member in fuel elements when it was introduced into the design of fuel for Berkeley Magnox reactors in which each uranium fuel pin is supported between a pair of struts which engage in slots cut in the channel wall. At a later stage in Magnox reactor development the build-up of stored energy became important and graphite sleeves were introduced into the fuel element designs of the Hunterston "A" and Tokai Mura

reactors with the primary objective of raising moderator temperature at the cool inlet end of the core. The advent of the AGR with its higher gas outlet temperature and re-entrant flow arrangement has resulted in sleeves becoming an essential part of the fuel assembly. At the same time their duty has become somewhat more onerous on account of the more highly-rated conditions under which they are required to operate.

The requirements of the AGR fuel sleeve are:

i. To provide support for a cluster of 36 fuel pins via the grid and braces of the fuel assembly.

ii. To provide a thermal barrier between the cool re-entrant and hot fuel channel gas flows.

iii. To provide a secure pressure barrier between re-entrant and fuel channel coolant gas flows through which both joint leakage and permeable flow are minimised.

iv. To retain dimensional stability under fast neutron irradiation.

v. To possess adequate impact strength before and after in-pile exposure in order to permit safe on-load charge/discharge operations.

A pitch coke graphite was selected as the sleeve material since this could be manufactured to a specification which most closely matched the above requirements. It possesses good impact properties, can be impregnated to give a low permeability, and although anisotropic is nevertheless reasonably stable under the required operating regime. Sleeve graphites having near isotropic properties have since been developed.

An example of the graphite sleeve design first adopted for the Civil AGRs is shown in Fig 4.8 which illustrates the Hinkley Point "B" fuel element. The sleeve is of double-wall construction comprising one outer and two inner sleeves. The lower inner sleeve is screwed into the bottom end of the outer sleeve where it clamps the bottom fuel pin support grid. The upper inner sleeve, on the other hand, is retained by means of a screwed ring which also clamps the upper fuel pin support brace. The free ends of the two inner sleeves have slots cut in them to provide location for the radial keys of the centre fuel pin support brace. An axial clearance is provided between free ends of the two inner sleeves to allow for differential axial shrinkage and thermal expansion, and axial creep of the outer sleeve under the influence of the static load imposed in the reactor by the weight of components above. For similar reasons, an axial clearance is provided between the ends of fuel pins on abutting elements.

The inner sleeves are designed primarily as a thermal barrier. This is achieved by undercutting the wall of the inner sleeve to leave a location at either end and a radial clearance of 1.3mm over the major portion of the sleeve length, thus providing a stagnant gas space between inner and outer sleeves. A further function of the inner sleeves is to support and locate the stainless steel grid and braces which space the fuel pins, and to provide axial alignment of the pin assembly by keys registering in slots cut into the sleeves.

The use of double-wall construction results in the outer sleeve being thinner and significantly weaker under transverse impact loading than would be the case if a single thick sleeve was used. Heat transfer calculations indicated that loss of heat through the wall of a single sleeve would be tolerable, and so in view of the potential improvement in safety margin under impacts sustained during on-load refuelling it was decided to develop what became known as the Stage 2 AGR fuel sleeve. Figure 4.9 illustrates this design from which it may be seen that a much more robust sleeve is obtained in which the grid and braces are sprung and locked into three grooves machined in the sleeve bore. All new fuel elements loaded into the Civil AGRs now have Stage 2 graphite sleeves.

6. Assessment of Irradiation Effects

The integrity of the graphite moderator structure is dependent upon the strength of its individual components. Thus brick shapes and key widths are optimised for maximum strength on the basis of tests conducted on representative slices of graphite bricks. Although a limited number of failures could probably be tolerated, the design criterion which has been adopted is that there should be no graphite failures.

The condition of the graphite moderator bricks and keys will change significantly due to in-pile exposure. The dimensions and shape will be modified, the physical properties and strength will be significantly altered, and the components will be subjected to both thermal and irradiation-induced internal stresses. Reliable assessment of these effects is an essential component of the safety case for continued operation of the reactor since failure to demonstrate the integrity of the moderator structure is potentially life-limiting. The various issues which must be addressed in the assessment of graphite moderator structures are briefly discussed below.

6.1 Brick Bowing

The correct functioning of the core is critically dependent upon the clearances between keys and keyways. Thermal expansions and contractions of the steel restraint tank cause relative sliding of keys in keyways due to the lower expansion coefficient of graphite. Too small a clearance would cause jamming and heavy loads on the bricks and keys. Too large a clearance would allow excessive lateral movement of the brick columns and cause possible difficulties with fuel cooling and control rod insertion..

Bricks will bow when one side shrinks axially more than the other due to the existence of a transverse damage flux gradient. Such gradients may exist due to the proximity of absorbers, empty channels or side reflector, but can also be the result of rating variations between fuel channels. Differential bowing between one brick and another to which it is keyed may be caused by differences in damage flux gradient, damage dose or material variability. It has the effect of reducing key/keyway clearance. This is allowed for in design calculations to determine key and keyway dimensions, but may require assessment in the later stages of core life when more reliable data on graphite behaviour become available.

Another effect of brick bow is to bring about a small reduction in the effective bore size of the channels, although this is usually small enough to be unimportant. A more significant effect of brick bow is to cause a reduction in column stability due to the opening up of

wedge-shaped gaps between brick end faces. The resultant loads are not large, the main concern being whether or not alignment of unstable columns is maintained by the radial keying system.

6.2 Brick Barrelling

Brick barrelling is a change in brick shape which is brought about by differences in shrinkage rate between the bore and outer region of the moderator brick which are, in turn, due to the radial damage flux gradient. The radial fall-off in damage through the brick wall causes the bore region to shrink more than the outer region for the major part of reactor life. The net result of this differential shrinkage is to produce tensile stresses at the bore and compressive stresses near the periphery. In an infinitely long brick all plane sections would remain plane. However, in a moderator brick of finite length the lack of axial restraint at the brick ends causes the ends to "barrel" inwards so that the end faces become "dished". The effect is largely the result of the fall-off in axial stress towards the brick ends, and its main significance is in the effect it may have on brick-to-brick end sealing.

6.3 Brick Wheatsheafing

Brick "wheatsheafing" may occur rather late in moderator life after the onset of shrinkage reversal if the growth rate at the bore is sufficiently greater than that at the brick exterior. This again is the result of the discontinuity at brick ends, but is opposite in sense to brick barrelling. The delay in shrinkage reversal brought about by radiolytic oxidation may well have the effect of significantly reducing or even preventing the occurrence of brick wheatsheafing.

6.4 Keyway Dovetailing

Differential shrinkage across the moderator brick wall also causes hoop stresses as well as axial stresses. The outer region of the brick is in compression for the major part of life, whilst the bore region is in tension. However, the presence of keyways relieves the compressive stresses in the outer region causing the keyway sides to collapse inwards and become dovetail shaped. This change in keyway shape causes a reduction in key/keyway clearance which is allowed for in the design, but may not necessarily be adequate. In extreme cases the clearance between key and keyway can be lost altogether, and the key then becomes jammed in the keyway. This may give rise to additional stress being generated at the keyway root, usually referred to as "key pinching stress". It may also result in the generation of inter-column loads during thermal transients.

6.5 Thermal Stresses

Temperature gradients will clearly be present due to heat conduction from the brick interior. These temperature gradients will increase due to irradiation-induced increases in graphite resistivity. The resultant differential thermal expansions will give rise to thermal stresses which will be alleviated by irradiation creep. However, when the reactor is shut down and the temperature gradients disappear, the thermal stresses will re-appear but in opposite sense, ie previously compressive stresses will become tensile, and vice versa. The shutdown thermal stresses may augment other stresses present in the bricks, and must be taken into

account in any assessment of brick integrity. The ABAQUS code is used to evaluate thermal stresses taking into account the various factors which influence their magnitude including irradiation-induced changes in thermal conductivity, coefficient of thermal expansion and Young's modulus. The calculation routine may be modified to include the evaluation of key pinching stresses referred to in Section 6.4.

6.6 Shrinkage Stresses

Significant variations in shrinkage rate will occur across the brick section due to the radial and circumferential variations in temperature and dose rate. These variations in shrinkage rate are largely accommodated by irradiation creep of the graphite, but nevertheless residual stresses and strains remain which may significantly reduce the ability of the brick to withstand external loading. The residual shrinkage stresses may well be augmented by thermal stresses during shutdown as described in Section 6.5. Calculation of shrinkage stresses is a complex procedure in which allowance must be made for the numerous effects of in-pile exposure and radiolytic oxidation on such properties as dimensional changes, irradiation creep and Young's modulus. The ABAQUS code is used for this type of calculation. The results of such calculations indicate that whilst stresses at the vulnerable keyway root are compressive during about the first half of reactor life, the subsequent onset of shrinkage reversal causes the stress pattern to change. When this happens, tensile stresses develop at the keyway root which is where the highest tensile stresses occur under external loading. From this it will be clear that shrinkage stresses are an important component in the assessment of moderator brick integrity.

7. Brick Loads

Loads on the bricks and keys may arise from three main sources:

i. Restraint movements.

ii. Gas pressure forces.

iii. Irradiation-induced brick distortions.

iv. Seismic forces.

An assessment is carried out to determine the capability of the bricks and keys to withstand these loads when it is necessary to make due allowance for changes in load-carrying capacity during life including:

a. Reductions in strength due to radiolytic oxidation.

b. Increases in strength due to fast neutron irradiation.

c. The development of shrinkage stresses across the brick section.

d. The development of thermal stresses during shutdown conditions.

e. The development of key pinching stresses.

7.1 Loads due to Restraint Movements

In designs where the graphite core expands and contracts "as steel", relative movement between columns will occur due to the lower thermal expansion of graphite. Any tightness of the graphite radial keying system may limit free intercolumn movement and generate loads.

The thermal inertia of the restraint tank and diagrid are also different, and so sudden changes in reactor operating conditions may cause these two components to respond thermally at different rates. The resultant differential radial thermal expansions (or contractions) will cause the graphite columns to tilt and thereby generate transverse loads. The number of columns affected, and hence the magnitude of the loads, will be dependent upon the difference in radial movement between one layer and another, and upon the amount of free movement permitted between adjacent graphite columns by the slackness of the graphite key/keyway system. The evaluation of loads due to boundary structure movement is done using classical statics, although computer codes can be used to solve the complex equations describing column interactions.

7.2 Loads due to Gas Pressure Forces

Although gas pressures in the re-entrant passages are nominally uniform, pressure variations do exist across the core due to zonal differences in cooling rate (eg between core reflector and side shield), the use of short or long keying, provision of cross flow headers and leakage of gas through boundary sealing keys. The pressure distribution is established from core flow network calculations which may be a 2D ring model network or a 3D octant model of the core. Pressure disturbances may also occur when fuel channels are empty during on-load refuelling operations.

7.3 Loads due to Irradiation-Induced Brick Distortions

Loads from this source arise due to brick bowing and have already been mentioned in Section 6.1. The loads are not expected to be large because they arise due to pivoting of the bricks about one edge (on the side where axial shrinkage is lowest), and since the restoring forces required to maintain a "pin-jointed" column of bricks in equilibrium can be shown to be quite small. Much larger forces could arise if bricks in a given column were to bow in opposite directions due to some bricks having gone into shrinkage reversal. However, quite apart from the fact that this scenario is unlikely, it is considered that the transverse slackness of the radial keying system is such that the development of large bowing forces from this source is highly improbable. Evaluation of loads is by classical statics.

7.4 Loads due to Seismic Forces

Transverse vibrations of the moderator structure may induce large inertia forces within the graphite core. These forces would be transmitted to the restraint tank via the restraint links and the graphite keys which connect each brick to its neighbours. The evaluation of seismic impact forces on the graphite keys and restraint links is extremely difficult due to the

complexity of performing a seismic response analysis on a structure comprising a large number of interconnecting components having several degrees of freedom. NCC have carried out such calculations for Heysham II/Torness using the computer code AGRCORE at enormous expense. The results are difficult to validate.

8. Failure Criterion

Experimental work has shown that when an AGR graphite brick is subjected to external loading via the keys and keyways it will fail in tension via a crack initiated at the keyway root. The calculated stress at failure, σ_{cr} is used as the basis for evaluating the structural integrity of graphite bricks following in-pile exposure after making due allowance for:

i. Changes in graphite strength (σ_{cr}) due to fast neutron hardening and radiolytic oxidation

ii. Shrinkage stress (σ_s)

iii. Thermal stress at shutdown (σ_t)

iv. Key pinching stress (σ_k)

8.1 Reserve Strength Factor

Until fairly recently, combining the above stress mechanisms into a single failure criterion was achieved using the "reserve strength factor" (RSF) equation, defined as:

$$RSF = \frac{\text{Residual strength}}{\text{Stress due to applied load}}$$

which, in terms of the mechanisms described above any be written:

$$RSF = \frac{\sigma_{cr} - (\sigma_s + \sigma_t + \sigma_k)}{\sigma_L} \qquad (1)$$

where: σ_L is the load applied stress

Thus, for an RSF = 2, the strength remaining in the brick is twice the load which must be borne. The RSF may thus be interpreted as a factor of safety for the component.

8.2 Fractional Remanent Strength

Recent experimental work has indicated that there is a different value of critical stress associated with each of the above four stress mechanisms. Furthermore, it is considered necessary to apply separate correction factors to each critical stress when applying the results of slice tests to bricks and to allow for practical loading conditions. Three factors need to be defined:

i. *Material Bulking Factor*

This reflects the changes in the strength of graphite as greater volumes are stressed.

ii. *Geometric Bulking Factor*

This reflects the difference in fracture load of a brick loaded along the full length and one loaded along only part length.

iii. *Key Tilt Factor*

This makes allowance for any tilting of the key in the keyway which serves to localise force transfer.

It was considered that the RSF equation could not adequately represent the requirement for different critical stresses and correction factors, and that a more suitable approach was to use fractional remanent strength in which all the terms of the equation are ratios of predicted and ultimate stresses. The fractional remanent strength (Δ S) is defined as[2]:

$$\Delta S = 1 - \left[\frac{\text{shrinkage stress}}{\text{critical internal stress}}\right] - \left[\frac{\text{shutdown thermal stress}}{\text{critical thermal stress}}\right] - \left[\frac{\text{keyway pinching stress}}{\text{critical key pinching stress}}\right] - \left[\frac{\text{load applied stress}}{\text{critical load applied stress}}\right]$$

The brick would be deemed to fail when ΔS is less than or equal to zero.

The equation above may be rewritten as follows when including the various factors which need to be applied to the critical stress values:

$$\Delta S = 1 - \left[\frac{\sigma_s}{M_s\sigma_{crs}} + \frac{\sigma_t}{M_t\sigma_{crt}} + \frac{\sigma_k}{M_kG_k\sigma_{crk}} + \frac{\sigma_L}{M_LG_LK\sigma_{crL}}\right] \quad (2)$$

where: σ_s, σ_t, σ_K and σ_L are the predicted values of shrinkage, thermal, key pinching and load applied stresses.

σ_{crs}, σ_{crt}, σ_{crk} and σ_{crL} are the corresponding critical stresses

M_s, M_t, M_k and M_L are the corresponding material bulking factors.

G_K and G_L are the geometric bulking factors for key/pinching and load applied stress

K is the key tilt factor.

Values for the critical stresses and factors M, G and K must be determined by experiment and may be different for each type of graphite and brick geometry.

References

1. Graphite Structures for Nuclear Reactors. Conference organised by the Nuclear Energy Group of the Institution of Mechanical Engineers. March 1972.

2. Davies M A and Judge R C B. Recommendations for Graphite Core Brick Failure Criterion. AEA-RS-5296, July 1992.

TABLE 4.1 LEADING PARTICULARS OF CEGB MAGNOX REACTORS

Station	Number of Fuel Channels	Pressure Containment	Design Conditions			Peripheral Restraint	Thermal Movement of Peripheral Bricks	Brick Location	Interbrick Seals	Charge Pans
			Gauge Pressure MN/m^2	T_1 °C	T_2 °C					
BERKELEY	3265	Steel Cylindrical	0.9584	160	345	Temperature Compensated Tie Bars	As graphite	Butting Tiles with Zirconium Pins	No	Supported on graphite
BRADWELL	2624	Steel Spherical	1.0136	180	390	Temperature Compensated Tie Bars with outer cage	As graphite	Butting Tiles with Zirconium Pins	No	Supported on graphite
HINKLEY POINT 'A'	4500	Steel Spherical	1.3790	181	378	Temperature Compensated Tie Bars with dowelled reflector	As graphite	Butting Tiles with Zirconium Pins	Yes	Supported on graphite
TRAWSFYNYDD	3740	Steel Spherical	1.7582	202	392	Temperature Compensated Tie Bars with outer cage	As graphite	Radially Keyed Tiles with cruciform Keys	Yes	Supported on graphite
DUNGENESS 'A'	3932	Steel Spherical	1.9651	250	410	Steel cage with puller rod attachment to peripheral bricks	As steel	Radial Keys	Yes	Suspended on control rod guide tube
SIZEWELL 'A'	3784	Steel Spherical	1.9306	214	401	Steel rings dowelled to graphite and radially keyed to a restraint tank	As steel	Radial Keys	Yes	Suspended from standpipes as composite control/ charge facility
OLDBURY 'A'	3308	Concrete Cylindrical	2.5167	250	411	Steel rings hung from boiler shield wall with puller rods attached to peripheral bricks	As steel	Radial Keys	Yes	Suspended from control rod guide tubes
WYLFA	6156	Concrete Spherical	2.7580	247	414	Temperature Compensated Tie Bars	As graphite	Radial Keys	Yes	Suspended from standpipes as composite control/ charge facility

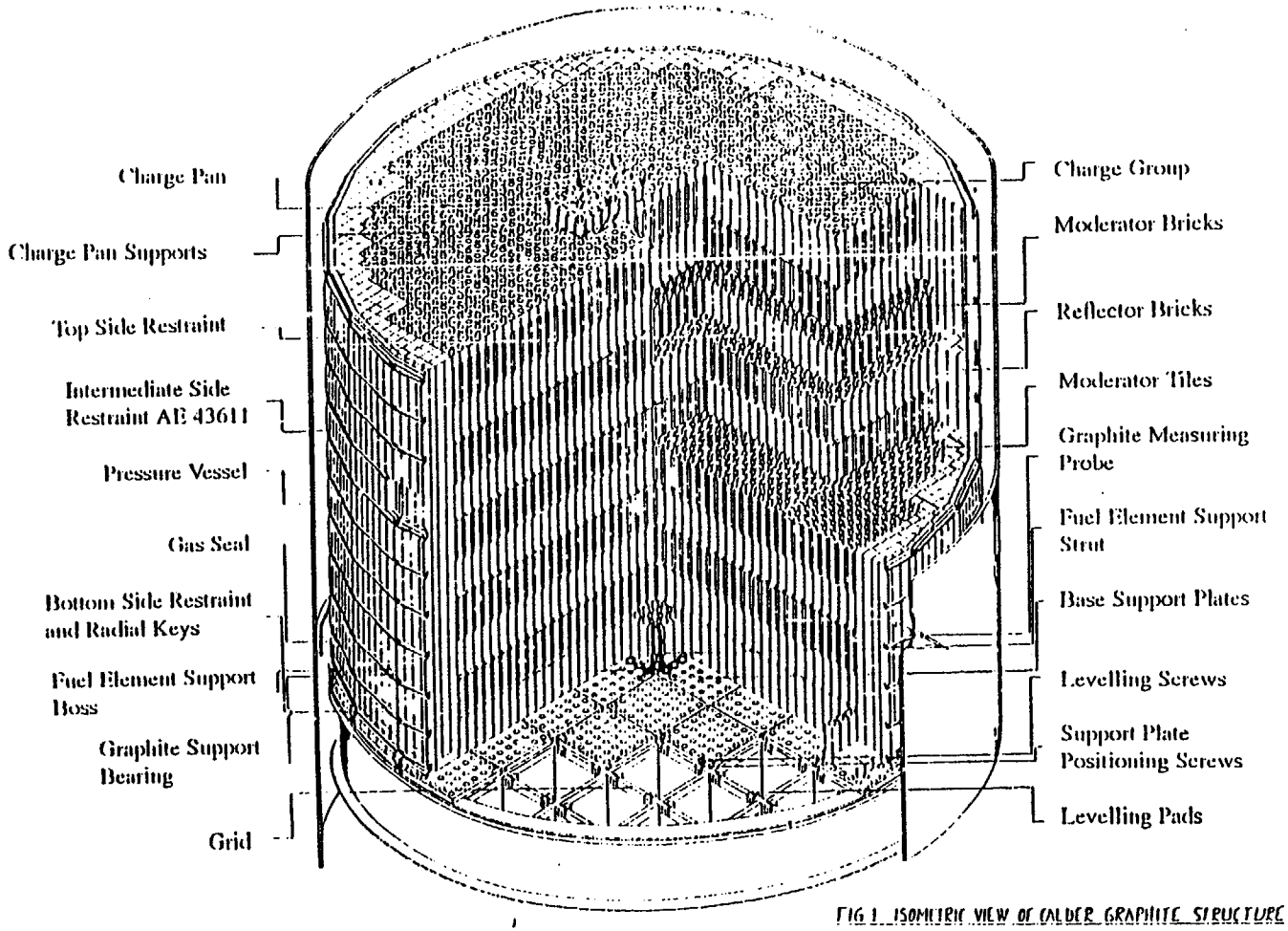

FIG 1 ISOMETRIC VIEW OF CALDER GRAPHITE STRUCTURE

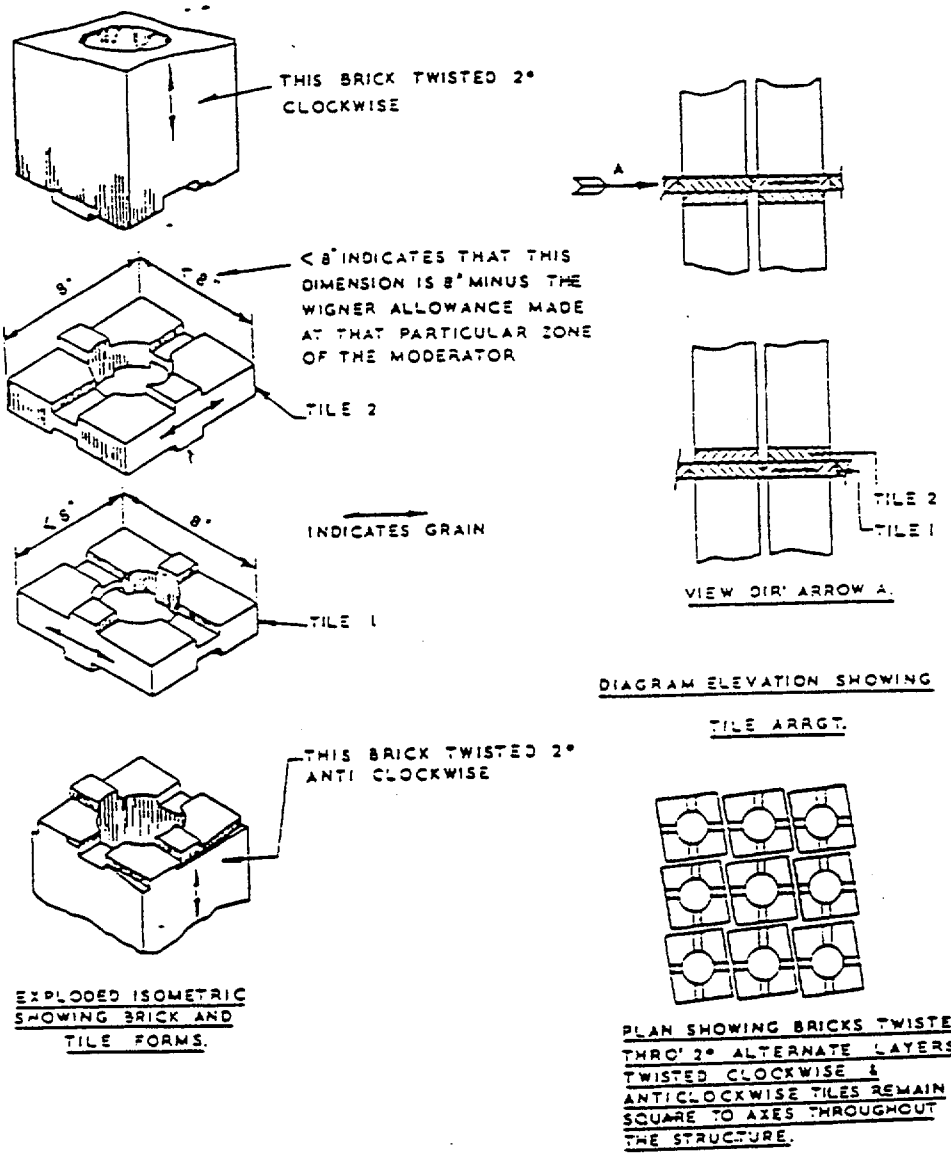

FIG 2 CALDER WORKS MODERATOR STRUCTURE.

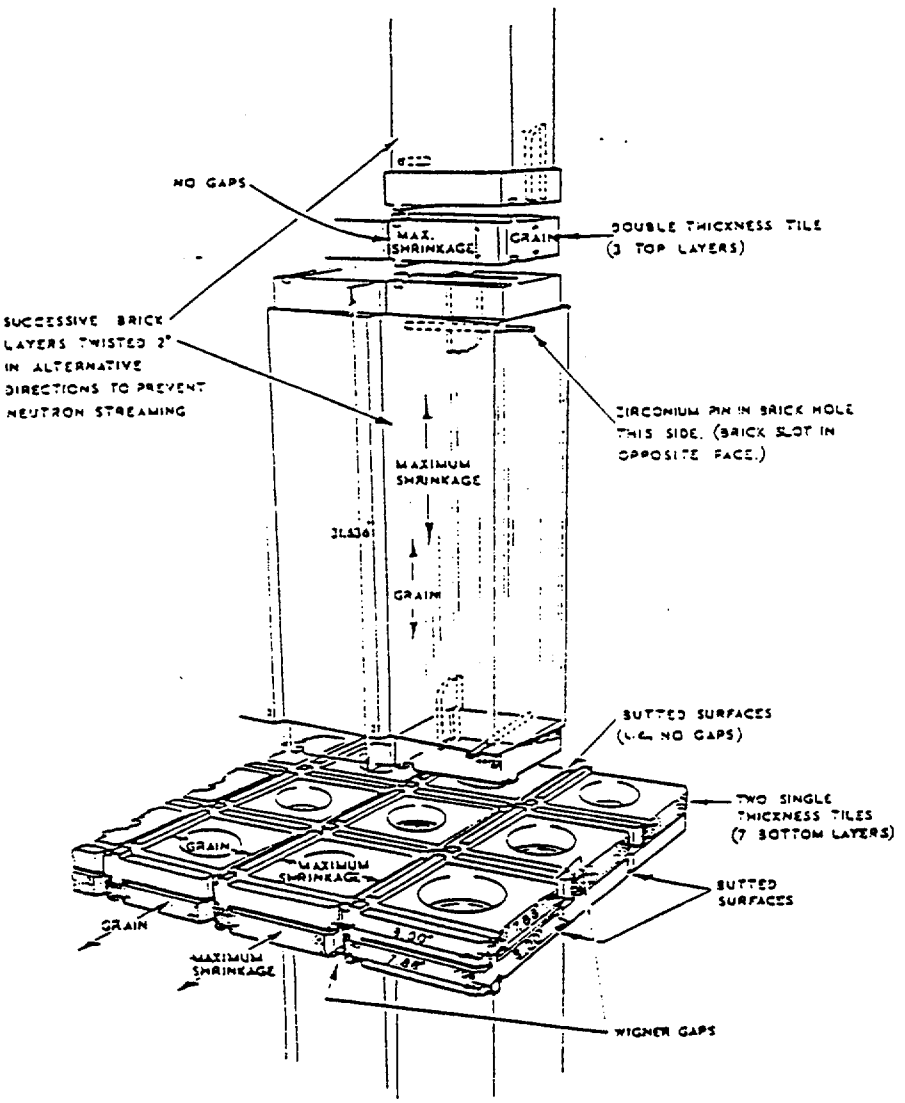

FIG.2. REPRESENTATION OF GRAPHITE COLUMN SHOWING BRICKS, TILES, INTER-KEYING, ZIRCONIUM PINNING, WIGNER GAPS AND EXTRUSION DIRECTIONS.

TRAWSFYNYDD

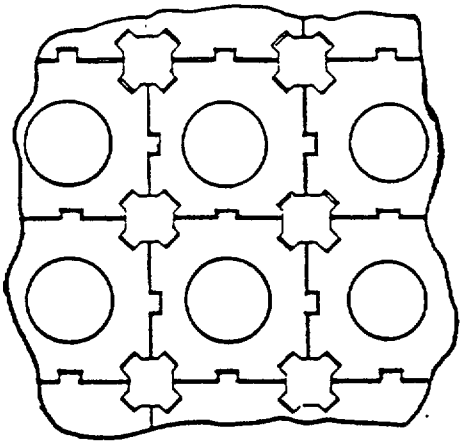

(a) RADIALLY KEYED TILE LAYER

LATINA

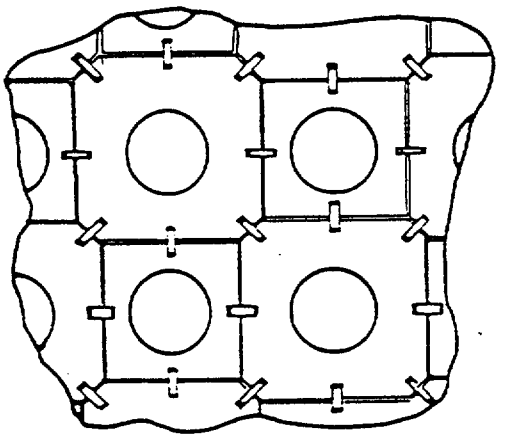

(b) OCTAGON/SQUARE RADIALLY KEYED BRICKS

TOKAI MURA

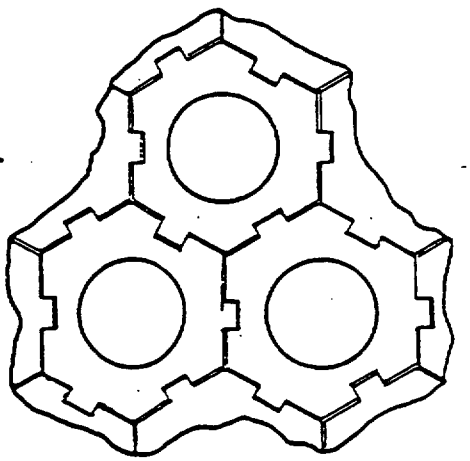

(c) HEXAGON RADIALLY KEYED BRICKS

Figure 4. EXAMPLES OF RADIAL KEYING USED IN MAGNOX REACTOR CORES

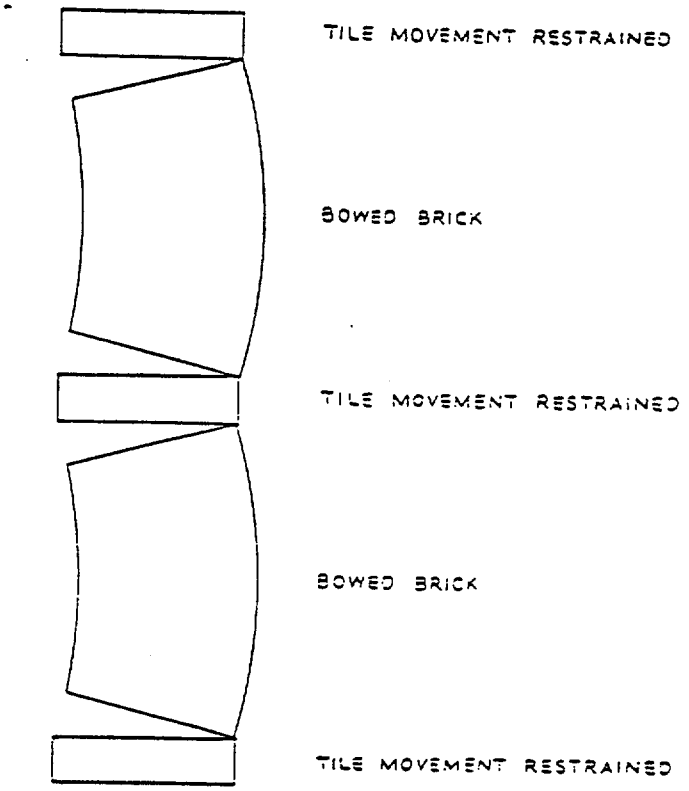

FORMATION OF BRICK GAP

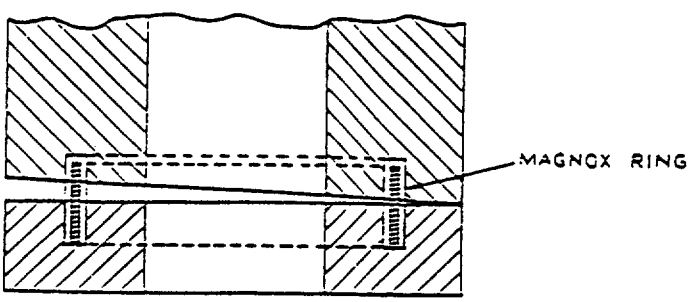

Fig 5. CROSS-SECTION THROUGH BRICK/TILE INTERFACE SHOWING USE OF MAGNOX RING AS A SEAL.

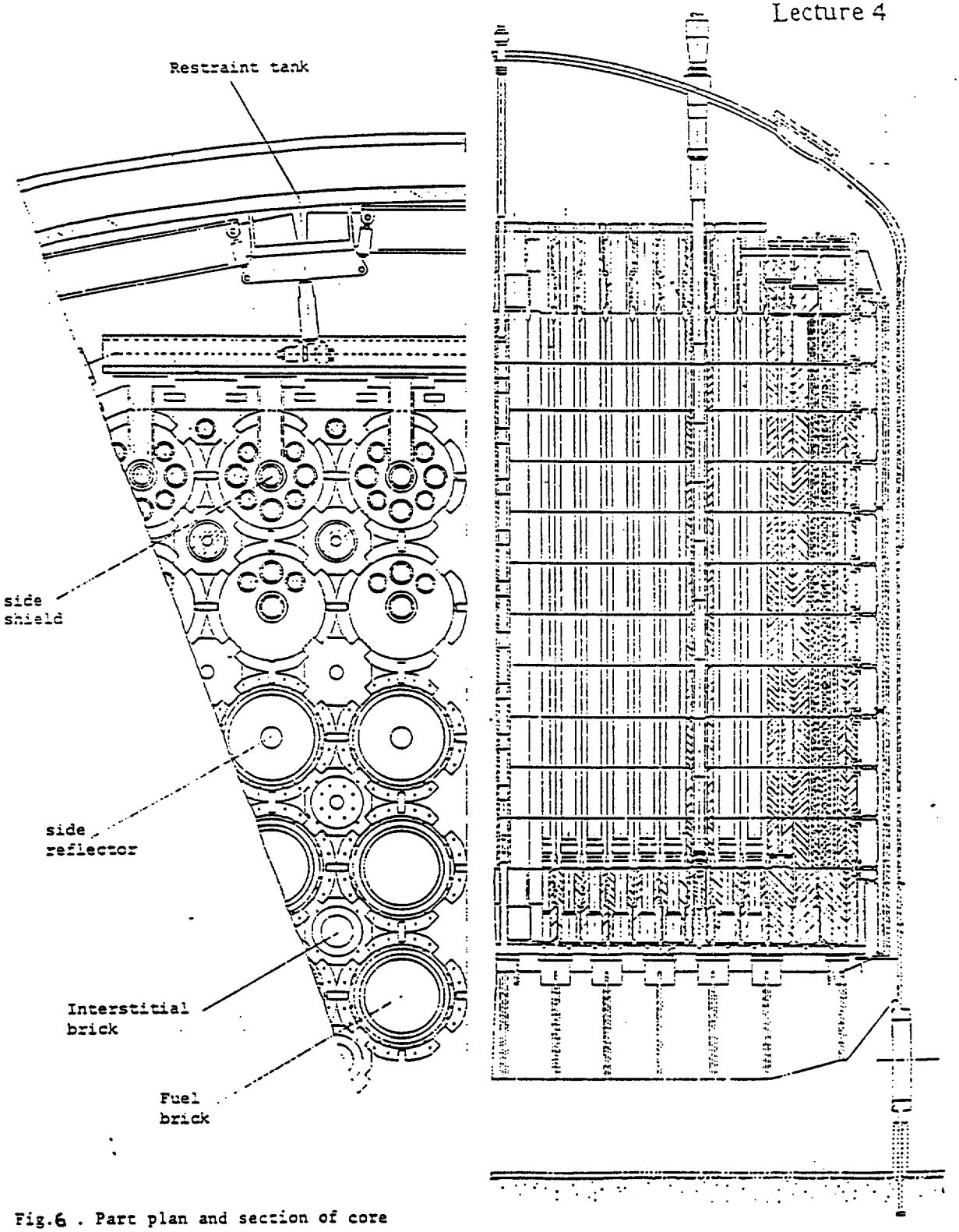

Fig.6 . Part plan and section of core

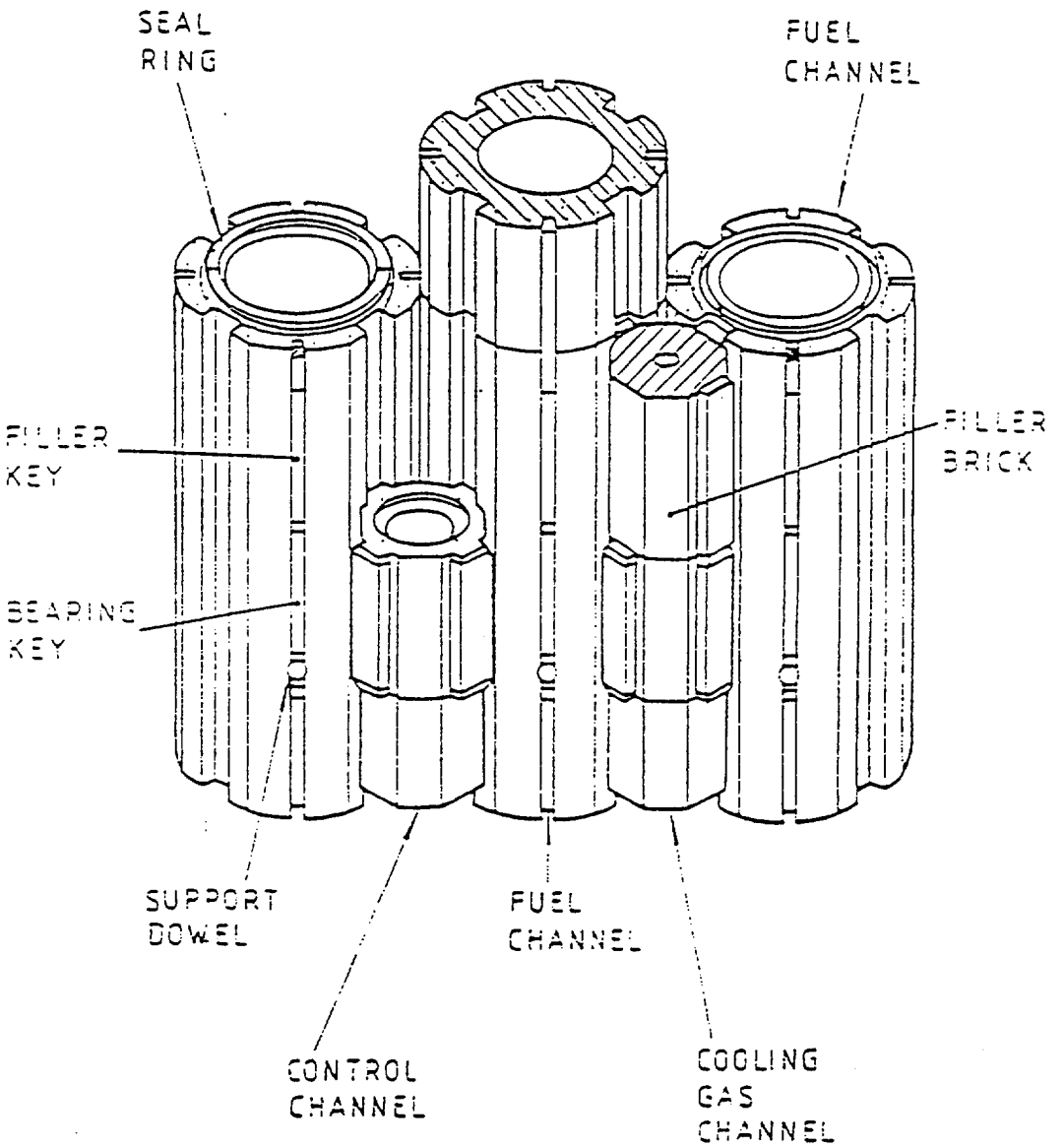

Figure 7. Core Bricks and Keys

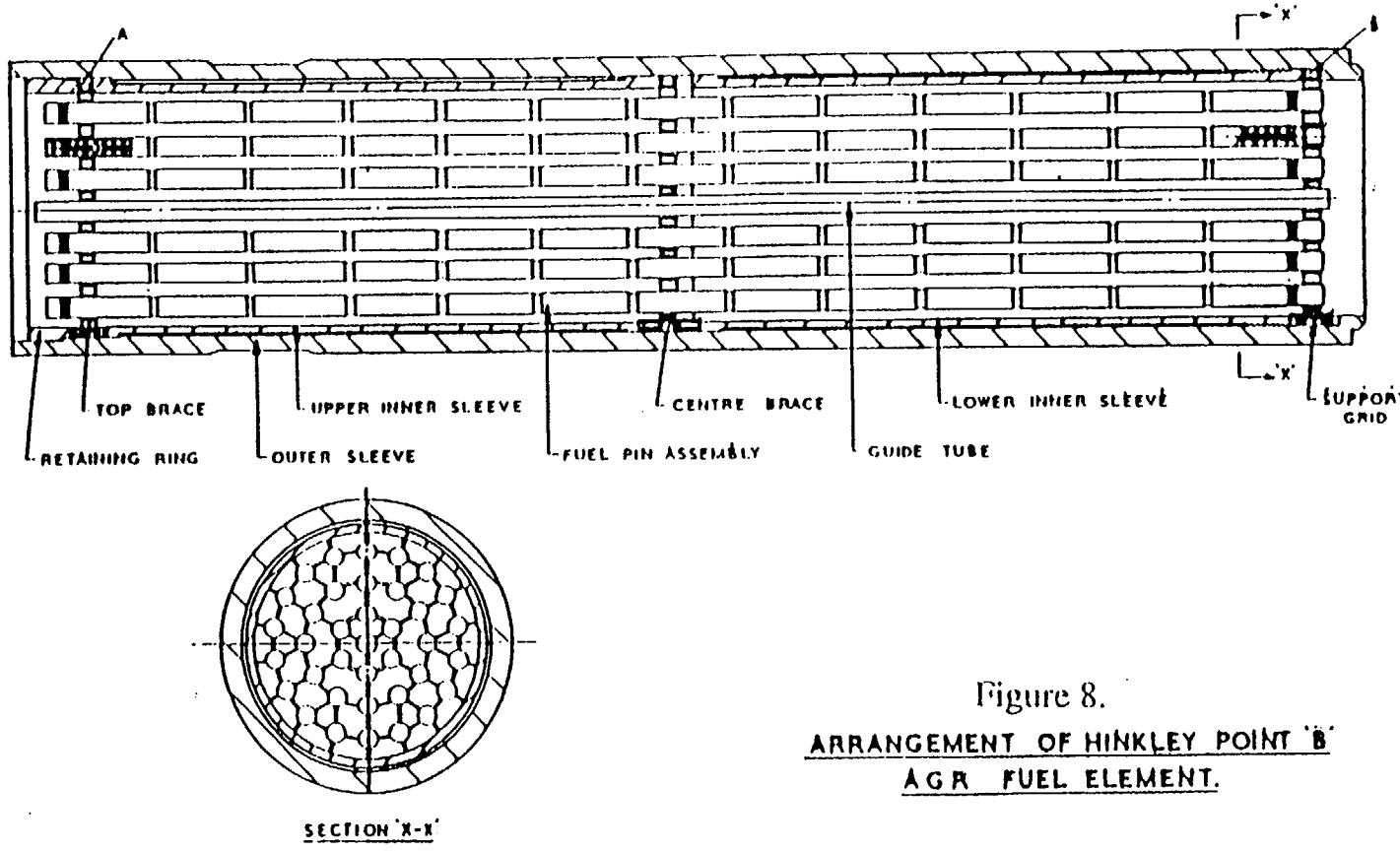

Figure 8.

ARRANGEMENT OF HINKLEY POINT 'B'
AGR FUEL ELEMENT.

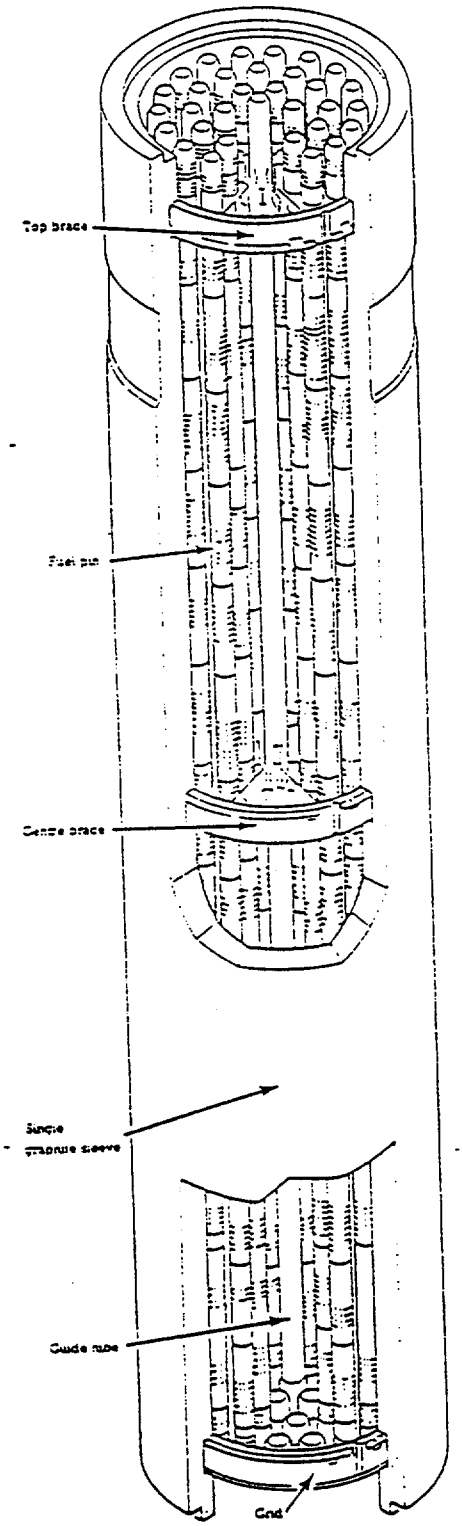

Figure 9.

Commercial AGR Stage 2 fuel element - performance and safety studies by TAD.

Exercises

Case 1

Calculate the radial variation of damage function, Calder equivalent rating, dose and temperature for the following example of a single rod of natural uranium in a single fuel channel surrounded by graphite using the following parameters.

Fuel burnup	= 45,000 MWd/t
Operating life at constant fuel rating	= 30 years at 85% load factor
Fuel rod cross sectional area	= 1.0 in^2
Channel bore diameter	= 4.0 in
Graphite density	= 1.70 g/cm^3
Graphite operating temperature	= 400 °C
Activation energy	= 1.2eV

Case 2

Calculate the DIDO nickel dose, dose rate and DIDO equivalent temperature at the channel bore position in Case 1.

Case 3

Calculate the damage function at the bore of the central fuel channel of a 5 by 5 array of 4.0 inch fuel channels located on a 10 inch square lattice pitch, assuming all 25 channels have the same parameters as those in Case 1. The position of interest should be assumed to lie on a line joining the central fuel channel to one of it's closest neighbours.

What is the percentage of the total damage contributed by the five channels closest to the point of interest?

Case 4

If the fuel burnup on channel rows A,B,C,D and E are as follows, calculate the DIDO nickel dose at the point of interest

	A	B	C	D	E
Burnup, MWd/t	46,000	44,000	42,000	40,000	38,000

Case 5

How would you expect graphite weight loss and dimensional changes to affect calculated damage function values?

4 cm = 10 inch

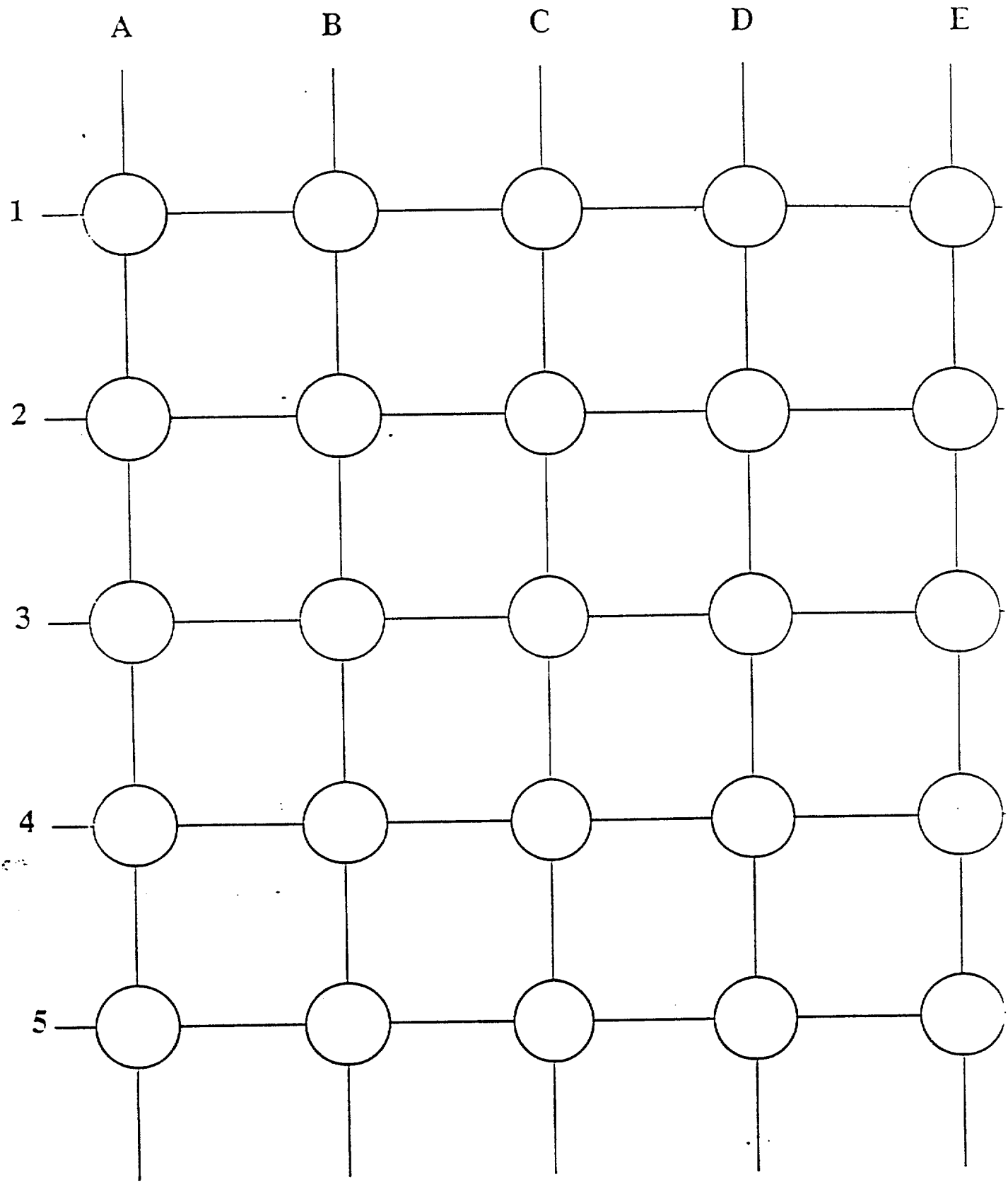

Exercises

Case 1

Using the parameters for Case 1 of Lecture 1 Workshop, estimate the percentage radial variation in dimensional change at the end of operating life in the parallel to extrusion direction of PGA graphite assuming a constant irradiation temperature of 200 °C. Limit the calculation to a 5 inch thickness of graphite.

Case 2

A PGA graphite component having unirradiated $\alpha_{(20\text{-}120)}$ thermal expansion coefficient values of $3.0 \times 10^{-6}\ °C^{-1}$ perpendicular and $0.8 \times 10^{-6}\ °C^{-1}$ parallel is irradiated at 300 °C to Calder equivalent dose of 40,000 MWD/T at a constant Calder equivalent rating of 4.38 MW/T.

Estimate the post-irradiation CTE values in terms of:

a) The mean CTE between 20 °C and 120 °C, $\alpha_{(20\text{-}120)}$

b) The instantaneous CTE at 300°C

c) The mean CTE between 20°C and 300°C, $\alpha_{(20\text{-}300)}$.

Case 3

A PGA component is irradiated at 200°C to a Calder equivalent dose of 20,000 MWD/T whilst the reactor is operating continuously at constant power for a total of 25 years. During this time the component suffers 10% weight loss due to radiolytic oxidation. Calculate the resultant thermal conductivity at a temperature of 200°C assuming an unirradiated value of 100 W/m K at 30°C.

Case 4

What are the end of life values of total stored energy, E and the rate of release of stored energy, $(dE/dT)_{max}$, for the component in Case 3? If $(dE/dT)_{max}$ occurs at 400°C, what is the fraction of specific heat represented by stored energy release at this temperature?

Case 5

Produce the relationship which describes the dimensional change versus dose of Gilsocarbon graphite in terms of values read from the curves in Figure 4, if the graphite total opv is 0.11 cm^3/cm^3 and the coolant gas composition is 1% CO and 300 vpm CH_4.

Case 6

A Heysham II / Torness graphite component is irradiated at a temperature of 450°C to a total dose of 1.8×10^{22} n/cm^2 whilst operating at constant power for 25 years. During this time the component suffers 20% radiolytic weight loss. Estimate the resultant thermal conductivity at 450°C assuming an irradiated value of 128 W/m°C at 30 °C.

Case 7

A Gilsocarbon graphite component having an unirradiated coefficient of of thermal expansion, $\alpha_{(20\text{-}120)}$, value of 4.5×10^{-6} °C^{-1} is irradiated to an equivalent DIDO nickel dose of 1×10^{22} n/cm^2 at a constant dose rate of 2×10^{13} n/cm^2. s and at a temperature of 450°C. During this time the component suffers a tensile strain of 1%. Calculate the post irradiation values of thermal expansion coefficient in terms of :

a) The instantaneous CTE at 450°C

b) The mean CTE between 20 and 450°C.

Exercises

Case 1

A graphite brick in a Magnox reactor operating at a temperature of 200°C and a coolant gas pressure of 120 psia is radiolytically oxidised in coolant at a G_{-c} value of 1.2. The virgin values of graphite density and effective open pore volume are 1.7g/cm^{3}and 0.22 cm^3/cm^3, respectively. If the dose rate to graphite remains constant at 0.1W/g, calculate the cumulative weight loss at 5 year intervals up to 25 years continuous operation. Check your answers using Figure 8.

Case 2

If the dose rate increases with mean weight loss (i.e. inversely with graphite density change), estimate new values for the cumulative weight loss every 5 years of operation assuming the following values for mean weight loss during each period.

Period, years	0-5	5-10	10-15	15-20	20-25
Mean Weight loss,%	1	3	5	7.5	10.5

Assume that g_0t for any period 0 to t years is increased by the factor $1/(1-\bar{x})$, $\bar{x}$ is the time averaged fractional weight loss between 0 and t years. Thus for the period 0 to 10 years, $\bar{x}$ =(0.01+0.03)/2 =0.02. Hence the factor $1/(1-\bar{x})$=1/0.98, and so on.

Case 3

If the dose rate in Case 1 is assumed to increase in accordance with operation at constant power, calculate the cumulative weight loss after 25 years using equation 13. Check your answers using Figure 9.

Exercises

Case 4

The virgin values of Young's Modulus and static strength for the PGA graphite component are:

E_o perpendicular	= 5.4 GPa
E_o parallel	= 11.7 GPa
σ_o perpendicular	= 12.0 MPa
σ_o parallel	= 19.0 MPa

Using the weight loss results from Case 2 above, and the following damage dose values, draw up a table of giving the resultant values of Young's Modulus and strength allowing for the combined effects of radiolytic weight loss and fast neutron irradiation. Assume a DIDO equivalent temperature of 250°C.

Time, years	5	10	15	20	25
EDND $x10^{21}$ n/cm^2	0.435	0.871	1.306	1.742	2.177

Answers

Case 1

Fuel rating, $P = \frac{45,000}{30 \times 0.85 \times 365} = 4.83$ MW/t

Calder equivalent rating, $P_e = 0.689 \cdot A \cdot df \cdot P$

$= 0.689 \times 1.0 \times 4.83 \times df$

$= 3.33df$ MW/t

Calder equivalent dose, $D_e = P_e \times 30 \times 0.85 \times 365$

$= 9307 \cdot 5\ P_e$ Mwd/t

$$\frac{1}{T_e} = \frac{1}{T_i} + \frac{k}{E} \log_e\left(\frac{P_e}{3.12}\right)$$

$$= \frac{1}{673} + \frac{8.617 \times 10^{-5}}{1.2} \log_e\left(\frac{P_e}{3.12}\right)$$

Radius	R_g	$R_{g1.6}$	ϕ_{Rg}	$\frac{\phi_{R_g}}{R}$	P_e	D_e	T_e	T_e
Rins	ins	ins			MW/t	MWd/t	$^\circ K$	$^\circ C$
2	0	0	1.0	0.50	1.665	15,497	694	421
3	1	1.06	1.2	0.40	1.332	12,398	702	429
4	2	2.13	1.15	0.288	0.959	8,926	714	441
5	3	3.19	1.025	0.205	0.683	6,570	726	453
7	5	5.31	0.74	0.106	0.353	3,286	752	479
12	10	10.63	0.29	0.024	0.080	745	818	545
17	15	15.94	0.12	0.007	0.020	186	890	617
22	20	21.25	0.04	0.002	0.007	65	954	681
27	25	26.56	0.02	0.01	0.03	28	1013	740
32	30	31.58	-	-	-	-	-	-

Answers

Case 1

Fuel rating, $P = \frac{45,000}{30 \times 0.85 \times 365} = 4.83$ MW/t

Calder equivalent rating, $P_e = 0.689 \cdot A \cdot df \cdot P$

$= 0.689 \times 1.0 \times 4.83 \times df$

$= 3.33df$ MW/t

Calder equivalent dose, $D_e = P_e \times 30 \times 0.85 \times 365$

$= 9307 \cdot 5\ P_e$ Mwd/t

$$\frac{1}{T_e} = \frac{1}{T_i} + \frac{k}{E} \log_e\left(\frac{P_e}{3.12}\right)$$

$$= \frac{1}{673} + \frac{8.617 \times 10^{-5}}{1.2} \log_e\left(\frac{P_e}{3.12}\right)$$

Radius	R_g	$R_{g1.6}$	ϕ_{Rg}	$\frac{\phi_{R_t}}{R}$	P_e	D_e	T_e	T_e
Rins	ins	ins			MW/t	MWd/t	$^\circ K$	$^\circ C$
2	0	0	1.0	0.50	1.665	15,497	694	421
3	1	1.06	1.2	0.40	1.332	12,398	702	429
4	2	2.13	1.15	0.288	0.959	8,926	714	441
5	3	3.19	1.025	0.205	0.683	6,570	726	453
7	5	5.31	0.74	0.106	0.353	3,286	752	479
12	10	10.63	0.29	0.024	0.080	745	818	545
17	15	15.94	0.12	0.007	0.020	186	890	617
22	20	21.25	0.04	0.002	0.007	65	954	681
27	25	26.56	0.02	0.01	0.03	28	1013	740
32	30	31.58	-	-	-	-	-	-

Answers

Case 1

- Fuel rating, $P = \frac{45,000}{30 \times 0.85 \times 365} = 4.83$ MW/t

Calder equivalent rating, $P_e = 0.689 \cdot A \cdot df \cdot P$

$= 0.689 \times 1.0 \times 4.83 \times df$

$= 3.33df$ MW/t

Calder equivalent dose, $D_e = P_e \times 30 \times 0.85 \times 365$

$= 9307 \cdot 5\ P_e$ Mwd/t

$$\frac{1}{T_e} = \frac{1}{T_i} + \frac{k}{E} \log_e \left(\frac{P_e}{3.12} \right)$$

$$= \frac{1}{673} + \frac{8.617 \times 10^{-5}}{1.2} \log_e \left(\frac{P_e}{3.12} \right)$$

Radius	R_g	$R_{g1.6}$	ϕ_{Rg}	$\frac{\phi_{R_t}}{R}$	P_e	D_e	T_e	T_e
Rins	ins	ins			MW/t	MWd/t	$^\circ K$	$^\circ C$
2	0	0	1.0	0.50	1.665	15,497	694	421
3	1	1.06	1.2	0.40	1.332	12,398	702	429
4	2	2.13	1.15	0.288	0.959	8,926	714	441
5	3	3.19	1.025	0.205	0.683	6,570	726	453
7	5	5.31	0.74	0.106	0.353	3,286	752	479
12	10	10.63	0.29	0.024	0.080	745	818	545
17	15	15.94	0.12	0.007	0.020	186	890	617
22	20	21.25	0.04	0.002	0.007	65	954	681
27	25	26.56	0.02	0.01	0.03	28	1013	740
32	30	31.58	-	-	-	-	-	-

Answers

Case 2

EDND $= 1.0887 \times 10^{17} \times D_e$

$= 1.0887 \times 10^{17} \times 15{,}497 = 1.687 \times 10^{21}$ n/cm^2

Equivalent DIDO dose rate, $\phi = \dfrac{1.687 \times 10^{21}}{30 \times 0.85 \times 365 \times 24 \times 3600}$

$= 0.21 \times 10^{13}$ n/cm^2 . s

$$\frac{1}{\theta} = \frac{1}{T_i} + \frac{k}{E} \ln\left(\frac{\phi}{4 \times 10^{13}}\right)$$

$$= \frac{1}{673} + \frac{8.617 \times 10^{-5}}{1.2} \ln\left(\frac{0.21}{4}\right)$$

$\theta = 785$ K

$= 512$ °C

Answers

Case 3

Channel	No.	R	$R_{g_{1.7}}$	$R_{g_{1.6}}$	ϕ_{R_g}	$\Sigma N \cdot \frac{\phi_{R_g}}{R}$	
A1	2	29.8	20.5	21.8	0.043	0.003	
B1	2	23.2	19.0	20.2	0.058	0.005	
C1	2	20.1	14.4	15.3	0.130	0.013	
D1	2	21.6	19.6	20.8	0.053	0.005	
E1	2	26.9	20.9	22.2	0.038	0.003	
A2	2	24.2	18.3	19.4	0.067	0.006	
B2	2	15.6	10.3	10.9	0.279	0.036	
C2	2	10.1	8.1	8.6	0.414	0.082	(9.7%)
D2	2	12.8	10.8	11.5	0.260	0.041	
E2	2	20.5	18.4	19.6	0.063	0.006	
A3	1	22.0	12.0	12.75	0.200	0.009	
B3	1	12.0	6.0	6.38	0.615	0.051	(6.0%)
C3	1	2.0	0	0	1.0	0.500	(59.0%)
D3	1	8.0	6.0	6.38	0.615	0.077	(9.1%)
E3	1	18.0	12.0	12.75	0.200	0.011	
						0.848	

Total Percentage = 9.7 + 6.0 + 59.0 + 9.1

= 83.8 %

Answers

Case 4

Channel	B	$\frac{B}{42,000}$	df (from case 3)	$df \times \frac{B}{42,000}$
A1	46,000	1.095	0.003	0.003
B1	44,000	1.048	0.005	0.005
C1	42,000	1.000	0.013	0.013
D1	40,000	0.952	0.005	0.005
E1	38,000	0.905	0.003	0.003
A2	46,000	1.095	0.006	0.007
B2	44,000	1.048	0.036	0.038
C2	42,000	1.000	0.082	0.082
D2	40,000	0.952	0.041	0.039
E2	38,000	0.905	0.006	0.005
A3	46,000	1.095	0.009	0.010
B3	44,000	1.048	0.051	0.053
C3	42,000	1.000	0.500	0.500
D3	40,000	0.952	0.077	0.073
E3	38,000	0.905	0.011	0.010
				0.846

EDND $= 3.9942 \times 10^{15} \times A \times df \times B \times \rho_u$

$= 3.9942 \times 10^{15} \times 1.0 \times 0.846 \times 42,000 \times 18.78$

$= 2.67 \times 10^{21}$ n/cm^2

Answers

Case 5

Graphite weight loss will cause damage functions to increase.

Dimensional changes in the moderator brick transverse direction will have little or no effect on damage functions. However, axial brick shrinkage will densify the core and cause calculated damage function values to be reduced.

Answers

Case 1

- End of life bore dose, EDND = 1.687×10^{21} n/cm^2 (See Lecture 1 workshop answers for cases 1 and 2).
  DIDO equivalent rating at bore = 0.21×10^{13} n/cm^3. s
  At 200°C, T_i = 473 K

$$\frac{1}{\theta} = \frac{1}{T_i} + \frac{k}{E}\ln\left(\frac{\phi}{4\times10^{13}}\right)$$

$$= \frac{1}{473} + \frac{8.617 \times 10^{-5}}{1.2}\ln\left(\frac{0.21}{4}\right) = 526 \text{ K i.e. } 253^\circ\text{C}$$

Draw up table using dose / dose rate ratios from Case 1. Answers of Lecture workshop :-

R_g	ϕ	EDND	θ	θ	Shrinkage
	n/cm^2. s	n/cm^2	K	°C	%
0	0.21×10^{13}	1.687×10^{21}	526	253	1.45
1	0.168×10^{13}	1.350×10^{21}	530	257	0.85
2	0.121×10^{13}	0.972×10^{21}	537	264	0.48
3	0.086×10^{13}	0.672×10^{21}	545	272	0.26
5	0.0445×10^{13}	0.358×10^{21}	559	286	0.10

Note: Shrinkages read by interpolation between 250 and 300°C DIDO curves in Figure 2.

Answers

Case 2

$$\text{EDND} = 40,000 \text{ MWD/t} \times 1.0887 \times 10^{17} \frac{\text{n/cm}^2}{\text{MWD/t}}$$

$$= 4.355 \times 10^{21} n/cm^2$$

$$\text{Irradiation time} = \frac{\text{Calder equivalent dose, MWD/t}}{\text{Calder equivalent rating, MW/t}}$$

$$= \frac{40,000}{4.38} = 9132.4 \text{ days}$$

$$\text{Dose rate, } \phi, = \frac{4.355 \times 10^{21}}{9132.4 \times 24 \times 3600} = 0.552 \times 10^{13} n/cm^2 \cdot s$$

$$\frac{1}{\theta} = \frac{1}{573} + \frac{8.617 \times 10^{-5}}{1.2} \ln\left(\frac{0 \cdot 552}{4}\right)$$

$$\theta = 624K \quad \text{ie } 351\,^{\circ}C$$

From figures 2.6, 2.7, 2.8a and 2.8b:-

α (20 - 120)	perpendicular	$= 5.09 \times 10^{-6}$
α (20 - 120)	parallel	$= 1.53 \times 10^{-6}$
αi (300)	perpendicular	$= (5.09 + 0.83)\,10^{-6} = 5.92 \times 10^{-6}$
αi (300)	parallel	$= (1.53 + 0.83)\,10^{-6} = 2.36 \times 10^{-6}$
α (20 - 300)	perpendicular	$= 5.43 \times 10^{-6}$
α (20 - 300)	parallel	$= 1.85 \times 10^{-6}$

Answers

Case 3

EDND $= 20,000 \times 1.0887 \times 10^{17} = 2.177 \times 10^{21} n/cm^2$

Dose rate,, $\phi = \dfrac{2.177 \times 10^{21}}{25 \times 365 \times 24 \times 3600} = 0.276 \times 10^{13} n/cm^2 \cdot s$

$$\frac{1}{\theta} = \frac{1}{473} + \frac{8.617 \times 10^{-5}}{1.2} \ln\left(\frac{0.276}{4}\right)$$

$\theta = 520K$ ie 247°C

$$\frac{1}{K(T)} = \frac{1}{K_o(30)}\left[\frac{K_o(30)}{K_o(T)} + f \cdot \delta T\right] S_k \left[\frac{K_o}{K}\right] ox$$

$$\frac{1}{K(200)} = \frac{1}{100}\left[\frac{1}{0.78} + 53.5 \times 0.84\right] 1.0 \times e^{(3.1 \times 0.1)}$$

$$K(200) = \frac{100}{63.0} = 1.587 W/mK$$

Answers

Case 3

EDND $= 20,000 \times 1.0887 \times 10^{17} = 2.177 \times 10^{21} n/cm^2$

Dose rate,, $\phi = \dfrac{2.177 \times 10^{21}}{25 \times 365 \times 24 \times 3600} = 0.276 \times 10^{13} n/cm^2 \cdot s$

$$\frac{1}{\theta} = \frac{1}{473} + \frac{8.617 \times 10^{-5}}{1.2} \ln\left(\frac{0.276}{4}\right)$$

$\theta = 520K$ ie 247°C

$$\frac{1}{K(T)} = \frac{1}{K_o(30)}\left[\frac{K_o(30)}{K_o(T)} + f \cdot \delta T\right] S_k \left[\frac{K_o}{K}\right] ox$$

$$\frac{1}{K(200)} = \frac{1}{100}\left[\frac{1}{0.78} + 53.5 \times 0.84\right] 1.0 \times e^{(3.1 \times 0.1)}$$

$$K(200) = \frac{100}{63.0} = 1.587 W/mK$$

Answers

Case 4

If $f = 53.5$ (from case 3 then:

$$E = 31.1f = 31.1 \times 53.5 = 1664 \text{ J/g}$$

$$\left(\frac{dE}{dT}\right)_{max} = \frac{E}{1910} = \frac{1664}{1910} = 0.87 = 0.87 \text{ J/g.K}$$

Specific heat at 400°C = 1.43 J/g.K

$$\therefore Ratio = \frac{0.87}{1.43} = 0.61$$

Answers

Case 4

If $f = 53.5$ (from case 3 then:

$$E = 31.1f = 31.1 \times 53.5 = 1664 \text{ J/g}$$

$$\left(\frac{dE}{dT}\right)_{max} = \frac{E}{1910} = \frac{1664}{1910} = 0.87 = 0.87 \text{ J/g.K}$$

Specific heat at 400°C = 1.43 J/g.K

$$\therefore Ratio = \frac{0.87}{1.43} = 0.61$$

Answers

Case 4

If $f = 53.5$ (from case 3 then:

$$E = 31.1f = 31.1 \times 53.5 = 1664 \text{ J/g}$$

$$\left(\frac{dE}{dT}\right)_{max} = \frac{E}{1910} = \frac{1664}{1910} = 0.87 = 0.87 \text{ J/g.K}$$

Specific heat at 400°C = 1.43 J/g.K

$$\therefore Ratio = \frac{0.87}{1.43} = 0.61$$

Answers

Case 5

Initial total open pore volume, $V_{TOT} = 0.11 cm^3/cm^3$

Initial reactive pore volume, $V_{RPV} = 0.15 \times 10^{-8} \times RR$

Now from table 2.1, RR = 0.124×10^{-8}

$\therefore V_{RPV} = 0.15 \times 0.124 = 0.0186$

The ratio $V_{RPV}/V_{TOT} = 0.0186/0.11 = 0.169$

Dimensional change % =0.169 curve A + 0.831 curve B

Answers

Case 5

Initial total open pore volume, $V_{TOT} = 0.11 cm^3/cm^3$

Initial reactive pore volume, $V_{RPV} = 0.15 \times 10^{-8} \times RR$

Now from table 2.1, RR = 0.124×10^{-8}

$\therefore V_{RPV} = 0.15 \times 0.124 = 0.0186$

The ratio $V_{RPV}/V_{TOT} = 0.0186/0.11 = 0.169$

Dimensional change% =0.169 curve A + 0.831 curve B

Answers

Case 5

Initial total open pore volume, $V_{TOT} = 0.11 cm^3/cm^3$

Initial reactive pore volume, $V_{RPV} = 0.15 \times 10^{-8} \times RR$

Now from table 2.1, RR = 0.124×10^{-8}

$\therefore V_{RPV} = 0.15 \times 0.124 = 0.0186$

The ratio $V_{RPV}/V_{TOT} = 0.0186/0.11 = 0.169$

Dimensional change% =0.169 curve A + 0.831 curve B

Answers

Case 6

- EDND = 1.8×10^{22} n/cm^2

$$\text{Dose rate} = \frac{1.8\times10^{22}}{25\times365\times24\times3600} = 2.283\times10^{13}\ \text{n/cm}^2\text{.s}$$

(1.2 eV) $$\frac{1}{\theta} = \frac{1}{723} + \frac{8.617\times10^{-5}}{1.2}\cdot\ln\frac{2.283}{4}$$

$$\theta = 745K \text{ ie } 472^\circ C$$

(3eV) $$\frac{1}{\theta} = \frac{1}{723} + \frac{8.617\times10^{-5}}{3}\cdot\ln\frac{2.283}{4}$$

$$\theta = 732K \text{ ie } 459^\circ C$$

$$\frac{1}{K(T)} = \frac{1}{K_o(30)}\cdot\left[\frac{K_o(30)}{K_o(T)} + f\cdot\delta T\right]\cdot Sk\left[\frac{K_o}{K}\right]_{ox}$$

From Figs 2.14, 2.15, 2.17 and 2.18:-

$K_o(30) = 128^*$; $f = 4.7$;

$\frac{K_o(30)}{K_o(450)} = \frac{1}{0.825}$; $\delta T = 0.68$ at 450°C;

$\left(\frac{K_o}{K}\right)_{ox} = e^{2.7\times0.2} = 1.72$, $S_k = 1.1$

$$\frac{1}{K_{(450)}} = \frac{1}{128}\cdot\left[\frac{1}{0.825} + 4.7\times0.68\right]\cdot1.1\times1.72$$

$$K_{(450)} = 15.3 \text{ W/mK}$$

* Given in question.

Answers

Case 6

EDND = 1.8×10^{22} n/cm^2

Dose rate = $\dfrac{1.8\times10^{22}}{25\times365\times24\times3600} = 2.283\times10^{13}$ n/cm^2.s

(1.2 eV) $\dfrac{1}{\theta} = \dfrac{1}{723} + \dfrac{8.617\times10^{-5}}{1.2}\cdot\ln\dfrac{2.283}{4}$

$\theta = 745K$ ie 472°C

(3eV) $\dfrac{1}{\theta} = \dfrac{1}{723} + \dfrac{8.617\times10^{-5}}{3}\cdot\ln\dfrac{2.283}{4}$

$\theta = 732K$ ie 459°C

$$\frac{1}{K(T)} = \frac{1}{K_o(30)}\cdot\left[\frac{K_o(30)}{K_o(T)} + f\cdot\delta T\right]\cdot Sk\left[\frac{K_o}{K}\right]_{ox}$$

From Figs 2.14, 2.15, 2.17 and 2.18:-

$K_o(30) = 128^*$; $f = 4.7$;

$\dfrac{K_o(30)}{K_o(450)} = \dfrac{1}{0.825}$; $\delta T = 0.68$ at 450°C;

$\left(\dfrac{K_o}{K}\right)_{ox} = e^{2.7\times0.2} = 1.72$, $S_k = 1.1$

$$\frac{1}{K_{(450)}} = \frac{1}{128}\cdot\left[\frac{1}{0.825} + 4.7\times0.68\right]\cdot1.1\times1.72$$

$K_{(450)} = 15.3$ W/mK

* Given in question.

Answers

Case 7

- EDND = 1×10^{22} n/cm^2, Dose rate = 2×10^{13} n/cm^{2}s

$$\frac{1}{\theta} = \frac{1}{723} + \frac{8.617\times10^{-5}}{3.0}\cdot\ln\left(\frac{2}{4}\right)$$

θ = 734K ie 461°C

From Figs 2.6, 2.7, 2.9a and 2.9b

α_o (20 - 120) = 4.5×10^{-6}

Correction for α_o = $(4.5 - 4.35)\times10^{-6}$ = 0.15×10^{-6}

Correction for strain = -1.35×10^{-6} (Fig 2.9b)

Irradiated $\alpha_{(20-120)}$ = 3.7×10^{-6} (Fig 2.9a)

Corrected $\alpha_{(20-120)}$ = $(3.7 + 0.15 - 1.35)\times10^{-6}$

= 2.5×10^{-6}

From Fig 2.6:-

Irradiated $\alpha_{i(450)} = A\alpha_i + B_i$

= $1\times2.5\times10^{-6} + 1.25\times10^{-6}$

= 3.75×10^{-6} W/m.K

From Fig 2.7:-

Irradiated $\alpha_{(20-450)}$ = 3.2×10^{-6} W/m.K

Answers

Case 1

$$g_o = \frac{145 \cdot \varepsilon_e \cdot G_{-c} \cdot D \cdot p}{T}$$

$$\varepsilon_e = \frac{0.22}{1.7} \quad \frac{cm^3}{cm^3}\frac{cm^3}{g} = 0.1294 \ cm^3/g$$

$$\therefore g_o = \frac{145 \times 0.1294 \times 1.2 \times 0.1 \times 120}{473} = 0.57 \ \% \text{ per year}$$

Time	$g_o t$	$C_t \left(= 28.205\left[\exp\frac{g_o t}{28.205} - 1\right]\right)$
yrs	%	%
5	2.85	3.00
10	5.70	6.32
15	8.55	9.99
20	11.40	14.05
25	14.25	18.54

$$C_t = A\left[\exp\frac{g_o t}{A} - 1\right]$$

$$A = \frac{100\pi e}{(1 - \pi e)} = \frac{100 \times 0.22}{0.78} = 28.205$$

$$\therefore C_t = 28.205\left[\exp\frac{g_o t}{28.205} - 1\right]$$

Answers

Case 1

$$g_o = \frac{145 \cdot \varepsilon_e \cdot G_{-c} \cdot D \cdot p}{T}$$

$$\varepsilon_e = \frac{0.22}{1.7} \quad \frac{cm^3}{cm^3}\frac{cm^3}{g} = 0.1294 \ cm^3/g$$

$$\therefore g_o = \frac{145 \times 0.1294 \times 1.2 \times 0.1 \times 120}{473} = 0.57 \ \% \text{ per year}$$

Time	$g_o t$	$C_t \left(= 28.205\left[\exp\frac{g_o t}{28.205} - 1\right]\right)$
yrs	%	%
5	2.85	3.00
10	5.70	6.32
15	8.55	9.99
20	11.40	14.05
25	14.25	18.54

$$C_t = A\left[\exp\frac{g_o t}{A} - 1\right]$$

$$A = \frac{100\pi e}{(1 - \pi e)} = \frac{100 \times 0.22}{0.78} = 28.205$$

$$\therefore C_t = 28.205\left[\exp\frac{g_o t}{28.205} - 1\right]$$

Answers

Case 2

Time t	Mean Weight Loss to time t, %	$g_o t$	New $g_o t$	New C_t
yrs		const. dose	%	%
5	1	2.85	2.879	3.03
10	2	5.70	5.816	6.46
15	3	8.55	8.814	10.34
20	4.12	11.40	11.89	14.79
25	5.4	14.25	15.06	19.90

$$\text{New } C_t = 28.205\left[\exp\frac{g_o t}{28.205} - 1\right]$$

Answers

Case 2

Time t	Mean Weight Loss to time t, %	$g_o t$	New $g_o t$	New C_t
yrs		const. dose	%	%
5	1	2.85	2.879	3.03
10	2	5.70	5.816	6.46
15	3	8.55	8.814	10.34
20	4.12	11.40	11.89	14.79
25	5.4	14.25	15.06	19.90

$$\text{New } C_t = 28.205\left[\exp\frac{g_o t}{28.205} - 1\right]$$

Answers

Case 2

Time t	Mean Weight Loss to time t, %	$g_o t$	New $g_o t$	New C_t
yrs		const. dose	%	%
5	1	2.85	2.879	3.03
10	2	5.70	5.816	6.46
15	3	8.55	8.814	10.34
20	4.12	11.40	11.89	14.79
25	5.4	14.25	15.06	19.90

$$\text{New } C_t = 28.205\left[\exp\frac{g_o t}{28.205} - 1\right]$$

Answers

Case 2

Time t	Mean Weight Loss to time t, %	$g_o t$	New $g_o t$	New C_t
yrs		const. dose	%	%
5	1	2.85	2.879	3.03
10	2	5.70	5.816	6.46
15	3	8.55	8.814	10.34
20	4.12	11.40	11.89	14.79
25	5.4	14.25	15.06	19.90

$$\text{New } C_t = 28.205\left[\exp\frac{g_o t}{28.205} - 1\right]$$

Answers

Case 3

For operation at constant power (i.e. increasing dose rate) the following equation must be satisfied :-

$$\frac{A^2}{100\pi e}\ln\left(1+\frac{C_t}{A}\right)-\frac{A}{100}C_t = g_o t$$

Now if A = 28.205, π_e = 0.22, $g_o t$ = 14.25, then:

$$\frac{28.205^2}{100\times 0.22}\ln\left(1+\frac{C_t}{28.205}\right)-\frac{28.205}{100}C_t = 14.25$$

$$36.16\times \ln\left(1+\frac{C_t}{28.205}\right)-0.282C_t = 14.25$$

Try C_t = 20

$$36.16 \text{ x } \ln(1.7091) - 5.64 = 14.25$$

$$19.38 - 5.64 = 13.74 \neq 14.25$$

Try C_t = 21

$$36.16 \text{ x } \ln(1.7445) - 5.92 = 14.25$$

$$20.12 - 5.92 = 14.20 \approx 14.25$$

From figure 9, C_t = 21%

Answers

Case 3

For operation at constant power (i.e. increasing dose rate) the following equation must be satisfied :-

$$\frac{A^2}{100\pi e}\ln\left(1+\frac{C_t}{A}\right)-\frac{A}{100}C_t = g_o t$$

Now if A = 28.205, π_e =0.22, $g_o t$ = 14.25, then:

$$\frac{28.205^2}{100\times 0.22}\ln\left(1+\frac{C_t}{28.205}\right)-\frac{28.205}{100}C_t = 14.25$$

$$36.16\times \ln\left(1+\frac{C_t}{28.205}\right)-0.282C_t = 14.25$$

Try C_t = 20

$$36.16 \text{ x } \ln(1.7091) - 5.64 = 14.25$$

$$19.38 - 5.64 = 13.74 \neq 14.25$$

Try C_t = 21

$$36.16 \text{ x } \ln(1.7445) - 5.92 = 14.25$$

$$20.12 - 5.92 = 14.20 \approx 14.25$$

From figure 9, C_t = 21%

Answers

Case 4

Perpendicular Young's Modulus, E

Time, t	EDND	$\left(\frac{E}{E_o}\right)_i$	Wt Loss	$\left(\frac{E}{E_o}\right)_{ox}$	$\left(\frac{E}{E_o}\right)$	E
yrs	x 10^{21} n/cm^2		%			GPa
0	0	1	0	1	1	5.4
5	0.435	2.19	3.03	0.8646	1.8935	10.22
10	0.871	2.07	6.46	0.7334	1.518	8.20
15	1.306	2.07	10.34	0.6088	1.260	6.81
20	1.742	2.07	14.79	0.4917	1.018	5.50
25	2.177	2.07	19.90	0.3847	0.7963	4.30

$\left(\frac{E}{E_o}\right)_i$ from Figure 2.23, $\left(\frac{E}{E_o}\right)_{ox} = e^{-4.8x}$.

Perpendicular Strength, σ

Time, t	EDND	$\left(\frac{\sigma}{\sigma_o}\right)_i$	Wt Loss	$\left(\frac{\sigma}{\sigma_o}\right)_{ox}$	$\left(\frac{\sigma}{\sigma_o}\right)$	σ
yrs	x 10^{21} n/cm^2		%			GPa
0	0	1	0	1	1	12.00
5	0.435	1.48	3.03	0.8542	1.264	15.17
10	0.871	1.44	6.46	0.7147	1.029	12.35
15	1.306	1.44	10.34	0.5841	0.841	10.09
20	1.742	1.44	14.79	0.4634	0.667	8.01
25	2.177	1.44	19.90	0.3553	0.512	6.14

$\left(\frac{\sigma}{\sigma_o}\right)_i = \sqrt{\left(\frac{E}{E_o}\right)_i}$ from above, $\left(\frac{\sigma}{\sigma_o}\right)_{ox} = e^{-5.2x}$.

Answers

Case 4 (Continued)

Parallel Young's Modulus, E

Time, t	EDND	$\left(\frac{E}{E_o}\right)_i$	Wt Loss	$\left(\frac{E}{E_o}\right)_{ox}$	$\left(\frac{E}{E_o}\right)$	E
yrs	x 10^{21} n/cm^2		%			GPa
0	0	1	0	1	1	11.70
5	0.435	2.12	3.03	0.8646	1.833	21.45
10	0.871	1.87	6.46	0.7334	1.372	16.05
15	1.306	1.73	10.34	0.6088	1.053	12.32
20	1.742	1.61	14.79	0.4917	0.7916	9.26
25	2.177	1.61	19.90	0.3847	0.6194	7.25

$\left(\frac{E}{E_o}\right)_i$ from Figure 2.22, $\left(\frac{E}{E_o}\right)_{ox} = e^{-4.8x}$.

Parallel Strength, σ

Time, t	EDND	$\left(\frac{\sigma}{\sigma_o}\right)_i$	Wt Loss	$\left(\frac{\sigma}{\sigma_o}\right)_{ox}$	$\left(\frac{\sigma}{\sigma_o}\right)$	σ
yrs	x 10^{21} n/cm^2		%			GPa
0	0	1	0	1	1	19.00
5	0.435	1.456	3.03	0.8542	1.244	23.63
10	0.871	1.368	6.46	0.7147	0.9771	18.57
15	1.306	1.315	10.34	0.5841	0.7683	14.60
20	1.742	1.269	14.79	0.4634	0.5880	11.17
25	2.177	1.269	19.90	0.3553	0.4508	8.57

$\left(\frac{\sigma}{\sigma_o}\right)_i = \sqrt{\left(\frac{E}{E_o}\right)_i}$ from above, $\left(\frac{\sigma}{\sigma_o}\right)_{ox} = e^{-5.2x}$.

Answers

Case 4 (Continued)

Parallel Young's Modulus, E

Time, t	EDND	$\left(\frac{E}{E_o}\right)_i$	Wt Loss	$\left(\frac{E}{E_o}\right)_{ox}$	$\left(\frac{E}{E_o}\right)$	E
yrs	x 10^{21} n/cm^2		%			GPa
0	0	1	0	1	1	11.70
5	0.435	2.12	3.03	0.8646	1.833	21.45
10	0.871	1.87	6.46	0.7334	1.372	16.05
15	1.306	1.73	10.34	0.6088	1.053	12.32
20	1.742	1.61	14.79	0.4917	0.7916	9.26
25	2.177	1.61	19.90	0.3847	0.6194	7.25

$\left(\frac{E}{E_o}\right)_i$ from Figure 2.22, $\left(\frac{E}{E_o}\right)_{ox} = e^{-4.8x}$.

Parallel Strength, σ

Time, t	EDND	$\left(\frac{\sigma}{\sigma_o}\right)_i$	Wt Loss	$\left(\frac{\sigma}{\sigma_o}\right)_{ox}$	$\left(\frac{\sigma}{\sigma_o}\right)$	σ
yrs	x 10^{21} n/cm^2		%			GPa
0	0	1	0	1	1	19.00
5	0.435	1.456	3.03	0.8542	1.244	23.63
10	0.871	1.368	6.46	0.7147	0.9771	18.57
15	1.306	1.315	10.34	0.5841	0.7683	14.60
20	1.742	1.269	14.79	0.4634	0.5880	11.17
25	2.177	1.269	19.90	0.3553	0.4508	8.57

$\left(\frac{\sigma}{\sigma_o}\right)_i = \sqrt{\left(\frac{E}{E_o}\right)_i}$ from above, $\left(\frac{\sigma}{\sigma_o}\right)_{ox} = e^{-5.2x}$.